



MPHIL

Towards Brillouin Enabled Photonic Switching and Quantum Memories

Weaver, Tom

Award date:
2023

Awarding institution:
University of Bath

[Link to publication](#)

Alternative formats

If you require this document in an alternative format, please contact:
openaccess@bath.ac.uk

Copyright of this thesis rests with the author. Access is subject to the above licence, if given. If no licence is specified above, original content in this thesis is licensed under the terms of the Creative Commons Attribution-NonCommercial 4.0 International (CC BY-NC-ND 4.0) Licence (<https://creativecommons.org/licenses/by-nc-nd/4.0/>). Any third-party copyright material present remains the property of its respective owner(s) and is licensed under its existing terms.

Take down policy

If you consider content within Bath's Research Portal to be in breach of UK law, please contact: openaccess@bath.ac.uk with the details. Your claim will be investigated and, where appropriate, the item will be removed from public view as soon as possible.

Towards Brillouin Enabled Photonic Switching and Quantum Memories

Thomas Weaver

University of Bath
Centre for Photonics and Photonic Materials
Department of Physics
July 2022

Supervised by
Dr. Joshua Nunn

Submitted for the degree of Master of Philosophy

Copyright

Attention is drawn to the fact that copyright of this thesis/portfolio rests with the author and copyright of any previously published materials included may rest with third parties. A copy of this thesis/portfolio has been supplied on condition that anyone who consults it understands that they must not copy it or use material from it except as licensed, permitted by law or with the consent of the author or other copyright owners, as applicable.

Abstract

This thesis explores two separate research avenues that both utilise stimulated Brillouin scattering in order to achieve their goal. The first employs a phonon generated in diamond by backwards Brillouin scattering in order to store and retrieve quantum information for use in quantum computing. The second uses the physical hypersonic waves induced by forwards Brillouin scattering in a null coupling fibre taper in order to switch light from one output to another.

A number of experiments were completed along both paths, work was first done to find the acoustic phonon lifetime in diamond which sets the lifetime of the quantum memory, however results for this experiment were inconclusive due to limitations regarding the difficulty of executing such an experiment, a figure for the acoustic phonon lifetime in diamond has since been established in the literature. A polarimetry experiment took place on a fibre taper in order to confirm the presence of acoustic modes, which produced good and expected results, however the following experiment that was designed to find the specific frequency of the acoustic mode produced null results, the reason for which are numerous.

A theoretical investigation into both devices' feasibility was also completed on these systems using a finite-element method. Results from these simulations show that while the potential for a functioning Brillouin-based diamond quantum memory is high as full switching is possible at distances of 6.36cm with gain values of $63.3\text{W}^{-1}\text{m}^{-1}$, the possibility of building a functioning photonic switch with this particular architecture and switching system is unlikely, as taper fabrication parameters needed for a full transfer of power require aspect ratios far higher than what is physically possible when considering reasonable laser systems.

Declaration of any previous submission of the work

The material presented here for examination for the award of a higher degree by research has been incorporated into a submission for another degree.

TWeaver

Declaration of authorship

I am the author of this thesis, and the work described therein was carried out by myself personally, with the exception of chapter 2, where 50% of the work was carried out by other researchers, Carlo Page and Tabijah Wasawo. Namely the formulation of ideas and the experimental details presented at the end of the chapter.

TWeaver

Contents

1	Introduction	1
1.1	Classical Computing	3
1.2	Quantum Computing	4
1.2.1	Single Qubit Operations	6
1.2.2	Two-Qubit Operations	8
1.2.3	Limitations	10
1.2.4	Quantum Computing Protocols	10
1.2.5	Linear Optics Quantum Computing	13
1.3	Quantum Memories	18
1.3.1	Quantum Memory Protocols	20
1.4	Photonic Switching	24
1.4.1	Photonic Switching Protocols	25
1.5	Device Proposals	29
1.5.1	Quantum Memory	29
1.5.2	Photonic Switch	31
2	Laboratory Logistics and Rubidium Vapour	33
2.1	Common Laboratory Equipment and Techniques	35
2.1.1	Saturated Absorption Spectroscopy	38
2.1.2	Two-Photon Absorption	42
2.2	Current and Further Work	44
3	Non-Linear Optics and Stimulated Brillouin Scattering	45

3.1	Applications of Stimulated Brillouin Scattering	52
4	A Finite-Element Analysis of Brillouin Scattering: Diamond	55
4.1	FeNICS and PySBS	55
4.2	Results	58
4.2.1	Diamond	58
5	Backward Brillouin Scattering in Diamond for use in Quantum Mem-	64
	ories	
5.1	Material Properties of Diamond	64
5.1.1	Applications of Diamond	65
5.1.2	Diamond-Based Quantum Memories	69
5.2	Light Storage in Diamond via Stimulated Brillouin Scattering	70
5.2.1	Detuning With an Electro-optic Modulator	72
5.2.2	Detuning With Two Lasers	76
5.3	Further Work	79
6	A Finite-Element Analysis of Brillouin Scattering: Fibre Tapers	81
6.1	Intramodal FSBS	83
6.2	Intermodal FSBS	86
7	A Proposal for A Photonic Switch Using Brillouin Scattering Induced	
	Acoustic Modes in Null-Coupling Fibre Tapers	89
7.1	Fibre Tapers	90
7.1.1	Taper Fabrication	90
7.1.2	Fibre based Couplers and Null Coupling Fibre Tapers	92
7.2	Null-Coupling Fibre Taper as a Photonic Switch	94
7.3	Proof-of-Concept Experiments	95
7.4	Switching Speed	102
7.5	Length Analysis	104
7.6	Further Work	110

8	Summary and Conclusions	113
A	A Mathematical Model of Brillouin Scattering	116
A.1	Lattice Vibrations in Crystals	116
A.2	The Three Contributions to Brillouin Scattering	122
A.3	Quantising SBS	129
B	Finite Element Analysis	135
C	Electromagnetic Modes in an Optical Fibre	140
C.1	Loss	145
C.2	Mode Development in Transition Regions	147

Chapter 1

Introduction

Using light to process information has use in both classical and quantum applications. Data centres are becoming larger and light provides the ideal mechanism for information transfer as it moves quickly, does not rely on cumbersome copper wires, and has an enhanced bandwidth. Light also has application in quantum computing, here, it takes the form of individual photons which have low decoherence and the ability to entangle remotely, and thus have some unique advantages over other quantum computing regimes.

This is not without issue, in both classical and quantum photonics the need arises for a photonic switch, these are devices capable of re-routing light from one direction to another and are integral to the operation of these systems.

Specific to quantum photonics is the need for a quantum memory, these are devices capable of storing quantum information for short amounts of time and have application in a variety of quantum information systems including quantum computing and quantum cryptography.

In this thesis, the feasibility of two devices that pertain to these ideas is investigated, the first is a diamond-based quantum memory that uses acoustic phonons accessed via Brillouin scattering to store quantum information, and the second uses a null-coupling fibre taper along with Brillouin scattering to switch light from one output to another.

Also presented is a theoretical investigation into both of these systems.

Chapter one presents a literature review on the topic of both quantum and classical computing, with a focus on how quantum memories and photonic switching are used in these systems.

Chapter two gives a brief introduction into some of the technical issues that arise when designing and building experiments, particularly when there is a significant overlap between distinct research avenues. Some preliminary data is presented towards two switchable cavity quantum memories that use rubidium to instigate the switching mechanism.

Chapter three provides the background information associated with Brillouin scattering, which is the fundamental physics that underlies the ideas presented in the remainder of the thesis. Both classical and quantum analyses are presented.

Chapter four introduces finite element analysis as the technique used to model the physical systems present in this thesis, as well as presenting results of the simulations of the diamond experiment.

Chapter five describes the diamond-based quantum memory in both the details of the final storage mechanism as well as some of the early experiments that have taken place to achieve that goal.

Chapter six moves from diamond to fibre and from quantum memories to photonic switching, beginning with a theoretical description of stimulated Brillouin scattering in optical fibre tapers using the same techniques present in chapter 4.

Chapter seven describes the details of the null-coupling fibre taper photonic switch, along with a series of experiments that work in the direction of creating a functioning device. This chapter also unites the theory presented in chapter six with an analytical description

to analyse the feasibility of the device.

Chapter eight concludes the thesis and provides a summary of the novel information that this thesis is built around.

1.1 Classical Computing

It is exceedingly rare these days to leave the house without interacting in some way with a computer. They control almost everything, from alarm clocks to traffic lights, and most people carry one around in their pocket everywhere they go in the form of a mobile phone. The power and practicality of modern computers is unmatched, but on a fundamental level they are simple machines that take user inputs translated into binary (i.e. chains of ones and zeros, or bits, that can be used to describe numbers, letters, and other inputs), stores and processes that information using a particular code, at which point the new information is output to be viewed and analysed by the user [1].

Data is processed using Boolean logic operations which are often named explicitly after what they do, for example, a NOT gate flips the input bit, the input is not equal to the output. Other logic gates include AND, OR, and NOR gates [2], combinations of which can be used to perform simple mathematics, this can be scaled up to perform useful operations.

Physically, these gates are built using transistors which are electronic devices comprised of a semiconductor, usually silicon, with three terminals, a small signal is applied to one of these inputs and can control how current passes through the device through the other two terminals. This is possible because of the particular doping architecture in the device. Modern high end computers contain processors that have upwards of 39 billion transistors [3], which is a good improvement over the early transistor computers of the 40s and 50s, whose transistor count sat at a humble 200 [4].

The exponential growth of on-chip transistors over the past seven decades can be described by Moore's law, a very general rule which states that the number of on-chip transistors double every 18 months, however, this growth is not sustainable. The cost of fabrication of these devices also follows an exponential pattern, so left unchecked it would not take long for the semiconductor chip industry to surpass gross world product [5]. Size of transistors also needs to be considered, they grow smaller every generation and will soon be comprised of only a handful of individual atoms, it is expected to reach this point by 2037 [6], and so another fundamental barrier to Moore's law is found. The search for more powerful computation hardware continues, and those at the forefront of research are turning their heads to other means, one such way is quantum computing.

1.2 Quantum Computing

In order to fully understand the potential of quantum computing, the fundamental principles that govern these ideas must first be established, starting with perhaps the most publicly known quantum effect, a superposition. In simple terms, these can be described as a quantum system that occupies various states simultaneously until a detection event is undergone. This concept of being in two states at once is a common feature of quantum mechanics, an example of which is the spin of an electron, which can either be up or down or in a superposition of both. This can be represented mathematically as

$$|\psi\rangle = \alpha_0 |\uparrow\rangle + \alpha_1 |\downarrow\rangle, \quad (1.1)$$

where $|\uparrow\rangle$ and $|\downarrow\rangle$ are the spin up and spin down states, α_0 and α_1 are complex coefficients that represent the probability amplitude of a system being in its corresponding state, and $|\psi\rangle$ is the overall state of the electron.

The probability that an electron is in the $|\uparrow\rangle$ or $|\downarrow\rangle$ state is proportional to $|\alpha_0|^2$ and $|\alpha_1|^2$ respectively. The following equation is produced as a result of this and is the generalised case for i states

$$\sum_i |\alpha_i|^2 = 1. \quad (1.2)$$

This result shows that a system occupying a superposition is a unit vector, regardless of what the values of α_i are.

The base unit of quantum computing is the quantum bit, or the qubit, which similarly to classical computing can represent either a 1 or a 0, but unlike classical computers the qubit can also exist in a superposition state between 0 and 1. There are various systems that can be used as qubits (described in section 1.2.4), but for now electron spin will continue to be used to explore the ideas of quantum computing.

Continuing this example further, consider now a system of two electrons in a closed system both of which are put into superpositions. When the system is observed, there are four potential outcomes, both electrons are spin up, both electrons are spin down, electron 1 is spin up but electron 2 is spin down, and electron 1 is spin down but electron 2 is spin up, this means that four different probability coefficients are needed to fully describe the system. For quantum computing with electron spin, spin-up and spin-down can be transcribed as 1 and 0 respectively, and so

$$|\psi\rangle = \alpha_0 |11\rangle + \alpha_1 |10\rangle + \alpha_2 |01\rangle + \alpha_3 |00\rangle. \quad (1.3)$$

This equation shows that a 2-qubit system needs four complex coefficients in order to fully characterise the potential outcomes, that is, four individual pieces of information compared to a classical computers two using the same number of bits. The amount of information that a qubit system can hold increases exponentially with an increasing number of qubits, for a system with N qubits, the amount of states that system is able to be measured in is 2^N . A system with 100 qubits can be measured 1.27×10^{30} states, the equivalent to one hundred bits.

Entanglement is another useful tool in quantum computation, two systems are entangled

when the quantum state of each system cannot be described independently of the other. Mathematically, this can be described as quantum states that cannot be factored as a product of states of its local constituents. An interesting effect that arises as a result of entanglement is that there is an individually random, yet correlated fluctuation of observables between entangled systems in a way that is impossible to reproduce classically. Practical examples of entanglement have been shown in a variety of different ways, including using photons [7], neutrinos [8], molecules [9], and even between living bacteria and photons [10]. The upper limit to the scale of systems exhibiting quantum effects has recently been pushed, with entanglement occurring between a pair of vibrating membranes $10\mu\text{m}$ in size [11]. Quantum entanglement has a variety of applications and some believe it is an essential part of quantum computing [12], Bell states are a special case for two qubit systems and are examples of maximal entanglement, they are given as

$$|\phi^+\rangle \equiv \frac{1}{\sqrt{2}}[|00\rangle + |11\rangle] \quad (1.4)$$

$$|\phi^-\rangle \equiv \frac{1}{\sqrt{2}}[|01\rangle + |10\rangle] \quad (1.5)$$

$$|\psi^+\rangle \equiv \frac{1}{\sqrt{2}}[|00\rangle - |11\rangle] \quad (1.6)$$

$$|\psi^-\rangle \equiv \frac{1}{\sqrt{2}}[|01\rangle - |10\rangle]. \quad (1.7)$$

1.2.1 Single Qubit Operations

Single qubit rotations must be unitary operators as the qubit must remain on the surface of the Bloch sphere as it undergoes an operation, states that exhibit this property are known as pure states as they can be described by a single ket vector, counter to this are mixed states, these are states that cannot be described by a single ket vector and as such reside on the interior of the sphere [13]. The relation between input and output states can be expressed as

$$|\psi'\rangle = A|\psi\rangle, \quad (1.8)$$

where ψ and ψ' are input and output states respectively, with complex amplitudes α_0 and α_1 , and A is a unitary operator matrix. There are five primary single qubit gates [14], namely the Pauli spin operations and the Hadamard matrix

$$\sigma_0 = \begin{bmatrix} 1 & 0 \\ 0 & 1 \end{bmatrix} \quad (1.9)$$

$$\sigma_X = \begin{bmatrix} 0 & 1 \\ 1 & 0 \end{bmatrix} \quad (1.10)$$

$$\sigma_Y = \begin{bmatrix} 0 & -i \\ i & 0 \end{bmatrix} \quad (1.11)$$

$$\sigma_Z = \begin{bmatrix} 1 & 0 \\ 0 & -1 \end{bmatrix} \quad (1.12)$$

$$H = \frac{1}{\sqrt{2}} \begin{bmatrix} 1 & 1 \\ 1 & -1 \end{bmatrix}. \quad (1.13)$$

The first of these is the identity matrix and will have no effect on a qubit it is applied to, that is $|\psi'\rangle = \sigma_0 |\psi\rangle = |\psi\rangle$. It is used not as an operation it itself, but often becomes useful when describing mathematically the effect of multiple gates on a qubit. The second is the Pauli-X gate and is the equivalent to the classical NOT gate, it has the effect of swapping the amplitude probabilities of the two states. Using column representation for vectors, this is explained as

$$\begin{aligned} |\psi'\rangle = \sigma_X |\psi\rangle &= \begin{bmatrix} 0 & 1 \\ 1 & 0 \end{bmatrix} \begin{bmatrix} \alpha_0 \\ \alpha_1 \end{bmatrix} \\ &= \alpha_1 |0\rangle + \alpha_0 |1\rangle, \end{aligned} \quad (1.14)$$

where $|\psi\rangle = \alpha_0 |0\rangle + \alpha_1 |1\rangle$. This can be represented on the Bloch sphere as a π rotation about the x-axis. Next is the Pauli-Y gate, and acts to swap the amplitude probabilities, just as in the Pauli-X gate and also introduce a π phase shift between the two states

$$\begin{aligned}
|\psi'\rangle &= \sigma_Y |\psi\rangle = \begin{bmatrix} 0 & -i \\ i & 0 \end{bmatrix} \begin{bmatrix} \alpha_0 \\ \alpha_1 \end{bmatrix} \\
&= -i(\alpha_1 |0\rangle - \alpha_0 |1\rangle) = e^{i\gamma}(\alpha_1 |0\rangle + e^{i\pi}\alpha_0 |1\rangle),
\end{aligned} \tag{1.15}$$

where $\gamma = -\pi/2$ is an immeasurable phase constant. Similar to the Pauli-X gate, this is represented on the Bloch sphere by a π rotation about the y-axis. The final of the Pauli spin operations is the Pauli-Z gate and introduces a π phase shift between the two states

$$\begin{aligned}
|\psi'\rangle &= \sigma_Z |\psi\rangle = \begin{bmatrix} 1 & 0 \\ 0 & -1 \end{bmatrix} \begin{bmatrix} \alpha_0 \\ \alpha_1 \end{bmatrix} \\
&= \alpha_0 |0\rangle - \alpha_1 |1\rangle = \alpha_0 |0\rangle + e^{i\pi}\alpha_1 |1\rangle.
\end{aligned} \tag{1.16}$$

Once again, this can be represented as a π rotation about the z-axis on the Bloch sphere. Finally, there is the Hadamard matrix, which transforms the qubit into a superposition

$$\begin{aligned}
|\psi'\rangle &= H |\psi\rangle = \frac{1}{\sqrt{2}}(\sigma_X + \sigma_Z) |\psi\rangle \\
&= \alpha_0 |+\rangle + \alpha_1 |-\rangle,
\end{aligned} \tag{1.17}$$

where $|+\rangle$ and $|-\rangle$ are superposition states.

1.2.2 Two-Qubit Operations

Only a single two-qubit operation is discussed here, the controlled-NOT (CNOT) gate. As expected, the CNOT gate only operates on two qubit registers ($|\psi\phi\rangle$) which are made up of control ($|\psi\rangle$) and target ($|\phi\rangle$) qubits. A CNOT gate performs a Pauli-X operation on the target qubit only if the control qubit is $|\psi\rangle = |1\rangle$, for the case when the control qubit is $|\psi\rangle = |0\rangle$, the target qubit is left unchanged [15]. The matrix of this operation takes the form

$$A_{CNOT} = \begin{bmatrix} I & 0 \\ 0 & \sigma_X \end{bmatrix} = \begin{bmatrix} 1 & 0 & 0 & 0 \\ 0 & 1 & 0 & 0 \\ 0 & 0 & 0 & 1 \\ 0 & 0 & 1 & 0 \end{bmatrix}. \quad (1.18)$$

Combinations of one, two, and although not discussed here, three and more qubit operations can be used to perform more complex logic operations [16], for example, a Bell state can be generated using a Hadamard gate along with a CNOT gate another example is that two CNOT gates along with the three qubit Toffoli gate can be used to create the quantum counterpart to the classical ADDER gate, as show in figure 1.1.

Quantum circuits are used to express these operations as the matrix representation of more complex operations quickly becomes unmanageable. Input states are shown on the left of the diagram, each with their own channel that defines the sequence of events, single qubit operations are shown by boxes on a given channel and two qubit operations join two channels with a vertical line [17]. Figure 1.1 shows quantum circuits of the Bell state generator and quantum ADDER gate described earlier, introduced in the ADDER operations are Toffoli gates, similar to the CNOT gate but performed on 3 qubits, a Pauli-X gate is applied to a qubit if the first two are in the state $|1\rangle$ [18]. Not shown in these diagrams are measurements which are denoted as needles on a gauge and classical bits, represented as two parallel lines.

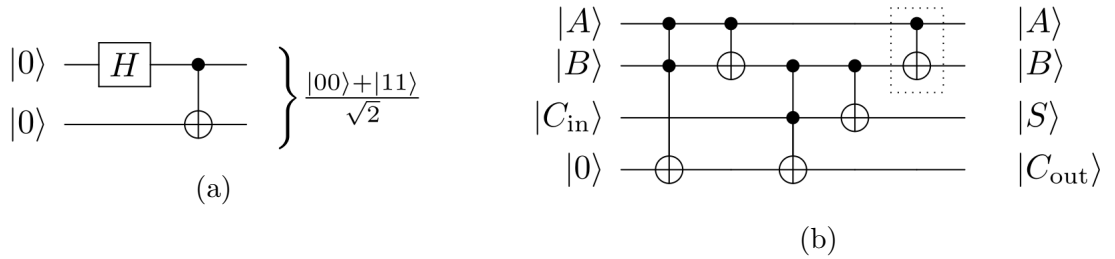


Figure 1.1: Two quantum circuits showing (a) Bell state generation using a Hadamard gate and a CNOT gate and (b) a quantum ADDER gate that makes use of CNOT and Toffoli gates.

All of this work would not be worthwhile if there isn't any clear examples of quan-

tum supremacy, situations where computation using quantum algorithms has the ability to solve problems that ordinary computing cannot when given a reasonable amount of time [19]. Thankfully there are many such examples, the first and most notable of these is Shor's algorithm, developed in 1994 by American mathematician Peter Shor. Shor's algorithm solves the simple problem of integer factorisation, it shows that for any integer with d digits, the runtime will scale with d^3 , comparing this to classical computation where the runtime for the most optimal integer factorisation algorithms scale with $\exp(d^{1/3})$ shows that Shor's algorithm provides a significantly more time efficient route to a solution [20]. Shor's algorithm makes use of the efficiency of quantum Fourier transforms and modular exponentiation by repeated squarings in order to achieve this goal.

1.2.3 Limitations

Decoherence occurs when the definite phase relation between different states described by the wavefunction of a system changes, it happens as a result of the interaction between a quantum system and its immediate classical surroundings [21,22].

Qubits will undergo bit flips, phase flips, or both due when decoherence acts against them [23], these errors are equivalent to the Pauli-X, -Z, and -Y gates respectively and will significantly disturb quantum computations, since they rely heavily on qubits being unaltered as they move between operations. Quantum error correction is used to combat against decoherence.

1.2.4 Quantum Computing Protocols

This section will provide a brief introduction to some of the more promising physical implementations of quantum computing characterised by the form of their qubits along with how far these protocols have progressed towards a fully functioning quantum computer.

- **Superconducting Circuits** - Quantum computers employing superconducting qubits

in their architecture follow three primary archetypes, charge [25], flux [26], and phase [27], each of these are cooled to 15mK in order to expose their superconducting properties and $|0\rangle$ and $|1\rangle$ states are mapped to different energy levels in the system corresponding to an integer number of Cooper pairs¹ for charge qubits, an integer number of flux quanta for flux qubits, and different charge oscillation amplitudes across a Josephson junction² for phase qubits. Gate operations are executed by applying microwave pulses to the qubits and qubits are coupled together using an intermediate electronic circuit.

Superconducting quantum computing is considered the frontrunner, with the likes of Google [30], IBM [31], and Intel [32] all working on building a fully functioning quantum computer using these systems. In 2019, Google presented a 53 qubit superconducting quantum processor that exhibited quantum supremacy for the first time, it did so by solving a complex problem in 200 seconds, impressive considering it is calculated to take a modern supercomputer 10,000 years to solve the same problem [30].

- **Trapped ions** - Qubits in this regime are charged atoms which are able to be suspended in free space by applying an electric field, the $|0\rangle$ and $|1\rangle$ states correspond to either two ground state hyperfine levels or a ground state and an excited state. There are a variety of specific elements that can be used in these systems including calcium, strontium, and ytterbium [33], all of which have different qualities such as absorption spectra and coherence times that may result in different outcomes. By applying short pulses of light to the ions, single gate operations are able to take place as well as coupling between ions.

Trapped ions have outstanding coherence times, making them useful in a variety of quantum applications, and in 2021, Pogorelov *et al* demonstrated a 20 qubit system making use of trapped ions, with the claim that one 100 qubit system is soon to follow [34,35].

¹A phenomena specific to superconductors, Cooper pairs are two weakly bound electrons with an attractive force caused by an electron-phonon interaction [28].

²Another effect specific to superconductors, a Josephson junction consists of two superconducting electrodes separated by an insulator, a current can be produced continuously without a voltage being applied [29].

- **Nuclear spin** - A less researched protocol that uses individual nuclear spins of atoms within a material or molecule as qubits, such as nitrogen vacancy defects within diamond and single alanine molecules. Qubit states are equivalent to up and down spin states, gate operations are performed using radio frequency pulses generated by an electromagnet. In 2001, Vandersypen *et al* [36] were able to perform Shor's algorithm on a 7 qubit NMR system.

In a similar vain, the spin of charge carriers in semiconductors can be used as qubits, specifically those found in quantum dots. Physical implementation of this, however, has only reached a total of ten qubits [37]. Quantum computing with nuclear spin can be distinguished into two categories, nuclear magnetic resonance and solid state. While the latter sees ongoing successful research as described above, nuclear magnetic resonance quantum computing has seen a stagnation in growth over the past decade.

- **Topological Quasiparticles** - Topological quantum computing provides an obscure insight into quantum computing, qubits take the form of non-abelian anyons, 2-dimensional topologically active quasiparticles consisting of collective excitations of many electrons [38]. Qubit states are mapped to the presence or absence of an electron at a detection event, and gate operations are applied by moving anyons around physically, leading to braids in space-time. While anyons have been physically detected [40], the only investigation into topological quantum computing is theoretical.

- **Photons** - Photons have the potential to have low decoherence [41] and their inherent property of flight allows for control over qubit separation and non-local entanglement, properties unavailable to solid-state protocols [42]. Photonic quantum computing forms the inspiration for the devices presented in this thesis and so the following section will provide a deeper explanation compared to those present in this section.

1.2.5 Linear Optics Quantum Computing

In 2001, Knill, Laflamme, and Milburn proved that full quantum computation is possible with only photons and linear optical elements such as mirrors, beamsplitters, and waveplates [43], this came to be known as the KLM protocol and forms the basis of linear optics quantum computing (LOQC).

The KLM protocol defines qubits as individual photons, with horizontal and vertical polarisation mapping to $|0\rangle$ and $|1\rangle$ states respectively. A photon is put into a superposition state (a Hadamard operation, resulting in states $1/\sqrt{2}(|0\rangle + |1\rangle)$ and $1/\sqrt{2}(|0\rangle - |1\rangle)$) by passing it through a half-wave plate, this has the physical effect of rotating the linear polarisation by 45° , resulting in diagonally polarised light. If a measurement is then taken in the horizontal-vertical basis, there is a 50/50 chance it will collapse into one of the two linear polarisation states. Circular polarisations of opposite handedness represent complex superposition states and can be achieved by passing a linearly polarised photon through a quarter-wave plate.

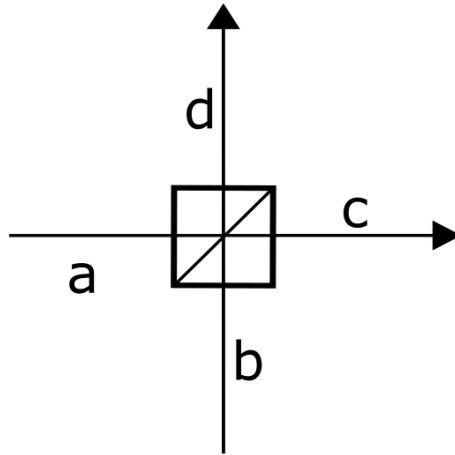


Figure 1.2: A simple beamsplitter, featuring input modes a and b and output modes c and d .

It is not just polarisation that can be used to express quantum information, spatial encoding, number encoding, and time-bin encoding have all been presented as potential solutions [44]. For the remainder of this section, however, polarisation will be used to describe LOQC.

There is a need for qubits to interact with one another in order to accurately apply multi-qubit gates, but this is not a function that light intrinsically has [45], photons usually pass through each other unperturbed. There are, however, unique circumstances where it is possible to engineer interactions using specific optical setups. There are four possible outcomes when two photons are incident on different inputs of a 50:50 beam splitter (shown in figure 1.2) at the same time, either both photons are reflected, both photons are transmitted, and two outcomes where one photon is transmitted and the other is reflected. Consider the quantum mechanical description of this interaction, two identical photons incident on different inputs can be described as

$$\hat{a}^\dagger \hat{b}^\dagger |0, 0\rangle_{ab} = |1, 1\rangle_{ab}, \quad (1.19)$$

where \hat{a}^\dagger and \hat{b}^\dagger are creation operators for input modes a and b , and $|0, 0\rangle_{ab}$ and $|1, 1\rangle_{ab}$ are Fock modes for inputs a and b , states denoting the number of particles within a specified state. There is a 50:50 chance that a photon will either reflect or transmit upon incidence with the beam splitter, and so

$$\begin{aligned} \hat{a}^\dagger &\rightarrow \frac{1}{\sqrt{2}}(\hat{c}^\dagger + \hat{d}^\dagger) \\ \hat{b}^\dagger &\rightarrow \frac{1}{\sqrt{2}}(\hat{c}^\dagger - \hat{d}^\dagger), \end{aligned} \quad (1.20)$$

where \hat{c}^\dagger and \hat{d}^\dagger are creation operators for outputs c and d . By combining the above equations, the output Fock states can be found for the case where two photons are incident on different inputs of a 50:50 beam splitter at the same time

$$\begin{aligned}
|1, 1\rangle_{ab} &= \hat{a}^\dagger \hat{b}^\dagger |0, 0\rangle_{ab} \\
&\rightarrow \frac{1}{2}(\hat{c}^\dagger + \hat{d}^\dagger)(\hat{c}^\dagger - \hat{d}^\dagger) |0, 0\rangle_{cd} \\
&= \frac{1}{\sqrt{2}}(|2, 0\rangle_{cd} + |1, 1\rangle_{cd} - |1, 1\rangle_{cd} + |0, 2\rangle_{cd}) \\
&= \frac{1}{\sqrt{2}}(|2, 0\rangle_{cd} + |0, 2\rangle_{cd}).
\end{aligned} \tag{1.21}$$

This provides the interesting result that instances where one photon occupies each of the output modes do not exist, instead, photons only exit in pairs.

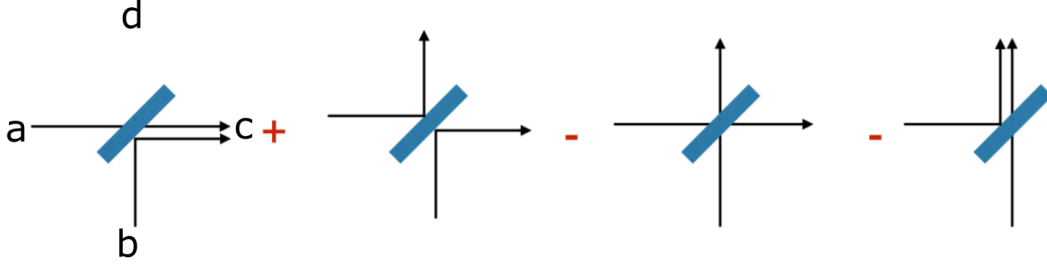


Figure 1.3: All potential outcomes of two photons incident on a 50:50 beam splitter, the middle two outcomes representing situations where one photon exits from both outputs cancel each other out (as shown in equation 1.21) leading to the Hong-Ou-Mandel effect. Reproduced from [46].

This effect has been proven to exist experimentally by Jachura *et al* [47], who placed detectors at both outputs of a beam splitter and measured the coincidence time between detection events, they measure a significant dip as coincidence tends to zero suggesting that photons exiting the beam splitter do so only through the same output.

This is known as the Hong-Ou-Mandel effect after those who found the effect in 1987 [48] and the associated measurement dip is known as the Hong-Ou-Mandel dip. This effect is used as the primary tool for entangling photons in LOQC, since photons at the output are indistinguishable.

There are many different architectures that are able to perform the same operation in LOQC, presented in figure 1.4 is an example of a CNOT gate derived by Gottesman *et*

al [49]. Present in the center is a 4-photon GHZ state (a maximally entangled multi-qubit state) $|\psi^+\rangle$ whose production causes a single photon to be emitted into each channel $1 \rightarrow 4$, the input target and control states $|\phi_1\rangle_t$ and $|\phi_2\rangle_c$ interfere on two separate polarising beam splitters³ of horizontal-vertical and orthogonal diagonal bases with two outputs form the Bell state. Bell measurements, measurements that find which of the Bell states a photon exists in, occur at all detectors in the system, and outputs 2 and 3 are only accepted when there is one and only one detection event at each detector. This in combination with the polarisation dependency of the beam splitters results in the photons exiting from outputs 2 and 3 exhibiting the desired transformation. This gate has a success rate of 25% when the creation of the ancillary Bell state is guaranteed which is somewhat less than desirable.

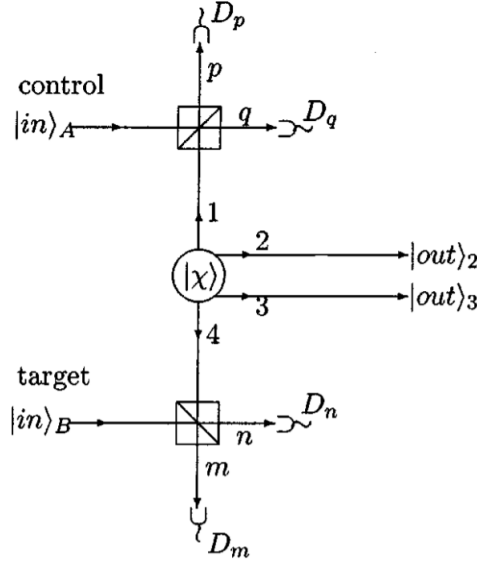


Figure 1.4: Physical implementation of a CNOT gate, a four qubit Bell state is prepared and each photon is sent into different channels, when a photon on each detector is measured the gate has succeeded. Reproduced from [50].

Processes within LOQC are often non-deterministic and so operations must be applied numerous times in order for a successful outcome. This severely limits the scalability of LOQC but can fortunately be eliminated with the inclusion of quantum teleportation-based logic gates, an example of which is the CNOT gate described above.

³Beamsplitters that direct one polarisation in one direction and the orthogonal polarisation in the other.

This idea of repeating non-deterministic operations until there is a successful outcome is known as multiplexing and can exist in a variety of forms. Multiplexing is split into three categories, spatial multiplexing, where multiple operations are run in parallel on different systems [53], temporal multiplexing, where operations are run successively on the same system [54], and frequency multiplexing, where operations are run on the same system at the same time but with different frequencies of light [55]. Physical implementation of multiplexing systems plays a key role in realising scalable LOQC.

There are some severe limitations to the implementation of the KLM protocol, although it has been shown to allow universal quantum computing and to be efficiently scalable the costs associated with even simple gate operations are significant [41]. As a result, there are a variety of protocols developed since KLM's original work that improve on both the scalability and the economic efficiency of LOQC. These improvements are largely based on cluster states [56].

A cluster state is a group of qubits all connected via entanglement [56], cluster states can take many different shapes as is shown in figure 1.5, where circles represent qubits and the lines that connect them represent entanglement. Clusters are built by first initialising all qubits into a superposition state, followed by performing a CZ operation on all qubits that are to be linked. The CZ gate is a two-qubit gate that is represented mathematically as $|q_1, q_2\rangle \rightarrow (-1)^{q_1 q_2} |q_1, q_2\rangle$ [41] and has the physical effect of entangling the qubits that are operated on [57].

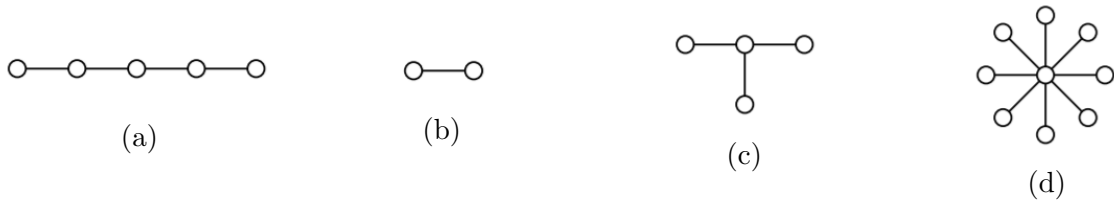


Figure 1.5: Five different examples of cluster states used in LOQC, including (a) a linear cluster of five qubits, (b) a cluster representing the Bell states, (c) a four qubit cluster state, and (d) a 9 qubit GHZ state. Reproduced from [41].

Cluster states allow for an alternative paradigm for quantum computing known as measurement based quantum computing (MBQC). Here, a large cluster state is built resembling a two-dimensional lattice, each row is equivalent to a single qubit in the circuit model and each column represents a single step in the time basis, algorithms are then applied sequentially by measuring all qubits in a single column from left to right. Single qubit gates are applied by selecting the basis for each measurement, and two-qubit gates are applied when two rows are connected by an edge in the cluster.

1.3 Quantum Memories

As described throughout this chapter, many of the processes that allow LOQC to perform accurate quantum computation are probabilistic in nature and so the need for a quantum memory arises as a result, devices capable of storing quantum information with on demand storage and retrieval [58].

For example, consider the Gottesman CNOT shown in figure 1.4, it is important in this system that both the input qubits and the 4-qubit Bell state are ready to be probed at the same time. If this is not the case there would be delays in deciding whether or not the output states are valid by which time the photons could travel huge distances. With the inclusion of a quantum memory, the 4-qubit Bell state can be pre-prepared and stored, so that when the input qubits are ready the Bell state can be released and the operation can take place. There are also applications at the end of this process, with the gate being probabilistic, successful attempts at a photonic CNOT gate can be stored and released on demand when other probabilistic systems operating in tandem have all had successful outcomes. Further still, for this gate to be considered single photons must be produced, a task that is possible but unexpectedly non-deterministic [59]. Quantum memories then play a vital role across various points in this process.

Applications for quantum memories are not limited to LOQC, quantum key distribution

takes advantage of a variety of quantum effects to securely send publicly undisclosed messages [60]. Qubits take the form of single photons as is the case for LOQC and are transported through optical fibre. Losses are low but certainly apparent when transporting light over long distances and so a need arises for quantum repeaters, devices capable of boosting a quantum signal and a process made difficult by the no-cloning principle [61]. Quantum repeaters work on the basis of entanglement swapping (figure 1.6) and quantum memories play an essential role, two photons that have never interacted are able to become entangled by a suitable detection event involving photons that they themselves are entangled to, leading to an unknown, but correlated variable between the two photons. Thus, with frequent enough quantum repeaters, quantum information is able to propagate indefinitely [62]. The likelihood of success of this multi-step deterministic process is vastly increased with the presence of a quantum memory, as successful entanglement events can be stored until the process is ready to go ahead [63].

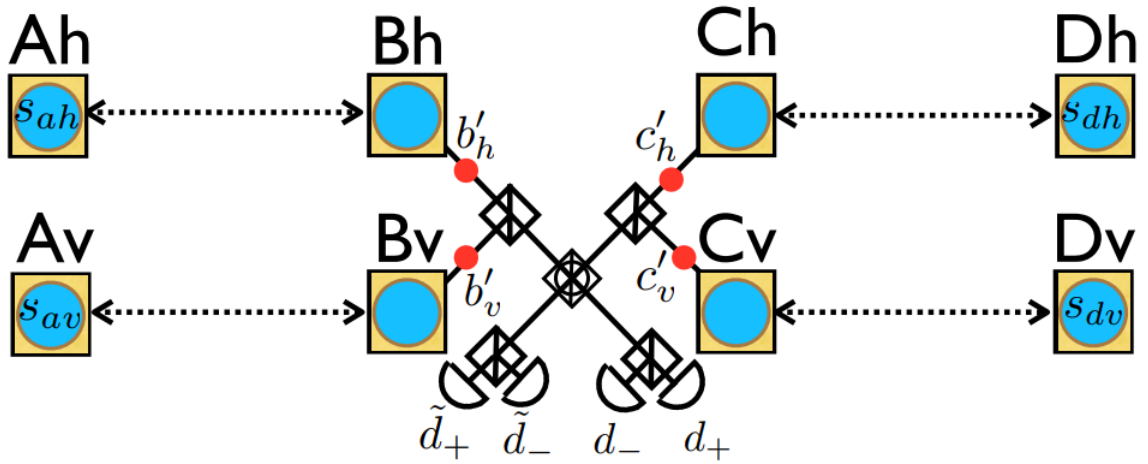


Figure 1.6: Long distance entanglement is created between qubits at locations A and B (also C and D), information is then stored in memories B_h , B_v , C_h , and C_v , which are read out together, combined, and detected. Subscripts denote polarisation (vertical or horizontal), squares with vertical lines are polarising beamsplitters, and the single square featuring a vertical line and a circle is a polarising beam splitter in the 45deg basis. Coincidence between d_+ and \tilde{d}_+ modes heralds the storage of two excitations in either A_h and D_h or A_v and D_v . Reproduced from [65].

Ideally a quantum memory would not have any effect on the quantum information residing within it, however in practise decoherence affects the stored qubit resulting in a different

output state. The similarity between input and output states is known as fidelity and is an important indicator of whether or not a quantum memory works [64].

Another important measure is storage lifetime, for some applications it is necessary to store information for times on the order of tens of seconds. Should decoherence affect a stored quantum state too much during that time then it would no longer be of any use and so the addition of a memory in this circumstance is futile [64].

Other such characteristics include operation wavelength, bandwidth, and multi-photon storage, all of which are important when considering the application of a memory.

1.3.1 Quantum Memory Protocols

The following section explores a non-exhaustive list of some of the recent implementations of quantum memories along with some of their benefits and detriments. Quantum memories have been developed along two distinct paths, optically controlled memories and engineered absorption [66]. The former takes place in a system with a particular absorption architecture and the presence of a control field can dynamically couple ground and storage states, resulting in an optically controlled memory. The latter engineers an inhomogeneous broadening of an energy level in rare earth ion-doped crystals allowing for broadband absorption and on demand read out as the process is reversible. Each of the following protocols will fit in to either one of these categories.

- **Raman Scattering** - The vibrational mode accessed by stimulated Raman scattering provides a broadband and wavelength-independent storage state. Two co-propagating pulses are able to couple ground and storage states when the frequency resonance condition $\Omega_{Storage} = \omega_{Signal} - \omega_{Pump}$ is met, leading to the transfer of energy from the signal beam to a vibrational mode in the material. A subsequent control pulse shortly follows and is able to stimulate a emission process leading to the retrieval of the stored signal [67]. There are some intrinsic problems associated with this process,. Noise is introduced where spontaneous Raman interactions take place due to a coupling between the strong control

field and the transition intended for the signal field, the same control field can stimulate an emission leading to a noise photon in the system. This occurs as the signal and control fields are spectrally very close and is therefore difficult to eliminate entirely [66].

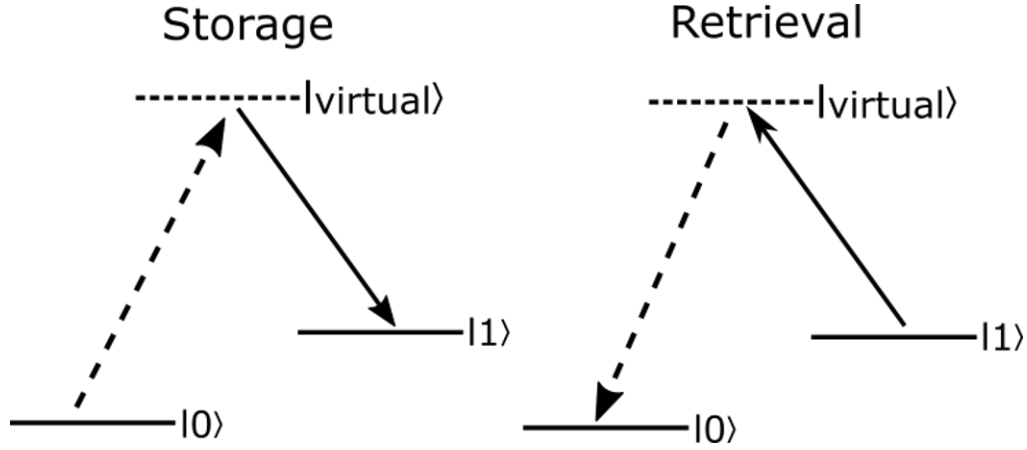


Figure 1.7: Energy level diagram describing the storage and retrieval of quantum information using Raman scattering. A strong pump field (dashed) and weak signal field (bold) interact to couple storage ($|1\rangle$) and ground ($|0\rangle$) states.

Raman memories have been demonstrated in both diamond [67] and gas-filled hollow core photonic crystal fibre [68] and show unfortunately short lifetimes of 50ns and 3.5ps respectively. This is not to say, however, that Raman memories are useless, as it has allowed for the study of light-matter interactions at the quantum level. Optical phonons in diamond have demonstrated an emissive quantum memory [69], macroscopic entanglement [70], heralded single photons [67], and the frequency/bandwidth manipulation of single photons [71].

- **Switchable Cavities** - The most intuitive form of quantum memories takes its form as switchable cavities, single photons are switched into a cavity where they can be stored until needed, at which point they can simply be switched out. These systems are not truly on demand as the storage time will be in multiples of l/c where c is the speed of light and l is the path length of the cavity, leading to some level of determinism and they require an efficient and reliable single photon switch. These are discussed further in section 1.4 but in short a switch needs to have near unit efficiency in order to consistently operate the

memory at the single photon level as any substantial loss leads to a lost photon. Storage lifetimes are limited by this loss and are on the order of $1\mu s$. The mechanism limiting these memories is the switching mechanism, should a fast, fibre-based photonic switch with low loss be developed these systems will see huge developments.

There are two primary implementations of switchable cavity quantum memories. The first consists of two concatenated cavities with a switch that is able to change the resonant frequency of one to allow common modes between both allowing for switching between different outputs of the cavities [72]. The second uses a single cavity with a polarising beam splitter and a switch that changes the polarisation of the contained light to either reflect back into the cavity or to transmit out of it when incident on the polarising beam splitter [73].

- **Gradient Echo Memory (GEM)** - These systems can take place in a variety of materials with different methods but all work under the same principle. For this example, Rubidium is considered and a diagram is presented in figure 1.8. A magnetic field gradient is applied to a rubidium cell in order to change the transition energy so that it is able to absorb a spectrally broad pulse. Each atom that absorbs a photon will then begin to de-phase at a rate proportional to the strength of the applied magnetic field. At a time τ_s the gradient is applied in the reverse direction, allowing the atoms to gradually re-phase allowing for the re-emission of the input field at time $2\tau_s$ [74].

Limiting this technique is its bandwidth, which is low and results in the speed of the device being severely limited. Then, even if the storage time is significant, it is difficult to fit in an appropriate number of clock cycles.

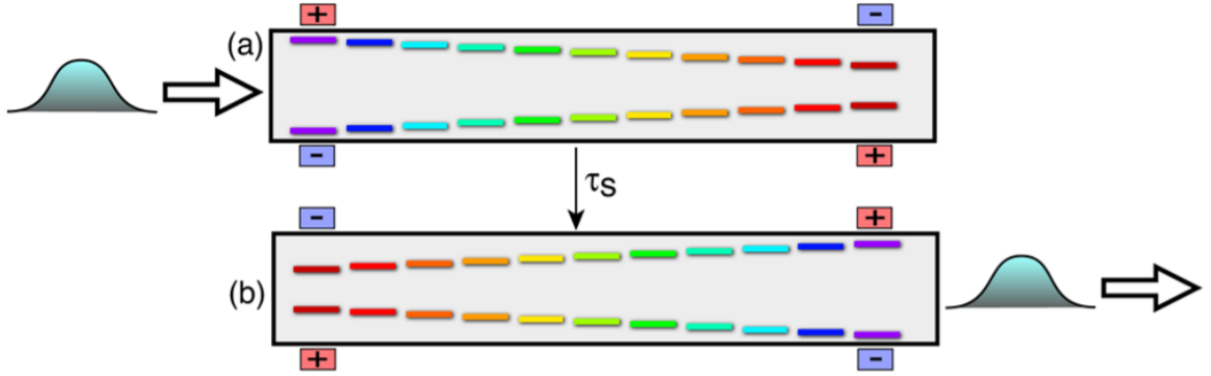


Figure 1.8: Induced broadening of a transition using an external magnetic field allows for broadband storage of a pulse. At time τ_s the field is reversed allowing the emission of the stored pulse at time $2\tau_s$. Reproduced from [73].

It is difficult to characterise the figures of merit for GEMs as there is a range of possible materials that can be used, all of which have varying figures for fidelity and storage times. It is easy, however, to present some of the best results gained using this method. Erbium doped Y_2SiO_5 is able to store information for up to 1.3s and fidelities of 0.97 are achievable in cold rubidium atoms [75].

• **Electromagnetically Induced Transparency (EIT)** - A material will become transparent when two fields (signal and control) resonant on separate transitions pass through a material simultaneously, causing quantum interference and dressing of the higher energy state, as a result, propagating light will pass through unperturbed [76]. This can be utilised as a quantum memory since a large change in absorption is correlated with a change in dispersion, from Ma *et al* [77], the group velocity of the signal beam is given by

$$v_g = \frac{c}{1 + g^2 \frac{N}{|\Omega|^2}}, \quad (1.22)$$

where g is the atom-field coupling constant, N is the total number of atoms, and Ω is the optical field detuning. By appropriately changing the atomic density or the control beam intensity it is possible to reduce the group velocity, slowing light down by 7 orders of magnitude and in some cases, halting movement entirely [78]. In the latter case, the control field intensity is reduced causing a proportionate reduction in group velocity and

the quantum information held in the signal beam is mapped onto the atoms through absorption. The control field can then be turned back on to re-emit the stored light thereby acting as a quantum memory [79].

Storage times are significant, with quantum memories lasting six hours in some circumstances [80], however the narrow linewidth of EIT severely limits the bandwidth of the memory [81], resulting in a memory that is only useful for specific applications.

1.4 Photonic Switching

In their most basic form, photonic switches are devices capable of re-routing light from one output to another, they have varying applications in both classical and quantum optics [72,82,83]. There are two important figures when discussing the efficacy of a photonic switch, these being switching time and optical power penalty. Ideally a switch will act instantly and have zero loss during its operation. The architecture of individual switches varies hugely, some of which are described further in section 1.4.1.

Large data centres used by technology companies such as Google, Facebook, and Amazon have recently moved away from copper wiring as their means of data communication in favour of fibre optics [84]. This progression is clear when considering the scalability of data centres and the users that utilise them. Intra-centre link rates have values upwards of 100Gbps (Giga-bits per second) and have link lengths that extend well beyond 2km [85]. The number of active internet users has been consistently growing at a rate of 6% per year [86], adding to the need for a scalable solution.

The inclusion of a photonic switch in these systems replaces the need to convert light into electricity in order to undergo a switching mechanism. This provides a solution to huge bottlenecks and is capable of limiting the power constraints of an electronic switch ASIC (application specific integrated circuits) as well as reducing inefficiencies associated with

opto-electronic conversions [87].

Photonic switching also has application in optical computing, where binary data is processed using optics rather than electronics. Not only will switching itself be essential in this process, but there are calls for optical transistors [88], whose functionality and physical dynamics will have large overlap with photonic switches. Reducing power consumption of photonic switches and transistors will lead to a viable competitor to electronic computing and so there is deep interest in finding the lower limit to how much light is able to trigger switching events. Photonic switching of coherent light using single photons was recently achieved by a group at IBM [89], representing the lowest possible energy consumption a switch can have.

There is also a great interest in finding a photonic switch for applications in LOQC, however the requirements are different to those discussed already in this section. These switches must be able to manage single photons at near unity efficiencies, any drop in efficiencies will add yet more indeterminism to the system, increasing the resources needed to accurately apply gate operations. This is a problem that is present in other switch applications, but is usually overcome with the use of an amplifier, which is not available when processing quantum information due to the no-cloning principle and the need for single photons. Photonic switches will find quantum applications in switchable cavity quantum memories (as already discussed) [72], the general re-routing of light as a system develops, as well as being necessary in the implementation of spatial multiplexing systems [90].

1.4.1 Photonic Switching Protocols

The following section briefly describes a range of possible photonic switching architectures, along with how useful their implementation will be for both classical and quantum applications.

- **Free-Space Micro-ElectroMechanical Systems (MEMS)** - The oldest of the photonic switches, they use arrays of micro-scale mirrors fabricated using etching techniques and controlled by electrostatic drivers to switch light into various output fibres [91]. 2D and 3D systems have been realised and are available commercially. Devices employing this technique have shown high port counts, up to 1100×1100 (1100 input fibres and 1100 output fibres) with a maximum insertion loss of 4dB and switching speeds of 5ms [92].

- **III-V Semiconductors** - Indium-Phosphide (InP) switches exist in a unique position as high performance optical amplifiers and lasers exist on-chip [93]. There are two switching mechanisms making use of this material, semiconductor optical amplifiers (SOA) switches and Mach-Zender interferometer (MZI) switches.

SOA switches work by broadcasting a pulse across a variety of outputs each with their own SOA, powering selected SOAs means that gain is only experienced by certain outputs and the extinction ratio of un-powered SOAs is large enough as to eliminate cross talk [94]. This has the potential to be entirely lossless and switches at speeds on the order of ns, there is a limit, however, to how many ports can be used as the size of the device has a square law increase in switch elements and a two-fold increase in 1×2 beam splitter and combiners, meaning that scaling beyond 4×4 switches is challenging if monolithic devices are to be fabricated [95]. The nature of the switching mechanism means that it is not at all suitable for sustaining quantum information.

The basic function of a MZI switch uses a phase change applied to one arm of a MZI to constructively or destructively interfere light at either output [96], leading to the effective switching of light. The largest MZI switch developed has an 8×8 [97] port structure however these switches experience large amounts of crosstalk between channels [98], severely degrading the output signal and limiting this architecture's capability. Proposals have been made to combine SOA and MZI structures in order to eliminate the crosstalk [99], physical implementations provide strong results with crosstalk being reduced almost entirely [100], drastically increasing the feasibility of III-V switches. These structures, how-

ever, still do not allow for the switching of single photons.

- **Silicon** - The infrastructure for silicon fabrication already has massive grounds in semiconductor chip manufacturing and as a result has generated huge interest in silicon photonics [95], a field that has recently experienced substantial growth. Silicon-based photonic switches can function in a variety of ways, three of which are discussed here and build on the implementations already discussed in this section.

Silicon based MZI switches work in the same way to those discussed for III-V materials. Modern implementations use 1024 MZI structures to create a 32×32 photonic switch [101, 102]. On-chip losses of $> 23\text{dB}$ are experienced with switching speeds of $750\mu\text{s}$ [102].

Micro ring resonators (MRRs) are waveguide rings that guide light at specific wavelengths according to the refractive index of the guiding material [103], this can function as a switch if the material comprising the MRR is non-linear, in which case a strong pump beam can be used to shift the refractive index and trigger coupling between MRRs and nearby waveguides on and off [104]. Switches employing this technique require wavelength uniformity and losses depend on the route through the switch, averaging 0.9dB [105].

MZI and MRR based silicon photonic switches act as both the propagating and redirecting element in the device, inducing loss and crosstalk at each event which harshly limits the port count scalability. By separating these elements, independent control over optimisation parameters is easily achieved [106, 107]. Some such systems are silicon integrated MEMS switches, shown in figure 1.9, grids of silicon waveguides are fabricated with adiabatic couplers above each intersection. Light can be switched easily by activating certain adiabatic couplers, leading to a 90° redirection into a separate and selected output port. The process is electrically controlled by adjusting the vertical spacing between propagation and redirection layers using a MEMS actuated cantilever.

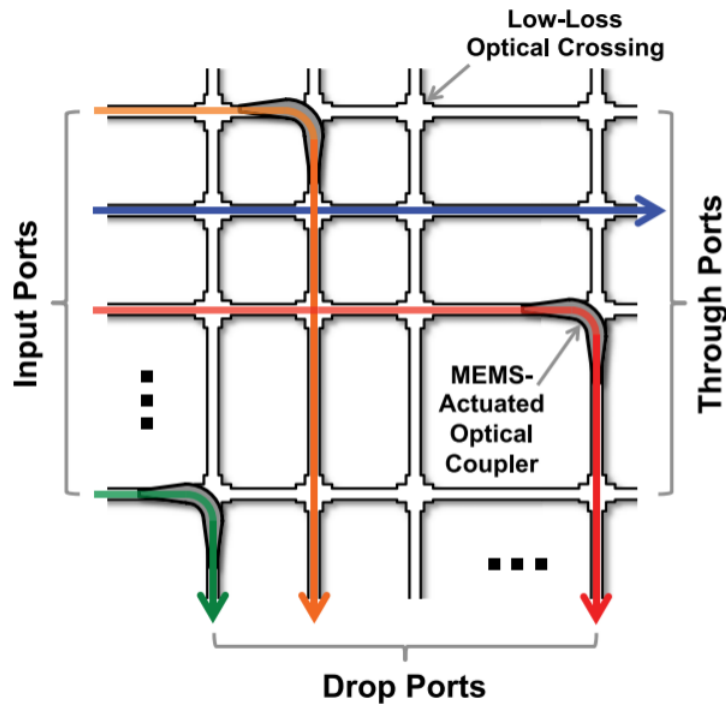


Figure 1.9: Light is able to be switched from through ports to specific drop ports by activating intergrated MEMS waveguides that moves closer to the device upon activation allowing for effective and low-loss switching between output ports. Reproduced from [106].

MEMS based silicon switches present switching speeds of up to $0.91\mu\text{s}$, extremely low losses of 0.028dB , and port counts scaled up to 64×64 . The total footprint of these devices is small, at 49mm^2 [107].

So far ignored in this discussion is a switch capable of switching individual photons reliably, there exist a number of different options from different groups. Yoshikawa *et al* [72] use an electro-optic modulator to change the resonance of a cavity, allowing photons to escape [108] and Kupchak *et al* [109] induce a birefringence in 10cm of single mode fibre using the Kerr effect (a non-linear effect, high powered light will change the refractive index of a material) allowing for switching on a polarising beam splitter.

1.5 Device Proposals

As described previously, the bulk of this thesis is dedicated to analysing the feasibility of two different devices that utilise Brillouin scattering in their operation, the following section seeks to give a detailed outline of these proposals.

1.5.1 Quantum Memory

A pump pulse and a single signal photon are incident on a diamond at the same time, allowing the pump pulse to store the photon in the crystal through a stimulated Brillouin interaction. After a time τ , a second pump pulse passes through the diamond stimulating the emission of the stored photon and allowing for the retrieval of the quantum information it holds. Figure 1.10 shows an energy diagram of this process, the interaction between the pump (dashed) and signal (bold) beams couples the ground and storage states, allowing for on demand storage and retrieval. Since the process is driven only by the detuning between pump and signal beams this memory is wavelength independent in its operation, but has an efficiency inversely proportional to the square of the wavelength, opening up the possibility of telecom operation.

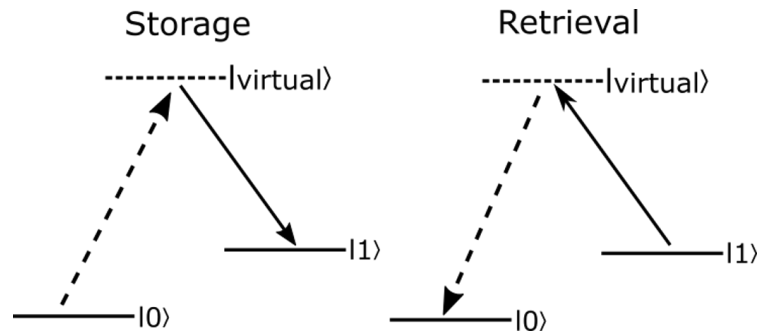


Figure 1.10: Energy level diagrams describing storage and retrieval of quantum information using acoustic phonons in diamond accessed by backwards stimulated Brillouin scattering. The dashed and bold arrows represent pump and signal beams respectively. Since the intermediate energy level is imaginary its location is not fixed, making this process wavelength independent.

In order to achieve this, a series of experiments must be completed in order to fully characterise the memory, the first of these is to measure the acoustic phonon lifetime in the diamond which sets the limit to the memories storage time. Physical realisation of

this experiment can be achieved in two different ways, the first uses a single laser and a modulator to achieve the necessary detuning needed for stimulated Brillouin scattering and the second uses two separate lasers to achieve this detuning. Both of these options are explored in chapter five and both produced unsuccessful results.

Once the value for acoustic phonon lifetime has been found, the infrastructure allowing for the storage of quantum information can begin to be put in place. The first step is to create a cavity for the sample, this has the effect of increasing the power in the diamond leading to a higher Brillouin gain, this cavity must be small to ensure both pump and signal beams are resonant and that the resonances have high enough bandwidths to incorporate short pulses. One way to achieve this is to fabricate small lenses into the surface of the diamond that will act as of the mirrors that make up the cavity.

Although more difficult to fabricate than other cavity designs, ring cavities are preferable as these allow for the interacting beams to be consistently counter-propagating, allowing for efficient probing of the diamond and the elimination of noise sources such as four-wave mixing.

Following the cavity enhancement of backwards stimulated Brillouin scattering in diamond, pulses will be employed in a similar manner to England *et al* [67] in order to store and retrieve light on demand. The delay between write and read pulses will be dictated by the acoustic phonon lifetime measured in earlier experiments.

Pulses can be created using a pulse carver allowing for more control over pulse shape and duration. This experiment will allow further characterisation of the quantum memory, including measurements such as readout efficiency.

Finally, the move will be made to single photons encoded with quantum information to analyse characteristics such as fidelity.

1.5.2 Photonic Switch

In 1996, Tim Birks *et al* used a null coupling fibre taper, a fibre beam splitter with no coupling between its cores consisting of two fused tapers with dissimilar diameters, along with an acoustic field induced by a piezoelectric transducer to switch light from one output to another. The second proposal present in this thesis analyses this system where the acoustic field created due to Brillouin scattering is used in place of a piezoelectric transducer. Such a device is expected to work at faster rates and higher efficiencies than its predecessor.

Two co-propagating pump fields detuned by the Brillouin frequency are directed into the two input ports of a null-coupling fibre taper inducing a high acoustic field amplitude via Brillouin scattering, after a short delay, a signal pulse (or single photon) enters the device through one arm, scatters off the induced acoustic mode into a higher order optical mode, and leaves the device through the opposed fibre. A diagram of this setup is shown in figure 1.11.

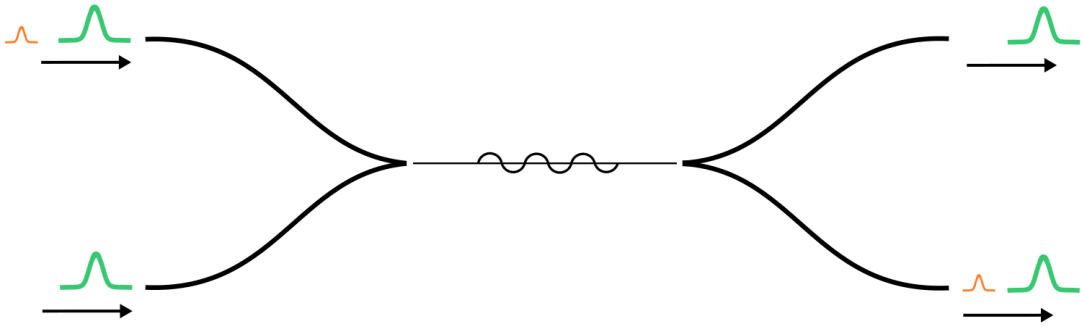


Figure 1.11: Launch conditions and mode of operation for a null-coupling fibre taper switch.

Similar to the memory proposal, there is a series of experiments that can be done in order to aid the progression of the device. The first of these, presented in chapter 7, is to measure Brillouin scattering through a single fibre taper. There is a trade off between length and diameter when considering the design specifications of a taper to be used in this experiment, lower diameters lead to a larger Brillouin gain but a reduced taper length, as fabricating long tapers at lower diameters becomes much more difficult.

The next step is to begin work on null-coupling fibre tapers, a simple experiment can take place to determine if intermodal scattering is taking place within the device. Two fields detuned by the acoustic field frequency are sent through the two separate input arms of a null-coupling fibre taper, intermodal scattering can be measured by analysing the relative power of the two output arms. If there is a significant change compared to the input powers then the desired outcome is achieved.

Based on the results of this experiment, pulses achieved in a similar manner to the proposed memory experiments can be used in the taper to confirm its efficacy at switching pulses and a device can be manufactured that employs a null-coupling fibre taper as a photonic switch. Finally, single photons can be used as a replacement for pulses to analyse the device's ability to switch quantum information. Such a device can be linked with a cavity to form a switchable cavity quantum memory or used stand alone as a quantum photonic switch.

Chapter 2

Laboratory Logistics and Rubidium Vapour

A large portion of this project was spent handling the logistical issues that arise when planning for multiple experiments using shared equipment, in total there are four major experiments that need to be taken into account when planning the layout of the optical setup. These are the two Brillouin scattering experiments that are described in this thesis featuring diamond and fibre tapers, and two quantum memory protocols that utilise rubidium in order to store and retrieve light.

Both rubidium quantum memory proposals are based on switchable cavities and are shown in figure 2.1, the first uses counter-propagating pump beams to form a spatially varying dispersion through warm rubidium vapour forming a Bragg mirror. Light can then be trapped in a cavity caused by this induced Bragg mirror and a permanent mirror, allowing for on demand storage and retrieval of a signal beam.

The second uses warm rubidium vapour in a cavity (figure 2.1b). Pump and signal beams are set to counter-propagate around the cavity, both fields interact with the rubidium in a two photon process causing a dispersion change resulting in the effective lengthening of the cavity and the changing of resonant frequencies,. Coupling this system to a second cavity then allows for an on-demand switchable cavity memory. A full theoretical and

experimental analysis of these systems is given by Page [110].

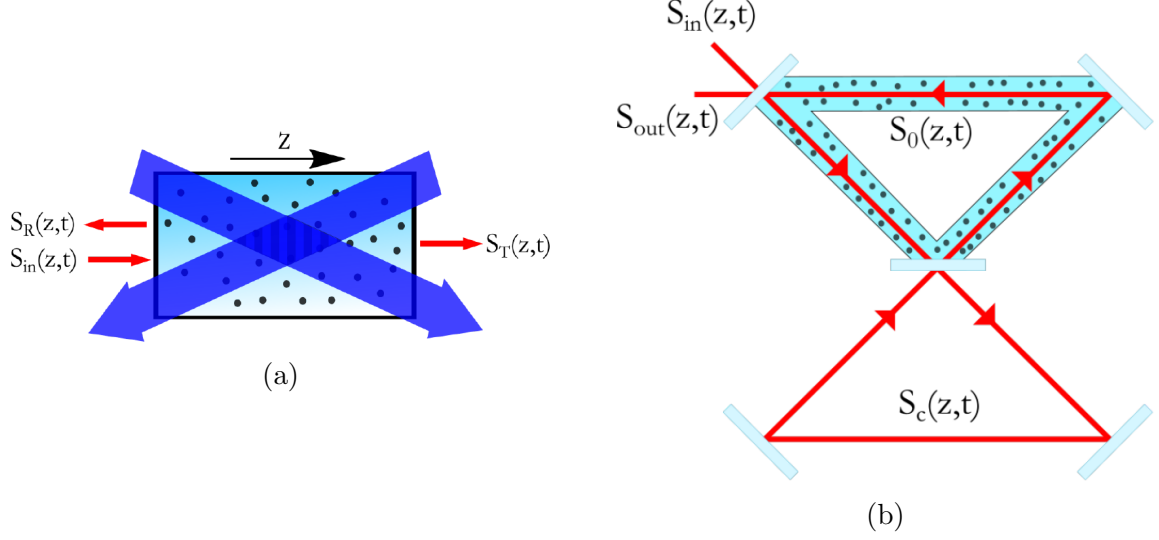


Figure 2.1: (a) Counter propagating pump beams induce a Bragg mirror in a rubidium vapour cell, light reflecting between this induced mirror and a fixed mirror is trapped and forms the basis for a quantum memory. (b) A strong pump field propagating through in cavity containing a rubidium vapour cell interacts with a signal field within the rubidium in a two photon process causing a dispersion change and the effective lengthening of the cavity, coupling this to a second cavity forms the basis for another quantum memory featuring rubidium. Recreated from [110].

Due to the complexity of the initial diamond experiment (discussed further in Chapter 5), significant time was spent performing preliminary experiments on rubidium as a prerequisite for the more complex diamond and rubidium experiments that were to come.

In this chapter, a detailed explanation of some of the experimental design decisions are given and how they have been implemented in a number of preliminary rubidium experiments along with an overview of the objectives associated with the various rubidium projects and how far along in the process these have gone. The work presented here was done in conjunction with Carlo Page and Tabijah Wasawo.

2.1 Common Laboratory Equipment and Techniques

During the early stages of this project, decisions had to be made regarding the equipment that was to be used for these experiments, with the additional caveat that it is to be shared across multiple experiments. The most clear example of this is the laser system, these had to be lasers with a tunability around 780nm – 776nm to coincide with the D_1 and D_2 lines of rubidium, they had to have narrow linewidths so that experiments involving both diamond and rubidium produced results as close as possible to the natural spectra of the materials. An additional but non-essential feature was for the lasers to allow automatic scanning across a range of frequencies, which would make both experiments significantly easier to execute. Economic issues must also be taken into account, an unfortunate yet very real aspect of academic research.

All three of these criteria were met with the tuneable cateye laser manufactured by MOGLabs, it produces a highly tuneable and low linewidth beam (100kHz) with the ability to scan over a region of 5GHz, these function by creating an external cavity using the rear reflecting surface of the semiconductor diode and a cat-eye reflector a few centimetres from the diode. The cat-eye reflector is placed on a piezoelectric actuator and so different cavity modes can be selected by applying various currents to the device, enabling the fine control of emission wavelength. The laser also contains a high efficiency ultranarrow filter in the external cavity that allows for the selection of a single external cavity mode, the transmission wavelength is angle dependent and can be manually rotated using a hex-bolt on the outside of the device [111]. Two of these lasers were purchased. The laser, containing everything described here, is shown in figure 2.2.

The laser is controlled using an external cavity diode laser controller also produced by MOGLabs, this device is able to control the diode injection current and the temperature of the laser. The output power of the diode follows a linear relation with injection current, the maximum current that the laser controller is able to apply to the diode is 200mA which results in an output power of around 140mW, output power can be finely

tuned by applying different currents to the diode. Since output wavelength relies heavily on cavity size, small thermal fluctuations will change the cavity length (and therefore wavelength) due to thermal expansion at a rate of 30GHzK^{-1} , a negative temperature coefficient thermistor is used with a Peltier thermoelectric cooler to monitor and change the temperature of the laser and the laser controllers low noise electronics contributes to the low linewidth and high stability of the laser. The laser controller is also the means by which a frequency scan can be achieved, by applying a sawtooth shaped current modulation to the piezoelectric actuator in the laser, the length of the cavity and therefore wavelength changes, the frequency of this sweep can be tuned from $4\text{Hz} - 70\text{Hz}$ [112].

Light could be sent to various points in the lab through a simple setup consisting of a polarising beam splitter, two quarter-waveplates, and a half-waveplate. The alternating waveplate configuration provides full polarisation control allowing all power to be directed in one of two directions regardless of input polarisation.

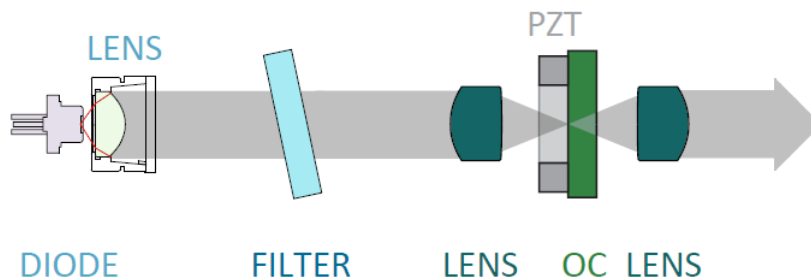


Figure 2.2: A diagram of the MOGLabs tuneable cateye laser, an external cavity is generated using the reflective surface on the back of the diode and a cateye reflector, wavelength can be changed coarsely using an in built wavelength filter or finely using a piezoelectric actuator. Reproduced from [111].

A means to frequently check the laser linewidth was found with the MOGLabs Economical Wavemeter, this is capable of measuring the input wavelength with an accuracy of $\pm 0.0001\text{nm}$ at picowatt powers and has a measurement rate of 1250Hz , this allows for the constant monitoring of the wavelength of light without sacrificing power and does not require intricate fibre coupling setups [113]. The wavemeter functions using a high resolution diffraction grating in a Littrow configuration, this is where the first order diffracted

beam is reflected at an angle equal to the angle of incidence, optical interference then creates an image of a singlemode fibre core at a wavelength dependent position on a semiconductor imaging sensor, the wavelength spectrum is then generated from that image and the peak power is found with a fitting procedure [113,114]. All MOGLabs products are able to work in conjunction with one another to automate the control of the wavelength and lock to various spectral lines in rubidium, further increasing the stability and convenience of the system.

Lock-in detection was used frequently throughout the project as a means to detect weak signals produced by the experiments. A carrier frequency is added to the optical field, when detected, the electronic signal is multiplied by a reference signal (equal to the carrier frequency) and integrated over time, the result is a DC signal that only contains components with the carrier frequency, anything else is attenuated to near zero [115].

A 160MHz carrier signal is applied to the signal beam using an acousto-optic modulator (AOM) these are devices that use physical sound waves to modulate light. An acoustic wave is set to propagate across a material using a piezo-electric transducer that causes a periodic refractive index change in the material, light then inelastically scatters off this refractive index modulation and a frequency sideband is added to the fundamental [116].

The modulator used here is the AOMO 3080-122 produced by Gooch and Housego, the device is made from tellurium dioxide and is driven at 80MHz. With only a single pass through the device, it is possible that the 80MHz sideband that is applied will interact unfavourably with the system as it is spectrally too close to the fundamental, by doubling this frequency to 160MHz through the use of a double-pass configuration it can be ensured that the sideband only used for aiding detection will not interfere with the rubidium hyperfine splitting of the D-state or the Brillouin linewidth of diamond and contradictorily add noise to the system.

Light passes into the AOM through one arm of a polarising beam splitter, a lens collimates

the fundamental and scattered beams and a quarter-wave plate turns the linearly polarised light into circularly polarised light which when incident on a mirror reverses polarisation direction, the light then traces the same path back through the device and exits through the second arm of the polarising beam splitter. There are different scattering efficiencies depending on polarisation, however they can be made equal with the fine tuning of the acoustic power caused by the transducer. This setup is shown in figure 2.3

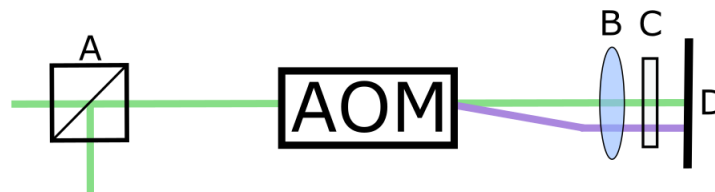


Figure 2.3: Double pass configuration for the AOM setup, light passes through the AOM twice to gain a 160MHz carrier frequency used later for lock in detection. A - Polarising beam splitter, B - collimating lens, C - quarter-wave plate, and D - planar mirror.

The final piece of shared equipment is the Liquid Instruments Moku:Lab, this is a reconfigurable hardware platform featuring twelve separate instruments that is accessible via an ethernet output or through an Apple iPad connected using Wi-Fi. The twelve devices are a lock in amplifier, arbitrary waveform generator, oscilloscope, frequency response analyser, waveform generator, PID controller, phasemeter, data logger, spectrum analyser, laser lock box, digital filter box, and FIR filter box. The large utility was countered by the relatively small bandwidth (250MHz), the low sampling rate (500MSas⁻¹), and the high input referred noise (60dBFS) [117]. The various experiments require different detection schemes and so this device is able to act in place of other cumbersome and expensive hardware, even with these issues the device produced data that was clear enough for the intended applications and the additional convenience due to the connected iPad was appreciated when sharing equipment.

2.1.1 Saturated Absorption Spectroscopy

All experiments presented in this thesis require detection with a high frequency resolution in order to accurately characterise the materials. In diamond for instance, the large

frequency detuning of 108GHz would usually require an ultrafast oscilloscope to accurately probe, but these are hugely expensive and are therefore not a viable option. Instead, the absorption spectrum of rubidium is probed at the same time as the signal frequency is swept through the Brillouin linewidth and data sets are combined to form an accurate frequency scale.

This is also necessary in the rubidium quantum memory experiments, having a separate system with the specific goal of ensuring the fields are on resonance with these transitions solves issues regarding guess work when experiments take place. Just as before, the absorption spectrum of rubidium acts as a frequency fingerprint that allows for better control over experimental systems. The hyperfine spectrum of rubidium can also be used to calibrate the wavemeter, which drifts slowly.

The fine structure alone does not allow for a high enough resolution to accurately apply these techniques, instead, the hyperfine structure of rubidium is looked at using a process called saturated absorption spectroscopy. Further to spin-orbit coupling, there is an additional splitting of degenerate energy levels that is orders of magnitude weaker, caused by coupling between the nuclear spin and the angular momentum of electron orbitals [118].

Rubidium has two common isotopes, Rb^{85} and Rb^{87} that have different nuclear spin of $I = 5/2$ and $I = 3/2$ and natural abundances of 72% and 28% respectively. This difference in nuclear spin results in the two hyperfine states of the $5S_{1/2}$ to have a splitting of 3.04GHz and 6.83GHz respectively [119, 120]. Shown in figure 2.4 is the full energy level diagram for the D_2 line of Rb^{85} , included are all possible transitions between the hyperfine energy levels of the two states.

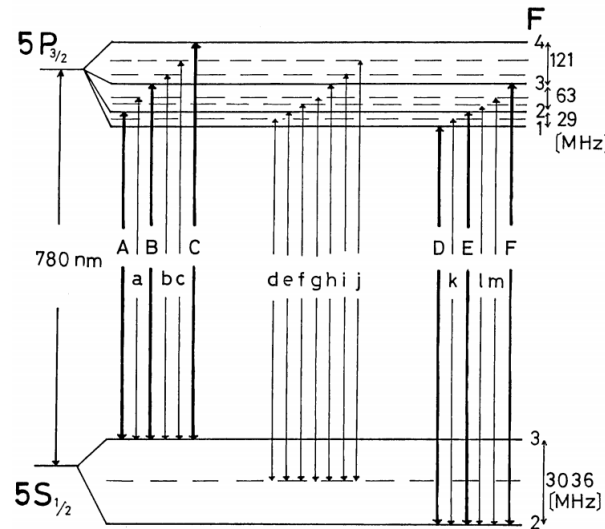


Figure 2.4: Full energy level diagram of Rb^{85} , featuring all hyperfine levels and all possible transitions between the two states. Reproduced from [121].

Doppler broadening is a common effect in experimental atomic physics, emission lines are broadened due the high speed at which atoms move and so the wavelength of the emitted photon is either blue- or red-shifted depending on the direction of travel and the direction of emission. This process leads to hyperfine emission lines becoming too broad to be detected using conventional means, but with a saturated absorption setup, this broadening can be overcome.

The rubidium used in the following experiments was purchased from Precision Glassblowing, who manufacture a variety of vapour cells for use in academic research. This company are able to supply isotopically pure samples as well as those with a natural abundance of isotopes, end-caps can be covered in an anti-reflective coating and angled to reduce reflections as much as possible. Here, vapour cells containing rubidium at natural isotopic abundance are used, with an anti-reflection coating for light of wavelength 780nm and planar end-caps.

A high powered pump beam and a low powered signal beam of identical wavelength are set to counter-propagate through a rubidium vapour cell, only atoms with a longitudinal velocity of zero observe both pump and signal beams as having the same wavelength, when

the signal beam encounters one of these atoms there is a high chance it has already been excited by the pump beam allowing the signal beam to pass through and experience less absorption. The resulting absorption profile experienced by the signal beam consists of the Doppler broadened fine structure with hyperfine peaks at their associated frequencies. It is these small and sharp atomic features that can be used in the above way. This optical setup is shown in figure 2.5.

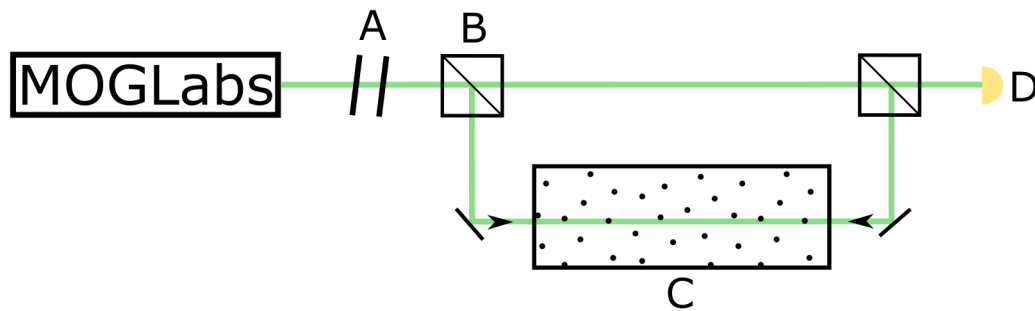


Figure 2.5: Saturated absorption spectroscopy setup, a strong pump beam saturates the D_2 transition allowing a weak signal beam to pass through with fewer interaction, they are counter-propagating to reduce Doppler broadening and produce a spectrum exhibiting the hyperfine transitions as a result. A - Polarisation control, B - Polarising beam splitter, C - rubidium vapour cell, and D - photodiode.

The results of this experiment, given in figure 2.6, shows the absorption spectrum for a signal beam sweeping frequency across the D_2 line of Rb^{85} with both the pump beam on and off and the hyperfine structure that arises as a result. Large dips on the left and right of the spectrum show the transitions $5S_{1/2}, F = 3 \rightarrow 5P_{3/2}$ and $5S_{1/2}, F = 2 \rightarrow 5P_{3/2}$, also shown are the transitions between $5S_{1/2}$ and $5P_{3/2}$ hyperfine states, these are $5S_{1/2}, F = 3 \rightarrow 5P_{3/2}, F = 2, 3, 4$ and $5S_{1/2}, F = 2 \rightarrow 5P_{3/2}, F = 1, 2, 3$, labelled A, B, C, D, E, and F.

The spectrum gained here is enough to accurately calibrate the wavemeter and to act as a frequency fingerprint for the fine probing of other experiments. This experiment was made to produce larger and more distinct peaks later on by others working on the project with the addition of a different detector and better experimental technique, allowing for a more reliable way to apply this information to the associated applications.

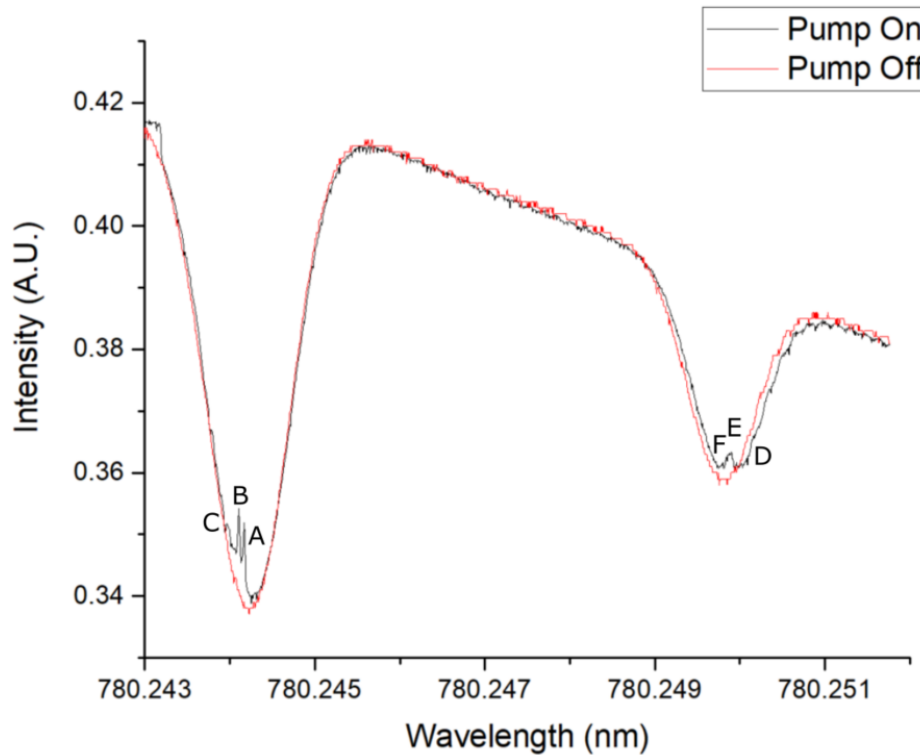


Figure 2.6: Absorption spectrum of rubidium as measured using a saturated absorber, when a strong pump field saturates the transition, the underlying hyperfine spectrum becomes clear.

2.1.2 Two-Photon Absorption

As well as the single-photon process described above, two-photon processes are also intrinsic to the rubidium based experiments and so two-photon absorption of rubidium is observed as a precursor to larger, more complex rubidium experiments. Two-photon absorption is a process analogous to single-photon absorption where two photons are absorbed by a material at the same time, the energies of the two photons linearly combine to mediate a transition that would otherwise not occur.

In rubidium, both the D_1 and D_2 lines are excited simultaneously using light of wavelengths 776nm and 780nm (referred to as control and signal field respectively), electrons in the excited state can decay through the original intermediate state or through the $6P_{3/2}$ state (as well as other, less common relaxation paths), the latter contains two transitions

occupying the $5D_{5/2} \rightarrow 6P_{3/2}$ and $6P_{3/2} \rightarrow 5S_{1/2}$ states and emit photons of wavelengths $5.2\mu\text{m}$ and 420nm respectively. This is used to judge the efficacy of the process, with strong blue light emitting from the rubidium cell when the fields are on resonance. An energy level diagram showing the dynamics of two-photon absorption in rubidium is presented in figure 2.7.

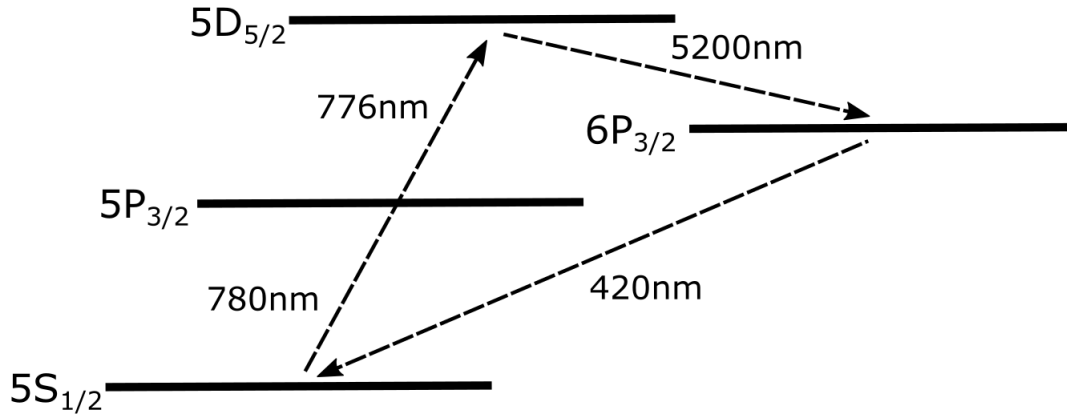


Figure 2.7: Energy level diagram for rubidium featuring two-photon absorption from $5S_{1/2}$ to $6P_{3/2}$ states and the decay path through the $6P_{3/2}$ that produces light of wavelength $5.2\mu\text{m}$ and 420nm .

Once again, two beams of appropriate wavelengths are set to counter-propagate through a rubidium vapour cell in order to reduce Doppler broadening, there is a slight detuning applied to the signal beam so that single-photon absorption does not dominate the process, the control beam is also detuned by the same amount to induce the two-photon process. Figure 2.8 shows the optical configuration of this experiment. This experiment produces a positive result in the way of a clear blue glow being emitted from the vapour cell (unfortunately not photographed).

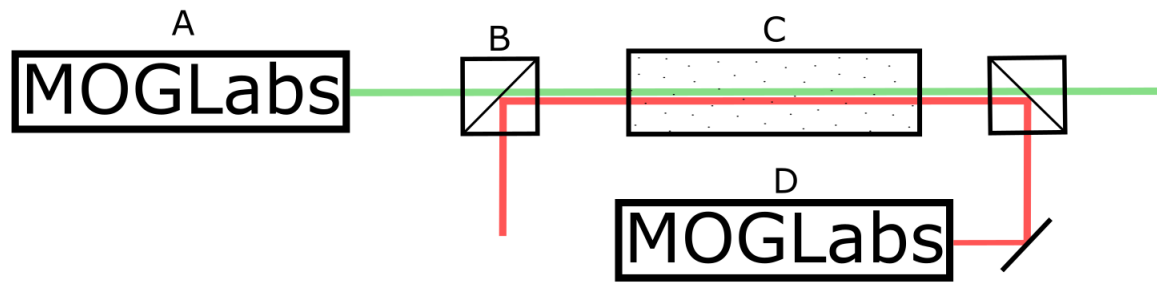


Figure 2.8: Diagram of the two-photon absorption set up, featuring A - MOGLabs laser set to a wavelength of 780nm, B - polarising beam splitter, C - rubidium vapour cell, and D - MOGLabs laser set to a wavelength of 776nm.

2.2 Current and Further Work

There has already been a substantial effort to advance the work detailed in this chapter, but the author has not been directly involved with it.

The induced susceptibility in rubidium has been characterised and a ring cavity containing a rubidium vapour cell has been built, early experiments have been completed to test the change in transmission through the cavity when a pump beam is turned on and off. Both of these experiments go a long way towards the goals described at the beginning of this chapter, however they are far from complete. While these experiments were taking place, progress was also being made towards the Brillouin memory and switching proposals, which the remainder of this thesis is dedicated to.

Chapter 3

Non-Linear Optics and Stimulated Brillouin Scattering

Light propagating through a material will occasionally scatter off localised non-uniformities such as particles, molecules, density fluctuations, and other similar features, this scattering can take various forms depending on a variety of factors such as whether the process is elastic or inelastic, and particle size relative to wavelength. Rayleigh scattering describes the elastic scattering of light and is the most common type, induced when light scatters off particles much smaller than its wavelength.

Raman scattering is the inelastic scattering of light [122], in this case the light incident on a material produces an optical phonon when it is scattered, thereby losing a some of its energy. The same process can also happen in reverse, where light scatters off an already present phonon caused by thermal energy within the system and gains energy during the process. These two scattering mechanisms are named Stokes and anti-Stokes scattering respectively, anti-Stokes scattering happens more readily due to the excess number of thermal phonons present in a material and the ratio of Stokes to anti-Stokes scattering can be used to find the temperature of a material to a high degree of accuracy [123].

Brillouin scattering is another inelastic scattering event, this time interacting with acoustic phonons in a material, as a result, Brillouin scattered light has a much lower frequency

change compared to Raman scattered light, as the phonons themselves contain less energy. These scattering mechanisms and the associated energies can be seen in figure 3.1.

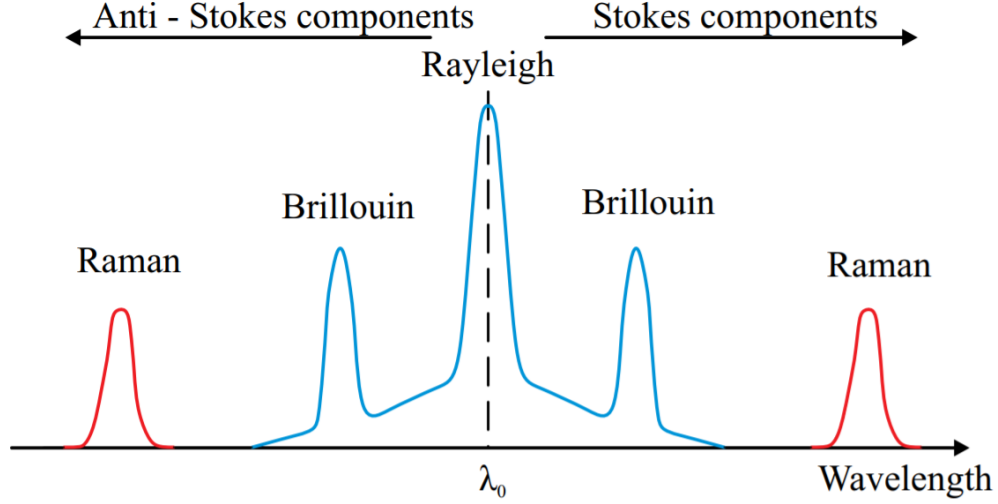


Figure 3.1: Spectrum displaying Rayleigh, Brillouin, and Raman scattering with the approximate changes in energy the light will undergo during a scattering process. Recreated from [124].

It is Brillouin scattering that is of particular interest, as it makes up the foundational physics for the devices presented in this thesis.

Essential to this process are phonons, quasiparticles consisting of large scale lattice vibrations in a crystal. They arise as a result of the Lennard-Jones potential, each atom in a crystal applies soft attractive and repulsive forces to atoms around it caused by Van der Waals forces and the need to eliminate the overlapping of electron orbitals respectively, the result of this is an array of potential wells in which each atom sits. Since these wells are shallow, atoms are able to move freely within them which in turn affects the position of nearby potential wells and causes waves to propagate through the material [125].

Phonons fall into two categories based on their movement patterns, optical and acoustic phonons. For an ionic crystal with atoms of alternating charge, atoms in an optical phonon will move against each other and will have a fixed center of mass, this type of motion is able to be excited with the electric field of a light wave. The atoms in an acoustic

phonon move with each other and have an oscillating center of mass much like in long wavelength acoustic vibrations, hence their name. Figure A.5 shows a dispersion curve of a 1-dimensional diatomic chain of atoms, which describes the relationship between frequency and wavevector of acoustic and optical phonons.

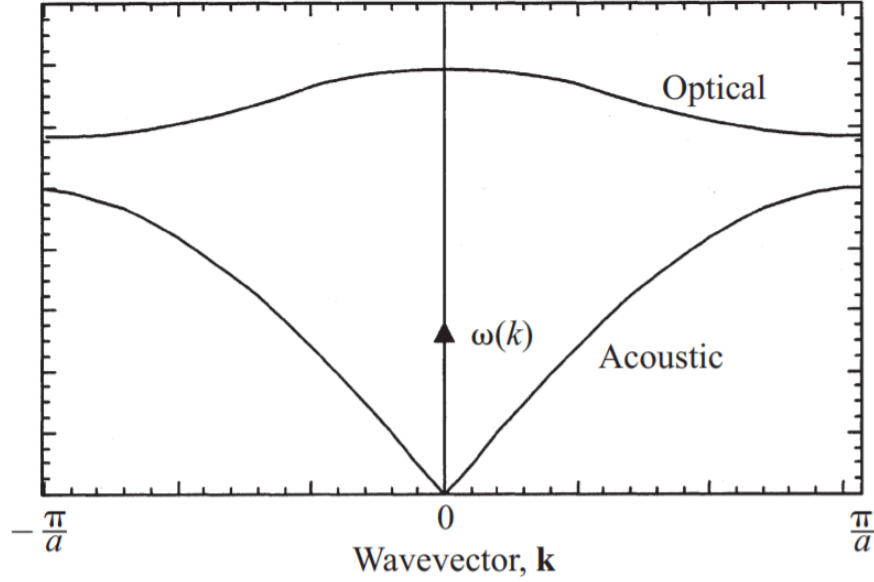


Figure 3.2: Dispersion curve caused by a one-dimensional chain of atoms with alternating high and low masses as described by equation 3.9. The higher frequency band is caused by optical phonons and the lower is caused by acoustic phonons. Recreated from [126].

Brillouin scattering will occur spontaneously, and is often the cause of noise in long distance fibre communications [127], however it is possible to stimulate the process under the correct circumstances causing a resonant energy transfer between electromagnetic fields mediated by a acoustic field. There are three components of Stimulated Brillouin Scattering (SBS), the combination of which produces the effect, these are bulk electrostriction, boundary electrostriction, and radiation pressure.

Electrostriction is the the tendency of a dielectric material to compress under a high local electric field leading to areas of higher density. It is a non-linear effect, meaning that the strength of the interaction has a non-linear relation with electric field strength. More precisely, it is a non-linear interaction between polarisation (in this context referring to the induced electric dipole moment per unit volume) and electric field strength, described

by expressing polarisation, $\mathbf{P}(t)$, as a power series in the field strength $\mathbf{E}(t)$

$$\mathbf{P}(t) = \epsilon_0(\chi^{(1)}\mathbf{E}(t) + \chi^{(2)}\mathbf{E}^2(t) + \chi^{(3)}\mathbf{E}^3(t) + \dots), \quad (3.1)$$

here ϵ_0 is the permittivity of free space, $\chi^{(1)}$ is the linear susceptibility, and $\chi^{(2)}$ and $\chi^{(3)}$ are the second- and third-order non-linear optical susceptibilities. The physical origin of the various linear and non-linear susceptibilities comes from a materials symmetry and how a atom is able to oscillate in a potential well, for condensed matter, $\chi^{(1)}$ is unity, and higher order susceptibilities $\chi^{(2)}$ and $\chi^{(3)}$ are on the order of 10^{-12} and 10^{-24} respectively. An assortment of effects arises as a result of non-linear optics, including second harmonic generation [128], optical parametric oscillation [129], and sum- and difference-frequency generation [130].

Described first is bulk electrostriction. Consider two beams of different wavelength passing through a bulk material and occupying the same spacial mode, a high powered pump beam with amplitude, frequency, and wavevector $(E_p, \omega_p, \mathbf{k}_p)$, and a low powered signal beam with amplitude, frequency, and wavevector $(E_s, \omega_s, \mathbf{k}_s)$. As these two beams propagate they will beat together to form a standing wave, which will induce a periodic density variation caused by electrostriction. When the frequency difference between the pump and signal beam is equal to the frequency of a phonon mode (u, Ω, \mathbf{q}) in the material, a resonant energy transfer takes place to dramatically boost the power of the signal beam. There are a number of selection rules associated with this process accounting for the conservation of energy and momentum

$$\Omega = \omega_p - \omega_s \quad (3.2)$$

$$\mathbf{q} = \mathbf{k}_p + \mathbf{k}_s. \quad (3.3)$$

The bulk electrostrictive force can be found using the electrostriction tensor, σ_{ij} , and has components

$$f_x^{ES} = -iq\sigma_{xx} - \partial_y\sigma_{xy} - \partial_z\sigma_{xz} \quad (3.4)$$

$$f_y^{ES} = -iq\sigma_{xy} - \partial_y\sigma_{yy} - \partial_z\sigma_{yz} \quad (3.5)$$

$$f_z^{ES} = -iq\sigma_{xz} - \partial_y\sigma_{zy} - \partial_z\sigma_{zz}. \quad (3.6)$$

For larger materials, the bulk electrostriction component of SBS far exceeds the boundary electrostriction and radiation pressure components, however when devices begin to reach nanometer scales the two boundary effects vastly outweigh the bulk electrostriction component due to an excess of material boundaries. The discontinuity of optical powers and photoelastic constants generates stress (and therefore electrostrictive forces) that contribute to the overall effect, the boundary electrostrictive forces can again be found with the electrostriction tensor, this time with components

$$F_i^{ES} = (\sigma_{1ij} - \sigma_{2ij})n_j, \quad (3.7)$$

where n_j is a normal vector that points from material 1 to material 2. When an electromagnetic field is incident on a material interface, there is an exchange of momentum between the field and the material resulting in a mechanical pressure being exerted on the material, this is known as radiation pressure and makes up the final component of SBS. The forces associated with radiation pressure can be derived from the Maxwell Stress Tensor (MST), a second-order symmetric tensor that represents the interaction between electromagnetic forces and mechanical momentum. The electric part of MST is

$$T_{ij} = \epsilon_0\epsilon(E_iE_j - \frac{1}{2}\delta_{ij}E^2), \quad (3.8)$$

where δ_{ij} is the Kronecker delta. The pressure between material 1 and 2 is

$$F_i^{RP} = (T_{2ij} - T_{1ij})n_j. \quad (3.9)$$

From these, Brillouin gain can be found, which is equal to the ratio of the input and output signal field powers.

$$g = \frac{2\omega Q_m}{\Omega^2\nu_{gp}\nu_{gs}} \frac{|\langle \mathbf{f}, \mathbf{u}_m \rangle|^2}{\langle \mathbf{E}_p, \epsilon \mathbf{E}_p \rangle \langle \mathbf{E}_s, \epsilon \mathbf{E}_s \rangle \langle \mathbf{u}_m, \rho \mathbf{u}_m \rangle}, \quad (3.10)$$

where Q_m is the mechanical quality factor, ν_{gp} and ν_{gs} are the group velocities of the pump and Stokes fields respectively, \mathbf{f} is the total optical force generated by pump and Stokes fields, and \mathbf{u} is the elastic deformation induced by \mathbf{f} . SBS falls in to two categories depending on launch conditions. When the pump and signal beams are counter-propagating through a material, the process reverses the direction of travel of the scattered light, and when the pump and signal beams are co-propagating through a material the process does not reverse the direction of travel of the scattered light. This is known as backwards stimulated brillouin scattering (BSBS) and forward stimulated brillouin scattering (FSBS) respectively.

BSBS and FSBS have slightly varying dynamics, where there are contributions to BSBS from bulk electrostriction, boundary electrostriction, and radiation pressure, but FSBS only has contributions from the boundary effects and so only interacts with transverse acoustic fields.

Additionally, FSBS can be split into two further characterisations referred to as intramodal and intermodal scattering, as the name implies, intramodal scattering happens when pump and signal fields occupy the same spatial mode, whereas intermodal scattering happens when pump and signal fields occupy different spatial modes.

A full quantum mechanical description of stimulated Brillouin scattering can be given that derives the Hamiltonian and the various equations of motion. Beginning with the Hamiltonian, which is described as

$$H = H^{\text{ph}} + H^{\text{opt}} + H^{\text{int}}, \quad (3.11)$$

where H^{ph} , H^{opt} , and H^{int} are the terms used to describe the acoustic field, optical field, and the acousto-optic interaction respectively. Expanding this following the derivation in Appendix A gives

$$\begin{aligned}
H = & \int dz \hbar b^\dagger(z) \hat{\Omega}_z b(z) \\
& + \sum_{\gamma} \int dk \hbar \hat{\omega}_z a_s^\dagger a_s \\
& + \sum_{\gamma, \gamma', \alpha} \int \frac{dk dk' dq}{(2\pi)^{3/2}} a_s^\dagger a_{as} b \int V(\gamma k; \gamma' k'; \alpha q) e^{i(k' - k + q)z} dz \\
& + \sum_{\gamma, \gamma', \alpha} \int \frac{dk dk' dq}{(2\pi)^{3/2}} b^\dagger a_{as}^\dagger a_s \int V^*(\gamma k; \gamma' k'; \alpha q) e^{-i(k' - k + q)z} dz
\end{aligned} \tag{3.12}$$

where z is the longitudinal position, b , a_s , and a_{as} are the phonon, pump, and signal field mode envelopes, G is the coupling parameter, α is the acoustic mode index, and γ is the electromagnetic mode index. Using this, the Heisenberg equations of motion for pump, signal, and acoustic fields can be derived, for backwards Brillouin scattering, ignoring the anti-Stokes scattered field and obeying the selection rules (equations 3.2 and 3.3), the equations of motion are then

$$\begin{aligned}
\frac{\partial B}{\partial t} - v_0 \frac{\partial b}{\partial z} &= i(\Omega - \Omega_0) b + iG^* a_{as}^\dagger a_s \\
\frac{\partial a_s}{\partial t} + v_p \frac{\partial a_s}{\partial z} &= iG a_{as} b \\
\frac{\partial a_{as}}{\partial t} - v_s \frac{\partial a_{as}}{\partial z} &= iG^* b^\dagger a_s.
\end{aligned} \tag{3.13}$$

Using the same criteria for forward Brillouin scattering, the equations of motion are

$$\begin{aligned}
\frac{\partial b}{\partial t} + v_0 \frac{\partial b}{\partial z} &= i(\Omega - \Omega_0) B - iG^* a_{as}^\dagger a_s \\
\frac{\partial a_s}{\partial t} + v_p \frac{\partial a_s}{\partial z} &= -iG a_{as} b \\
\frac{\partial a_{as}}{\partial t} + v_s \frac{\partial a_{as}}{\partial z} &= -iG^* b^\dagger a_s,
\end{aligned} \tag{3.14}$$

where G is related to Brillouin gain g by the equation

$$g = \frac{4|G|^2}{v_s v_p \Gamma_m \hbar \omega_p} \frac{\left(\frac{\Gamma_m}{2}\right)^2}{(\Omega - \Omega_0)^2 + \left(\frac{\Gamma_m}{2}\right)^2}. \tag{3.15}$$

3.1 Applications of Stimulated Brillouin Scattering

The applications of SBS are numerous, presented here is a brief review of the various avenues in which SBS can be used. Garmire [131] describes nine separate applications of SBS that are characterised by how the process interacts with the medium, these are spatial dependence, time dependence, frequency dependence, linewidth dependence, background noise, the physical hypersonic waves, SBS signal amplitude, micro devices, and nanostructures.

- **Spatial dependence** refers to the control of the spatial phase front of a coherent beam. A phase distortion is applied to a wavefront as it passes through a phase abberator such as a laser gain medium which is unfortunate for systems in which a high powered beam is necessary. This can be fixed by using an SBS Phase Conjugate Mirror (PCM), which employs the phase shift gained from SBS to ‘reverse’ the phase distortion of the wavefront, the beam then passes through the medium a second time resulting in an output wavefront equal to the input wavefront. The scattered light introduces a π phase shift and induces conjugation in the the light, the correction is caused by the selective amplification of a wave that has a wavefront approximately conjugate to that of the incident pump field [132].

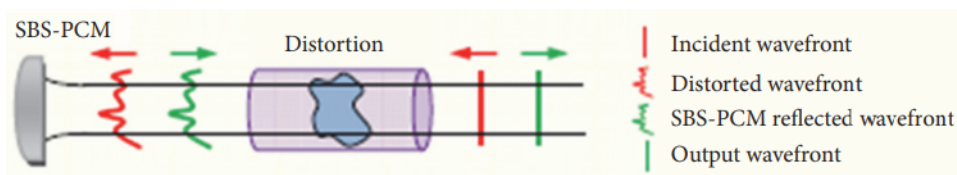


Figure 3.3: Diagram describing the effects of a stimulated Brillouin scattering phase conjugate mirror on a distortion picked up by a plane wave as it passes through a medium. Replaced from [133].

- **Time dependence** applications are able to shorten pulses significantly, experimental data from Bai *et al* [134] shows pulses of 7.8ns being shortened to 450ps, this occurs in a simple BSBS process where the long pump field is almost entirely converted into a short signal field, thus reducing the pulse duration.

- **Frequency dependence** is useful in sensing applications because of the frequency shift dependence of SBS on refractive index. This results in small variations in refractive index in a material to be easily detected, contributions to this refractive index change come mainly from temperature or local stresses.
- **Linewidth dependence.** Counter to other methods in this list, the linewidth dependence of SBS can be used to suppress the noise that occurs in long distance fibre communications, rather than being the source of an application itself. Since the SBS response is Lorentzian, a wider FWHM will lead to a lower peak value, drastically reducing the gain a beam will experience.
- The **background noise** of SBS processes are incredibly low, as the spontaneous process is negligible compared to the stimulated process. Instead it is the thermal phonons that initiate the process, representing the final limit of low noise [131].
- The **physical hypersonic waves** that SBS produces have their own interesting properties and applications, often employed by material scientists, these physical acoustic waves have enhanced spatial resolution and are able to separate strain and temperature leading to diverse fibre sensors. They are also easy to induce, all that is needed is two interacting electromagnetic fields [131].
- **Amplitude of SBS signal** can be used to enhance other non-linear signals. For example, dynamic control of phase is possible using SBS, meaning that the phase matching conditions for four wave mixing (FWM) can be easily met and controlled leading to longer interaction lengths and lower powers [135].

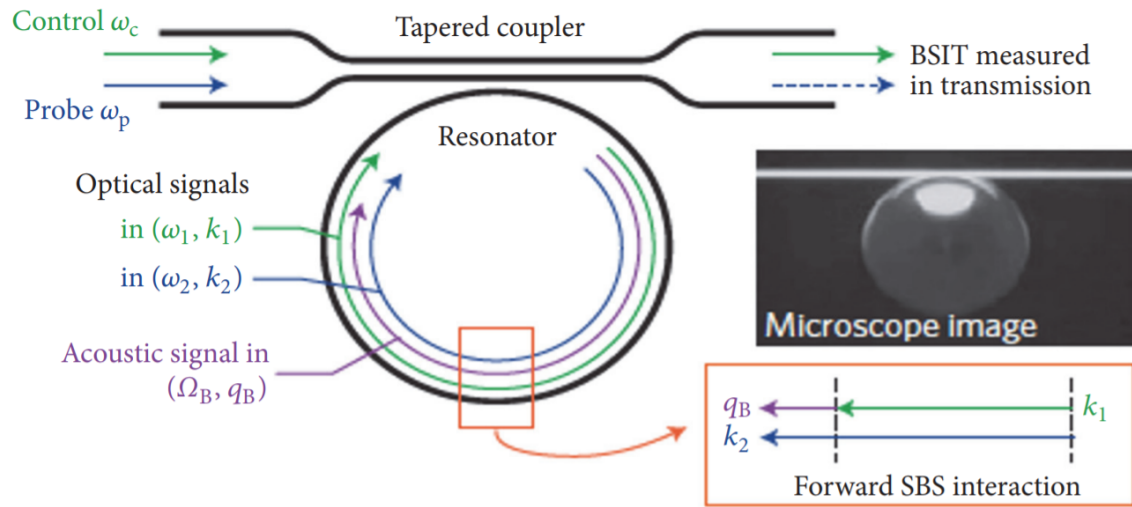


Figure 3.4: Various whispering gallery modes in $100\mu\text{m}$ diameter silica balls cause a FSBS signal and generate an induced transparency. Replaced from [135].

- **Micro devices.** The usefulness of microscale devices is exemplified by $100\mu\text{m}$ diameter silica balls. Phase matched pump and signal fields travelling in whispering gallery modes in these resonators produced acoustic fields as in FSBS leading to FSBS induced transparency. This is usually an effect reserved for atomic physics, powerful enough light passing through a material will excite atoms into higher energy levels leaving nothing for the following light to interact with, this is the case as well for SBS but acts on acoustic phonons instead of atoms [136].

- **Nanostructures.** The huge increase in radiation pressure forces, and therefore Brillouin gain, at nanoscale material geometries can lead to some interesting results, and presents a huge opportunity for the future of this research [131, 137].

Chapter 4

A Finite-Element Analysis of Brillouin Scattering: Diamond

Theoretical work is often used alongside experiments to gain information that sometimes isn't possible in a laboratory environment, parameters can be changed easily and physical systems can be created that would take months of planning and significant resources to create.

In the following chapter, finite element analysis is introduced and applied to BSBS in diamond in order to simulate the experiments outlined in Chapter Five. The results of these simulations show what is expected to be found when looking for the Brillouin linewidth in the diamond, and allows for an analysis of the feasibility of a device utilising this effect.

4.1 FeNICS and PySBS

FeNICS (Finite Elements nurtured in Computer Science, or For Everything new in Computational Science) is open source software used for automatically finding solutions to differential equations. While the vast majority of the computation is done in C++, FeNICS provides a python front end to allow for a low barrier of entry and for easy integration into other systems. There are various components of FeNICS that are used to

achieve this goal, these are; DOLFIN (Dynamic Object-oriented Library for Finite Element Computation) - the high performance C++ backend of FeNICS and functions as the primary problem solving environment, it also compiles the various other components of the package and communicates with external libraries, UFL (Unified Form Language) - this implements the often complex mathematical language that is expressed in Python and used in problems FeNICS is adept at, FFC (FeNICS Form Compiler) - acts as a code compiler, taking UFL inputs and outputting UFC, UFC (Unified Form-assembly Code) - takes inputs from FFC and compiles them into simple C++ code used for evaluating and assembling finite element variational forms, FIAT (Finite element Automatic Tabulator) - this is the finite element backend of FeNICS. There are other, less essential components as well that account for jobs such as meshing algorithms and linear algebra.

FeNICS has been used for a range of different applications in both industry and academia, including simulating thermomechanical problems of turbomachinery which until the implementation of FeNICS was not considered a problem accurately solved by FEA [138], high accuracy simulations of jet engines [139] and full aeroplane flight [140], and biomedical fluid modelling of patients [141].

PySBS is a Python package that works in conjunction with FeNICS to provide a complete simulation of Stimulated Brillouin Scattering events in waveguides [142]. It is split into four primary sections, an elastic mode solver, an electromagnetic solver, an electrostriction forces solver, and a Brillouin gain solver, the package can also handle both forwards and backwards Brillouin interactions.

In a head to head comparison to another more popular FEA software, COMSOL, PySBS was able to produce identical results while saving significant amounts of time and computational power [142], as a result PySBS was chosen over COMSOL for the simulations present in this thesis.

Both the elastic mode solver and the electromagnetic mode solver use FeNICS in order to

solve for various geometries, specifically they use a weak form approximation. In order to save computation time, exact solutions to complex differential equations can be ignored in favour of weak solutions with respect to certain test functions, these weak formulations allow the transfer of concepts from linear algebra to solve problems that arise when solving differential equations. This is in contrast to strong formulation, where exact solutions are necessary. Weak formulation provides near-perfect solutions with the benefit of saving computation time, and so is standard practise in the FEA field.

Acoustic resonances depend on crystal orientation, while previous computational analyses of acoustic modes in materials have assumed an isotropic medium ensuring that computation times are kept low, which is well justified as it results in values that are qualitatively acceptable, there is some variation in the frequency shift for the same acoustic mode at different crystal orientations. The Brillouin gain that is experienced by a particular acoustic mode is inversely proportional to the Brillouin frequency, and so variations in Brillouin frequency will result in variations in the Brillouin gain, an important figure when discussing the efficacy of Brillouin based quantum memory and photonic switching systems. The constitutive equation of motion for an elastic medium is [143]

$$\nabla \cdot \sigma = \rho \frac{\partial^2 \mathbf{u}}{\partial t^2}, \quad (4.1)$$

where σ is the stress, ρ is the density, u is the displacement vector, and t is time. This is translated into a weak form approximation allowing the eigenvalues to be calculated, which correspond to the frequency of a particular acoustic mode to be calculated, as well as the power of a particular mode to be calculated, both of which are necessary in order to calculate Brillouin gain, as per equation A.31.

The electromagnetic mode solver works in much the same way, using the electric component of the electromagnetic wave equation [144]

$$\left(\frac{c^2}{n^2} \nabla^2 - \frac{\partial^2}{\partial t^2} \right) \mathbf{E} = 0, \quad (4.2)$$

where c is the speed of light, and E is the electric field. Once again, this is translated into a weak form approximation and both electric field power and eigenvalues are calculated, this time corresponding to the effective refractive index of a particular electromagnetic mode.

With an electric mode profile accurately found, the various electrostriction components can be calculated as described in Chapter 3. Since for most systems both the pump and signal fields occupy the same mode, only one solution needs to be found in order to accurately apply these equations. Finally, equation A.39 can be applied for each of the three Brillouin gain components using the forces each one produces along with the electric and acoustic fields, to find gain values for each component.

4.2 Results

In the following section there is a large amount of variation in how modes are visually presented, here is a short guide on how to read these plots correctly. Material domains are represented with two colours, yellow and purple, representing areas of high and low refractive index respectively, meshes are simple line drawings that outline the elements within a structure, electromagnetic modes are shown with a yellow to purple colour gradient, with yellow areas representing high electric field strength and purple areas representing low electric field strength, and finally, acoustic modes are shown with a red to blue colour gradient, with red areas representing an overall positive displacement, blue areas representing an overall negative displacement, and white areas representing no displacement at all.

4.2.1 Diamond

As previously mentioned, PySBS is useful for simulating SBS dynamics specifically in waveguides, this is in contrast to the physical experiment presented in chapter 5 which does not take place in a waveguide, but in a bulk crystal. Thankfully, the simulation can be manipulated into presenting results that accurately model that experiment and useful

information can be gleaned as a result.

The elastic and electromagnetic mode solvers rely heavily on the geometry of the system in order to accurately find solutions, and so the geometry is set as a circle with the material parameters of diamond [145, 146] surrounded by air, this results in what is effectively a Gaussian beam profile within a bulk diamond and a beam width that is adjustable simply by changing the radius of the circle. An elastic mode is then chosen with wavevector and Brillouin shift that mimics the response that would occur in a bulk diamond. The domain, mesh, electric field mode, and acoustic field mode is presented in figure 4.1.

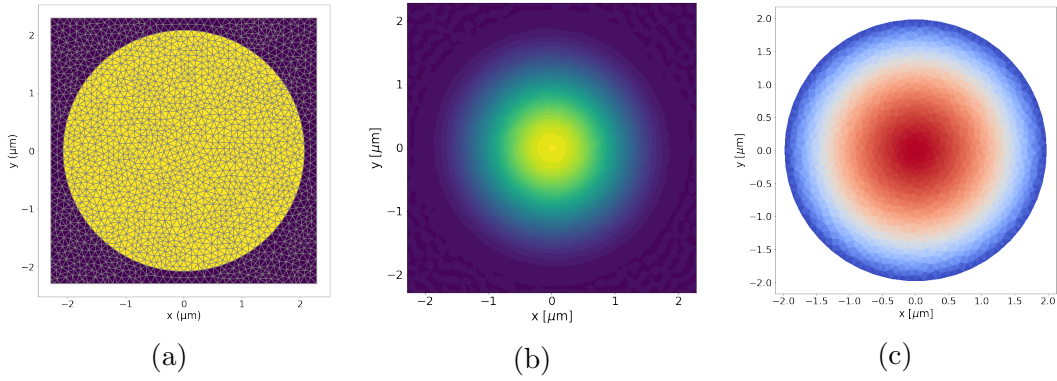


Figure 4.1: The various parameters used in the simulation of BSBS in diamond, featuring (a) the domain and the mesh, (b) the electric field mode, and (c) the acoustic field mode.

Although BSBS gain does have transverse components, the boundary electrostriction and radiation pressure components of BSBS gain can be ignored, as these effects are not present when focussing into the center of a bulk medium.

There are two lenses focussing light into the diamond to increase intensity leading to a higher Brillouin gain, the waist size determines the diameter of the circle use in the model and can be calculated using the equation [147]

$$w_0 = \frac{\lambda}{\pi \arctan(\frac{w_I}{f})}, \quad (4.3)$$

where λ is the wavelength, w_I is the initial beam diameter, and f is the focal length of

the lens. For a wavelength of 780nm, an initial beam diameter of 6mm, and a lens with a focal length of 25mm, the beam waist is $4\mu\text{m}$. There are several important figures that first must be calculated in order for the model to behave accurately, the first of which is Brillouin shift, which is present in equation A.39 and is therefore an important figure to know. Brillouin shift can be found analytically, using the equation [148]

$$\Omega_B = \frac{2vn\omega_p}{c}, \quad (4.4)$$

where v is the speed of sound in diamond, and ω_p is the angular frequency of the pump field. The second of these figures is the Brillouin linewidth, Bai *et al* [149] showed that the Brillouin linewidth at with a pump wavelength of 532nm is 12MHz. There is a frequency-squared law [150] relating wavelength and Brillouin linewidth, starting with

$$\left(\frac{\Omega_B}{\Omega_B^{ref}}\right)^2 = \frac{\Gamma}{\Gamma^{ref}}. \quad (4.5)$$

Substituting in equation 4.4, $\lambda = c/\omega$, and rearranging gives

$$\Gamma^{ref} \left(\frac{2vn/\lambda}{2v^{ref}n/\lambda^{ref}} \right) = \Gamma, \quad (4.6)$$

where Ω_B^{ref} , λ^{ref} , v^{ref} , and Γ^{ref} are the angular frequency, pump wavelength, speed of sound in diamond, and linewidth respectively, from Bai *et al* [149]¹. The speed of sound varies depending on the direction it travels through a crystal, three directions are chosen to be analysed representing cubic (100), dodecahedral (110), and eight sided octohedral (111) surface structures [151], these are the most common morphological structures and therefore represent a potential physical system well.

Figure 4.2b shows the Brillouin shift and gain of the [100], [110], and [111] directions in a single crystal diamond as described by the simulation parameters stated above. It is clear that there is both a significant gain and frequency shift difference between all three propagation directions caused by the variation in the speed of sound, those who

¹Finding this value was the primary goal of the first set of diamond experiments This paper was published in March 2020, after the majority of diamond experiments had been completed.

wish to probe Brillouin scattering in diamond must choose a direction to fit their own needs, however the increase in gain is a far more valuable addition and the small change in frequency shift can easily be accounted for. These values are comparatively similar to those seen in the literature [152].

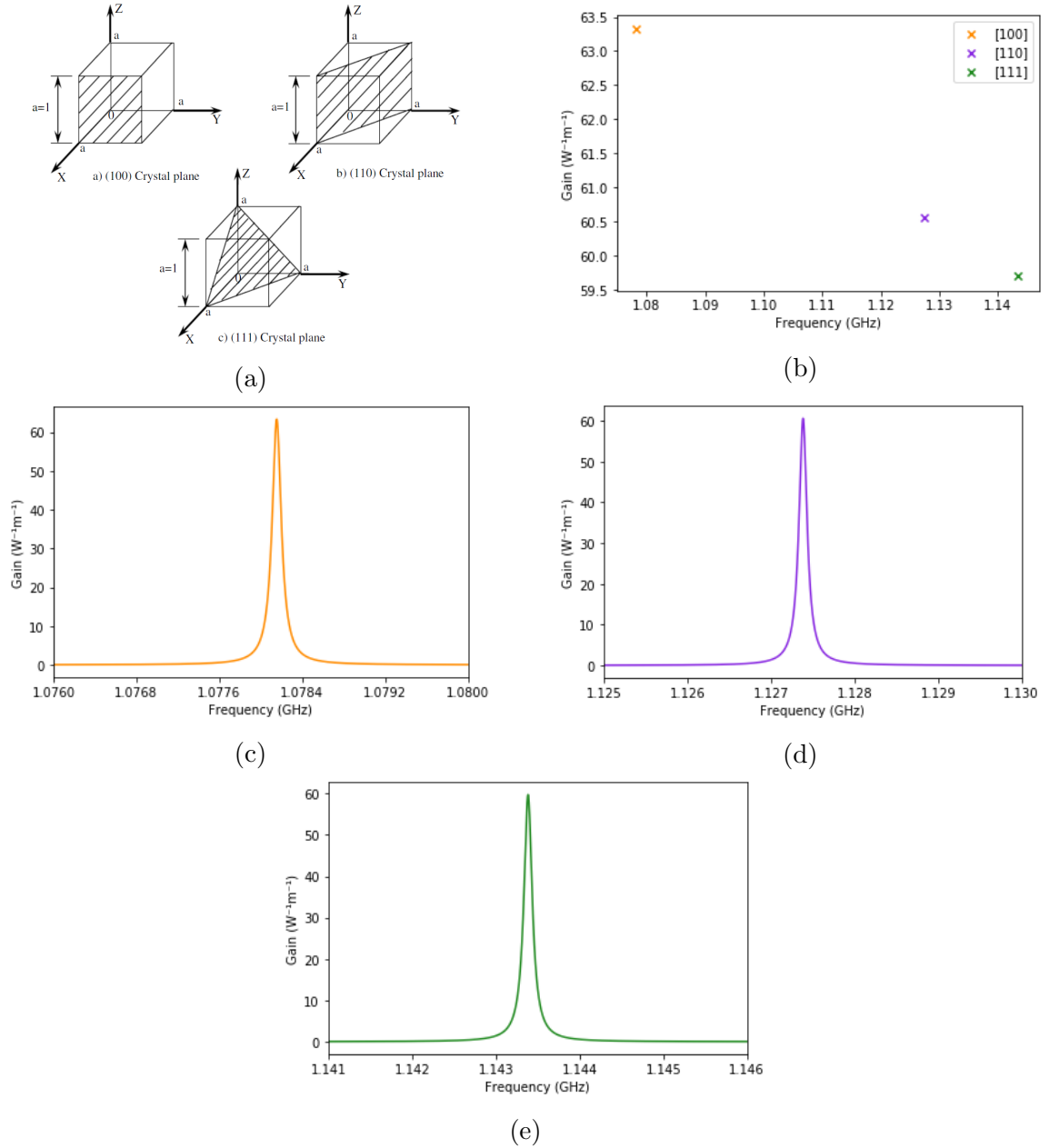


Figure 4.2: (a) A diagram of the (100), (110), and (111) planes of diamond, Reproduced from Taillandier *et al* [151]. (b) Gain frequency against Brillouin frequency for the [100], [110], and [111] directions. Brillouin gain profiles for the (c) [100], (d) [110], and (e) [111] crystal directions.

Table 4.1

Direction	$v(\text{ms}^{-1})$	$\Omega_B(\text{GHz})$	$\Gamma(\text{MHz})$	$g(\text{W}^{-1}\text{m}^{-1})$	$\tau(\text{ns})$
[100]	17520	108	10.6	63.3	93.7
[110]	18320	113	11.7	60.6	85.7
[111]	18580	114	12.0	59.7	83.3

From these values for gain and the linewidths found by equation 4.6, full gain profiles of each propagation direction can be , representing the results that would be present in the physical experiment. These are summarised in figure 4.2. The all important figure of phonon lifetime can be calculated using $\tau = 1/\Gamma$, this, along with all other direction dependent figures are summarised in table 4.1.

The units presented here, $\text{W}^{-1}\text{m}^{-1}$, describe the ratio of signal and control output powers at a peak power, w , with interaction length m . The acoustic phonon lifetimes generated here are not large when compared with other quantum memory protocols, but still provide a good amount of potential storage time and warrant further investigation. Using the values of gain produced by these simulations, it is possible to predict the distance at which full storage of an input signal pulse occurs. Boyd [148] presents an analytical solution to this problem that accounts for pump depletion effects

$$I_2(L) = \frac{I_1(0) [I_2(0)/I_1(0)] [1 - I_2(0)/I_1(0)]}{\exp \{gI_1(0)L [1 - I_2(0)/I_1(0)]\} - I_2(0)/I_1(0)}, \quad (4.7)$$

where I_1 and I_2 are the intensities of the pump and signal fields, L is the total length of the interaction medium, and z is the lateral distance along that length. Equation 4.8 is an analytical solution to the coupled equations describing the intensity evolution of pump and signal fields, however, this is not the case for the system presented in this thesis as it is concerned with Brillouin absorption and not gain. Small variations in the above equation changed the result to allow a more accurate description of Brillouin absorption

$$I_2(L) = \frac{I_1(0) [I_2(0)/I_1(0)] [1 + I_2(0)/I_1(0)]}{\exp \{gI_1(0)L [1 + I_2(0)/I_1(0)]\} + I_2(0)/I_1(0)}. \quad (4.8)$$

For an initial pump-signal intensity ratio of 5 and a diamond oriented along the [100]

direction, 99% of the signal field is scattered at a distance of 6.36cm as shown in figure 4.3. In 2020, Aiello *et al* [153] produced a CVD diamond wafer of radius 180mm and thickness 2mm, meaning the environment simulated and the overall quantum memory architecture presented here has genuine experimental prospects.

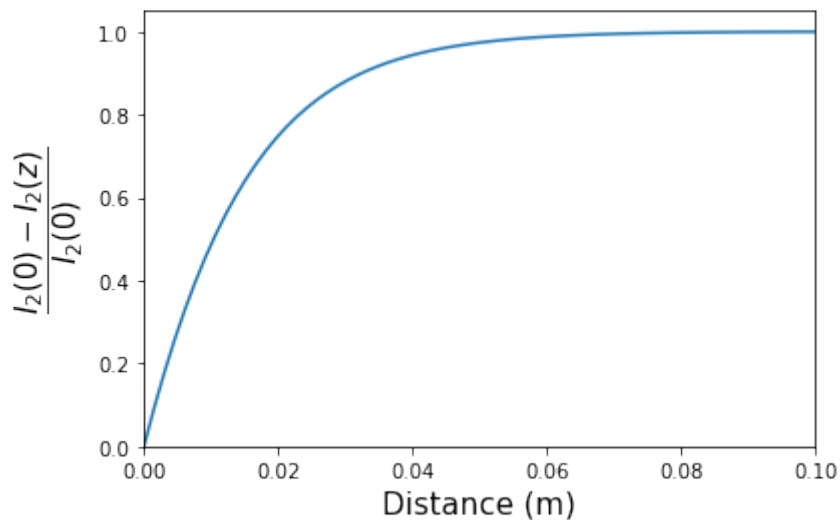


Figure 4.3: Portion of scattered signal field as a function of distance as described by equation 4.8. The signal field is depleted by 99% at a distance of 6.36cm.

Macroscopic crystals are hard to model and so corners were cut by adjusting simulation parameters in order to describe the desired effect and PySBS does not lend itself to deriving acoustic modes that are independent of material geometry as is the case with the diamond experiments, however the results produced here are in line with those found in the literature and allow for an analysis of how feasible this device is.

Chapter 5

Backward Brillouin Scattering in Diamond for use in Quantum Memories

In the following chapter a series of early experiments are presented with the goal of creating a diamond-based quantum memory that uses acoustic phonons accessed via stimulated Brillouin scattering as the storage mechanism. Although there are no explicit results given, the experiments show that a variety of preliminary experiments have been explored and that some of the more difficult technical problems have been overcome, paving the way for this research avenue to be explored further in the future.

5.1 Material Properties of Diamond

Diamond is an allotrope of carbon, each atom is bonded tetrahedrally to four nearest neighbours via sp^3 hybridised covalent bonds of length 1.51Å [156]. The resulting structure is a face-centred cubic lattice with a two-atom basis and 8 atoms in the unit cell, characterised by the space group $Fd\bar{3}m$ [157]. This structure is seen in other materials such as sphalerite, a form of zinc sulphide and is known as the zinc-blende structure [156]. The combination of element, structure, and bond type produces a material that holds extreme values of almost every measurable property, a list of these is presented in table

5.1 and a diagram of the structure of diamond is shown in figure 5.1.

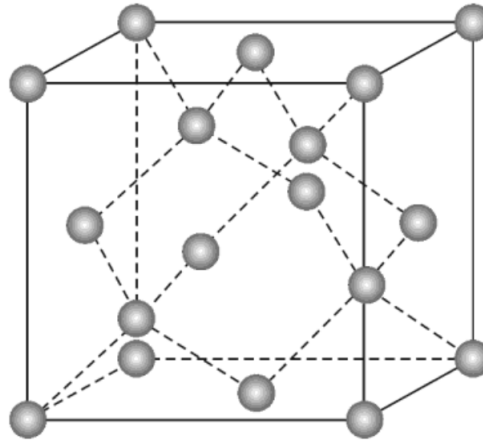


Figure 5.1: A single unit cell of diamond. Reproduced from [158].

5.1.1 Applications of Diamond

Hinted at already is the large number of useful properties that diamond possesses, they can be characterised into six different categories, electronic, photonic and quantum, mechanical, chemical, thermal, and optical. Diamond research has a rich history largely focussed around making use of these unique properties, presented here is a brief introduction into this research and some of the practical applications that have subsequently been developed.

Some of the properties come as a direct result of doping, adding to the crystal lattice with various other atoms and impurities gives rise to additional absorption lines in the medium and changes the electronic and optical properties, sometimes drastically. Dopants come in two forms depending on whether they act as an acceptor (P-type) or as a donor (N-type) of electrons. Both dopant types have been found for diamond but the primary N-type dopant s, phosphorus and nitrogen, have deep donor levels giving diamond a low conductivity, this eliminates its use in semiconductor computing [160]. Doping is achieved by introducing the doping material into the growth chamber, it then naturally occupies

Table 5.1: Principle Properties of Diamond [159].

Property	Value	Units
Hardness	1.0×10^4	kgmm^{-2}
Strength, tensile	> 1.2	GPa
Strength, compressive	> 110	GPa
Coefficient of friction (Dynamic)	0.03	Dimensionless
Density	3.52	gcm^{-3}
Young's modulus	1.22	GPa
Poisson's ratio	0.2	Dimensionless
Thermal expansion coefficient	1.1×10^{-6}	K^{-1}
Thermal conductivity	2000	$\text{Wm}^{-1}\text{K}^{-1}$
Thermal shock parameter	3.0×10^8	Wm^{-1}
Debye temperature	2200	K
Optical index of refraction (at 591nm)	2.41	Dimensionless
Optical transmissivity (from nm to far IR)	225	Dimensionless
Loss tangent at 40Hz	6.0×10^{-4}	Dimensionless
Dielectric constant	5.7	Dimensionless
Dielectric strength	1.0×10^7	Vcm^{-1}
Electron mobility	2200	$\text{cm}^2\text{V}^{-1}\text{s}^{-1}$
Hole mobility	1600	$\text{cm}^2\text{V}^{-1}\text{s}^{-1}$
Electron saturated velocity	2.7×10^7	cms^{-1}
Hole saturated velocity	1.0×10^7	cms^{-1}
Bandgap	5.45	eV
Resistivity	$10^{13} - 10^{16}$	Ωcm

carbon sites as the crystal grows¹.

- **Electronic** - When heavily doped with boron, diamond becomes electrically conductive due to the holes provided by the boron atoms. This in combination with diamonds chemical inertness makes heavily boron doped diamond a strong contender for electrodes in electrochemistry [161]. The importance of electrochemistry itself should not be understated, with applications in waste-water treatment [162], electroanalysis [163], synthesis of both organic [164] and inorganic [165] compounds, and biomolecule sensing [166]. Heavily boron doped diamond has also been shown to exhibit some superconductivity [167].

- **Photonic and Quantum** - When nitrogen is introduced into diamond and the material is heated up, vacancies (empty lattice sites) migrate and form stable defects with the nitrogen that take up two carbon sites, this is known as a Nitrogen-Vacancy (NV) defect. These defects have a long coherence time and can be initialised easily by pumping with green light [168], this allows for applications in quantum sensing and means the defect can be used as a qubit for quantum computing. NVs also have been shown to act as a single photon source [169], a quantum memory [170], and in 2015 Hensen *et al* [171] probed the principles of Bell's inequality using two entangled NV defects separated by 1.3km. Chen *et al* [172] have recently shown the possibility of writing NV defects straight into diamond using a laser annealing method on nitrogen doped diamond, this opens up huge opportunity for applications in quantum photonics by eliminating the defects spatial randomness when it is produced.

- **Mechanical** - The extreme hardness of diamond is perhaps the most publicly known property of diamond, defining the Mohs hardness scale [173] it is the hardest known natural material. This property is employed in the oil and natural gas mining industry, used specifically are polycrystalline diamond plugs [174] that provide the ideal trade-off between hardness and toughness², rather than the conventional percussive drilling, these

¹An interesting side effect of doping in diamond is that the colour of the crystal is able to be tuned when polished, different dopants produce different colours, nitrogen - yellow, boron - blue, nitrogen-vacancy centres - pink, and various others.

²Often confused with hardness, toughness is a similar material property that characterises the ability

diamond plugs use the more effective method of shear cutting the rocks, providing better cost/performance values for mining companies [175, 176].

This property is due to the strong, directional covalent bonds that make up diamond, as a result diamond has a large sound velocity, which directly contributes to Brillouin gain.

- **Chemical** - Nano-diamonds are nano-scale diamonds, they can be manufactured easily using contained explosions [177] and importantly for this section they are bio-inert, meaning they do not react with biological tissue. In addition, they are also capable of crossing the blood brain barrier, a mechanical barrier that prevents cells and molecules from entering the brain, the blood brain barrier has the unfortunate side effect of preventing drugs from crossing into the brain and represents the largest limiting factor for the progression of neurotherapeutics. By adsorbing drugs onto the surface of nano-diamonds, it has been shown that drugs can be effectively delivered beyond the blood brain barrier providing solutions to combat brain diseases such as Alzheimer's and Parkinson's [178, 179].

- **Thermal** - The strong and directional covalent bonds in diamond leads to some exceptional thermal properties, natural diamonds have been measured to have thermal conductivities of $2200 \text{ W m}^{-1} \text{ K}^{-1}$ [159] and isotopically pure single crystal diamond reaches values exceeding $40000 \text{ W m}^{-1} \text{ K}^{-1}$ at low temperatures [180], making it one of the best solids for thermal conductivity. This has applications in effective heat removal for high power electronics [181].

- **Optical** - Diamond has a high refractive index of 2.4 [159], the high contrast with air gives diamond the ability to strongly guide light when it is formed into waveguides [182], a somewhat useless but interesting side effect of this property is that the gemstone is sparkly when polished. Diamond also has a very strong Raman response at 1332 cm^{-1} [183] corresponding to the sp^3 bonds, making the characterisation of the material straightforward.

to absorb energy and plastically deform without fracturing.

5.1.2 Diamond-Based Quantum Memories

This would not be the first attempt at providing a functional quantum memory using diamond, so far attempts have been made that utilise bulk optical phonons accessed via Raman scattering, the nuclear spin of nitrogen in an NV defect, and the nuclear spin of silicon in an SiV⁻ defect [?, 67, 185].

England *et al* [67] have shown that light storage in diamond using optical phonons is not only possible, but can be used to store non-classical information. Trains of pump pulses separated by time τ interact with signal pulses to facilitate a resonant energy transfer between ground and storage states separated by 40THz (1332cm^{-1}), when resonance conditions are met the signal pulse is stored and retrieved with subsequent pulses. Results show that although the storage and retrieval of quantum information is possible, decoherence of the high frequency phonons results in a loss of information within 3ps, limiting the usefulness of this storage mechanism in quantum computing (see section 1.3.1 for more).

The spin of the nitrogen nucleus in an NV defect has been shown to provide an accurate storage mechanism that has a total storage fidelity of $88 \pm 6\%$ at a storage time of $10\mu\text{s}$, the nuclear spin of the nitrogen is used as the storage state and is manipulated using an external magnetic field [186]. Systems have been built with this in use, Bradley *et al* [184] have built a ten-qubit register combining the nuclear spin states of nine nearby carbon-13 atoms with an NV quantum memory entanglement is generated between all 45 possible qubit pairs, and the system can behave as a multiqubit memory, with a coherence time of 75s, the longest of any solid-state qubit.

The negatively charged Silicon-Vacancy (SiV⁻) defect has recently emerged as a competitor to the NV defect for its bright, narrowband transitions that exhibit small inhomogeneous broadening, and it has a coherence time that is protected by its inversion symmetry. It consists of a single silicon atom occupying the space caused by two vacancies. Spin-orbit coupling and crystal strain splits the ground level of the system, the lower band of which is split further by an external magnetic field and it is these energy levels that are

mapped to $|0\rangle$ and $|1\rangle$ states and are used as the storage states [185]. Coherence times of 13ms are achieved and fidelity reaches 89%.

5.2 Light Storage in Diamond via Stimulated Brillouin Scattering

In order to realise this proposal, a series of experiments must be performed to fully characterise the memory, the first of these is to measure the acoustic phonon lifetime in diamond which sets the limit to storage time of the memory.

Diamond is chosen as the storage medium for a variety of reasons, equation A.20 shows that the electrostriction tensor has a dependency on refractive index to the fourth power, therefore the large refractive index of diamond will result in a much higher Brillouin gain factor compared to other materials, increasing the likelihood of effective storage. The diamond used in these experiments is a mono-sectoral³ HPHT, single-crystal diamond manufactured by Element 6 that has been polished on the $[100]$ faces and has been engineered to reduce impurities and crystal imperfections that act as phonon scattering centres, by creating a crystal that is near-perfect the phonons lifetimes are extended, which leads to a greater memory storage time. The large Brillouin frequency (108GHz, as shown in chapter 4) adds to the utility of using diamond in this experiment, as it results in a sparsely populated phonon band at room temperature reducing noise in the system. The sample along with 3D printed sample mount is shown in figure 5.2

³Cut from the same growth sector.

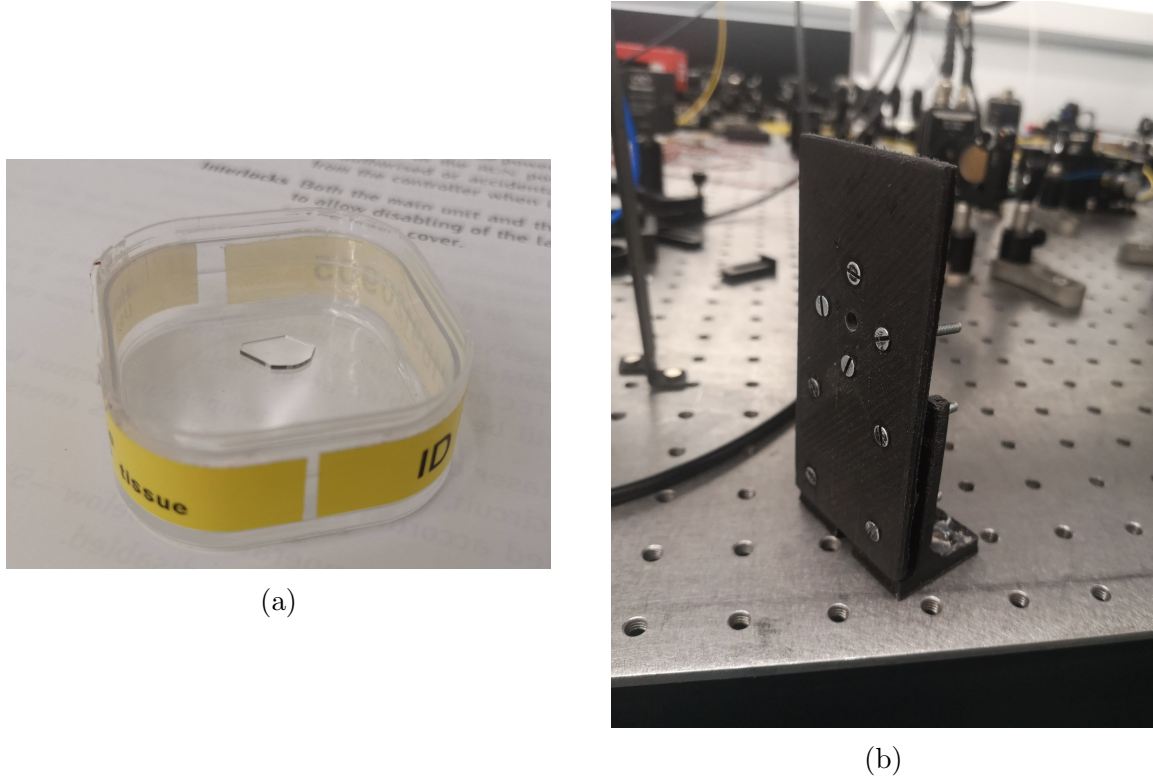


Figure 5.2: (a) The diamond sample used in the experiments presented in this chapter, and (b) the 3D printed mount that was used to hold it in place.

Pump and signal beams detuned by the Brillouin shift are set to counterpropagate through the diamond sample, the signal beam is swept through a range of frequencies and measured to produce a full gain spectrum as a function of detuning. The full-width half-maximum (FWHM) of the Brillouin gain peak can then be extracted, the inverse of which is the phonon lifetime, as per the equation $\tau_P = \Gamma_m^{-1}$. Beams are continuous wave to provide a constant SBS signal and to provide a spectrum, experiments take place at 780nm to align with the rubidium experiments shown in chapter 2 and to increase Brillouin gain.

There are two options for how to generate the Brillouin response corresponding to Stokes and anti-Stokes scattering, both processes produce the desired effect but at different intensities. It is Stokes scattering that is primarily investigated, as the dynamics of the interaction closely resemble that of information storage.

Two separate attempts were made at generating this 108GHz shift, using a single laser

with a 108GHz modulation and using two separate lasers. Both options have their *pros* and *cons*, the former adds stability to the system as when the laser inevitably drifts due to local temperature fluctuations both signal and pump beams would drift by the same amount leaving the detuning unaffected and the latter has a much simpler physical implementation. Unfortunately, both attempts ended with null results.

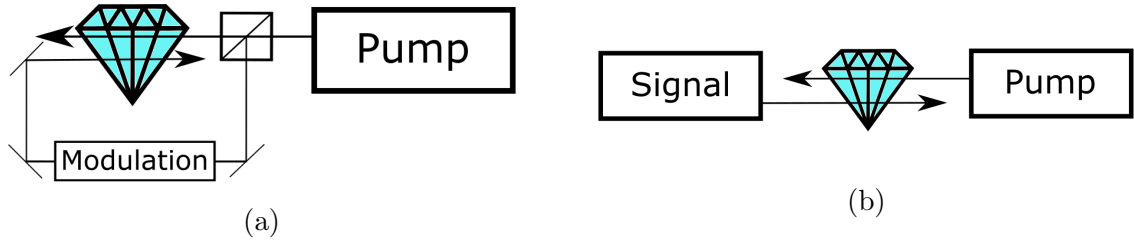


Figure 5.3: Two different methods used to achieve the necessary 108GHz frequency shift between pump and signal beams, using (a) a single laser with a modulator and (b) two separate lasers.

5.2.1 Detuning With an Electro-optic Modulator

In order to generate a 108GHz sideband the beam (produced by a MOGLabs tuneable cat-eye laser) is passed through an electro-optic modulator (EOM), these devices come in a variety of types that modulate phase, frequency, amplitude, or polarisation.

An oscillating electric field will induce a birefringence in a non-centrosymmetric crystal such as lithium niobate as it passes through the crystal, any subsequent light passing through the device will then experience a phase shift between orthogonal polarisations, resulting in sidebands with intensities proportional to the applied electric field and frequency shifts at integer multiples of the applied frequency. This is the basic function of a phase modulating EOM and is the kind that is used in this experiment. By including other optical instruments such as waveplates and polarisers, the various EOM types can be converted between one another.

The NIR-MPX800-LN-20 electro optic phase modulator produced by iXblue receives drive frequencies of up to 22GHz, the desired frequency shift is then possible using the fifth

sideband. The intensities of the various sidebands follow a Bessel function as applied voltage (and therefore phase shift) increases, at a phase shift of 6.4rad the fifth sideband is the most prominent, however some further filtering must be done to remove the fundamental along with sidebands one to four in order to reduce noise in the system. Figure 5.4 shows the fundamental along with the first 5 sidebands as a function of phase delay, the vertical line shows the amplitudes of the various sidebands at the desired phase shift.

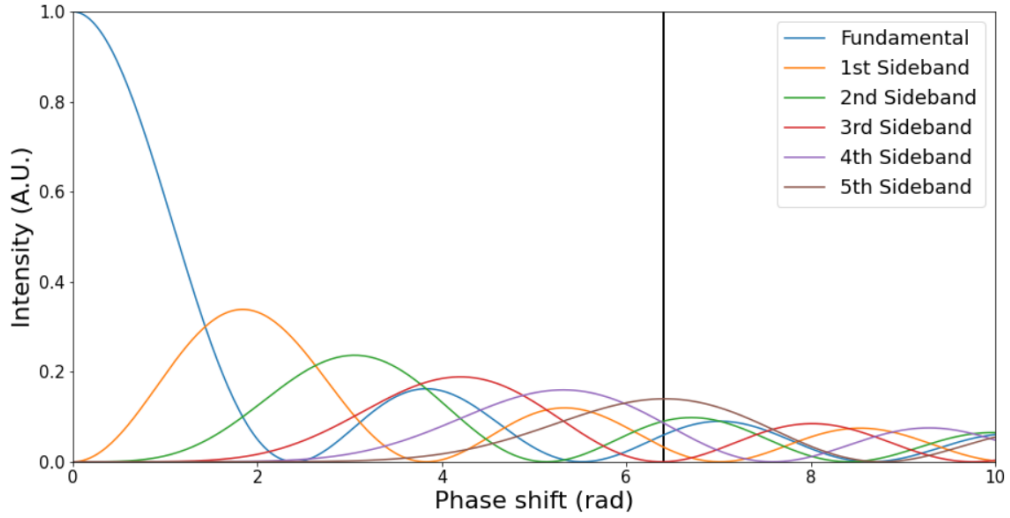


Figure 5.4: The first six bessel functions representing the fundamental and first 5 sidebands produced by and electro-optic phase modulator. The first maximum of the desired fifth sideband resides at a phase shift of 6.4rad.

There are a number of ways to spatially distinguish between different wavelengths such as reflective diffraction gratings, unfortunately for these applications the wavelength change is too fine for any of the traditional methods to effectively and efficiently separate the sidebands. Instead, two etalons with varying free spectral ranges are used, they have transmission windows that overlap only once within the 108GHz range and so with some fine tuning it is possible to only extract the desired sideband. Etalons consist of two planar partially reflective mirrors creating a cavity, only certain resonance modes are supported by this cavity and therefore only certain wavelengths can pass through. The various properties of the device, such as reflectivity of the mirrors and mirror spacing affect how frequently resonance conditions are met, this is known as the free-spectral range.

The two etalons used here both have mirrors with reflectivities of 80% and the cavity

is filled with fused silica, they have separation distances of 6.35mm and 10mm resulting in free spectral ranges of 16.08GHz and 10.21GHz respectively. Although this will not limit light from other sidebands entirely, the degree to which non-useful light is reduced is enough to see minimal disturbance in the experiment.

Signal and probe beams need to be connected and separated to stimulate the process and to allow for accurate detection, both beams occupy orthogonal linear polarisation states that enter and exit from separate arms on two polarising beam splitters on either side of the diamond sample. The overlap integral of the electric field components of two orthogonal linearly polarised beams is zero, placing quarter-wave plates on either side of the diamond converts these beams into orthogonal circular polarisations allowing them to interact before converting them back into linear polarisations so that they can once again be separated on a polarising beam splitter. The Brillouin interaction between orthogonal circular polarisations is 50% as intense as the Brillouin interaction between beams with identical polarisation states [187], however the reduction in the pump field leaking into that mode increases the SNR despite this loss in scattering efficiency.

An 818-bb-21 high speed (1.2GHz) photo detector produced by Newport optics is used to detect the signal beam, this was chosen as an economic solution that was used for multiple experiments that make use of the large bandwidth. The Brillouin interaction is expected to be very small relative to the intensity of the probe beam and so lock-in detection is used to boost sensitivity of the measurement.

A custom driver for the EOM was built that allowed the applied frequency (and therefore the frequency of the sideband) to be linearly swept, contributing the final piece of the experiment. A full diagram of the above experiment is shown in figure 5.5.

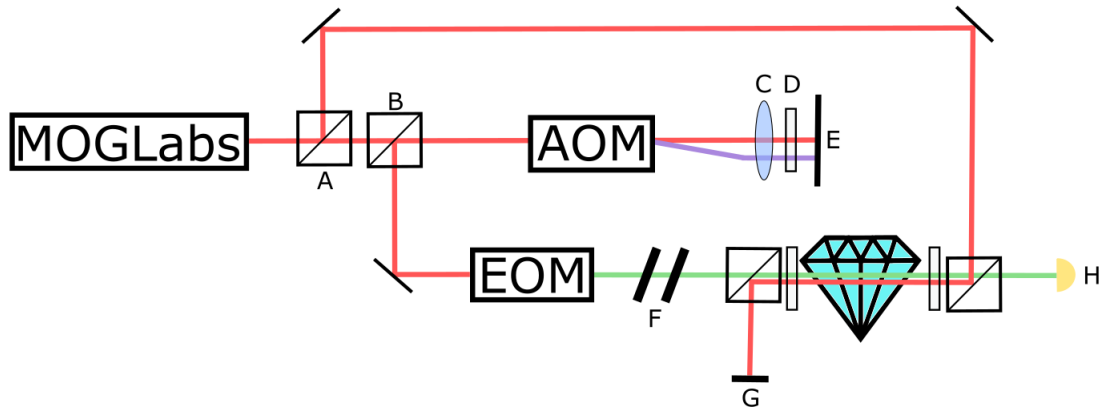


Figure 5.5: A full schematic of the diamond BSBS experiment featuring a single laser and a modulation technique. Light is first split into signal and pump beams (A), the signal field passes through an AOM making use of a collimating lens (C), quarter-wave plate (D), planar mirror (E), and a polarising beam splitter (B) to gain a frequency sideband used for lock-in detection, it then passes through an EOM to gain five sidebands at 21.6GHz intervals, filtering of the fundamental and first four sidebands is done using a series of etalons (F), and finally the light passes through the diamond to interact with the pump field and undergo the BSBS process before the signal beam is detected (H) and excess light from the pump beam is discarded (G).

The individual components of this experiment all worked in isolation, however bringing them together to form a functioning system proved incredibly difficult. Optical power loss was the primary issue, there is a significant drop in power as light passes through each component due to the intrinsic losses associated with performing these operations, which in combination with the delicate alignment of the etalon system produced a modulated beam with an optical power far below the capabilities of the detector.

Each component had an effect on the power of the beam, the AOM reduced the power by 30%, the EOM reduced power by 40%, the etalons reduced power by 60%, a further 25% was lost due to imperfect polarisation controlled beam splitting, 17% due to the reflections off the diamond crystal, and 50% due to the necessary polarisation system within the crystal. This results in a total reduction of 95% of laser power not considering the initial splitting of beams nor the reduction that comes as a result of sharing the laser with other experiments. For a initial power of 2mW, the power at the detector would be 0.1mW which will produce a signal of 2mV with the detector used and is a value below the noise

floor of the Moku Oscilloscope. All percentages presented here are approximate.

Even with a functioning lock-in system, these powers are too low to reliably detect a scattering signal, in addition, alignment of etalons was imprecise and was frequently subject to drift requiring near constant monitoring and adjustment adding to the difficulty of executing this experiment. A tapered amplifier could have been used to amplify the weak signal beam, but even without considering the financial detriment that would have, a tapered amplifier would introduce noise to the signal beam that would significantly effect the Brillouin interaction. Even with these negative effects, however, the inclusion of a tapered amplifier in this experiment could be necessary as without it no response can be measured.

To conclude, although the premise for this experiment was well thought out, the physical implementation requiring the cooperation of multiple different complex systems and the engineering challenges associated with it were too great to overcome. Rather than continuing the fruitless attempts at solving some of these issues, the simpler setup involving separate lasers was explored.

5.2.2 Detuning With Two Lasers

By including a second laser in this experiment, all of the problems associated with the modulation can be eliminated. In place, problems surrounding stability arise, as the detuning between pump and signal beams can now drift away from each other.

A second tuneable cateye laser manufactured by MOGLabs was used to replace the various instruments that allowed for the modulation of the pump beam, the main sources of optical power loss (the EOM and the etalons) were subsequently removed from the experiment. The double pass AOM configuration remained in place as it was still in use as a carrier frequency for lock-in detection. The polarisation control as light enters the diamond was also kept from the previous experiment, the increase in power is large enough such that the 50% reduction in Brillouin gain is off set. A full schematic of this experiment is shown in figure 5.6.

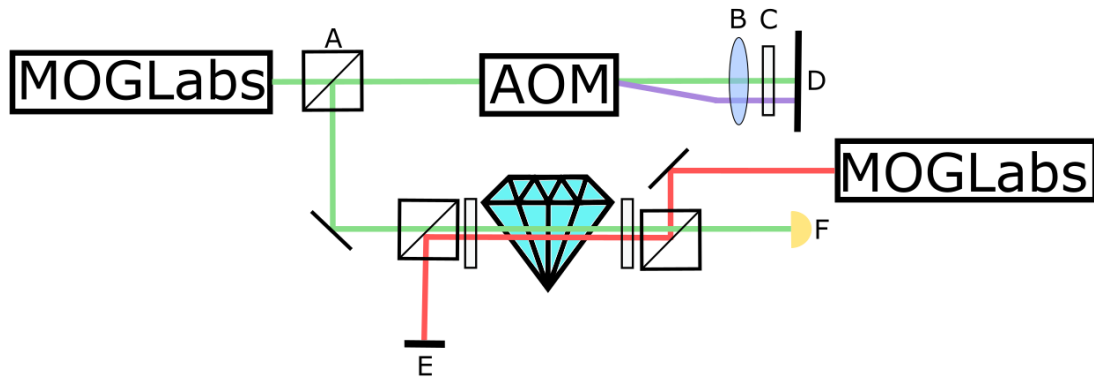


Figure 5.6: A full schematic of the diamond BSBS experiment featuring two separate lasers. The signal beam passes through an AOM making use of a collimating lens (B), a quarter-wave plate (C), a planar mirror (D), and a polarising beam splitter (A) to gain a frequency sideband used for lock in detection. The pump and signal beams are then incident on the diamond sample where BSBS takes place, the signal beam is detected (F) and excess light from the pump field is discarded (E).

By applying a sawtooth-shaped current variation to the piezoelectric actuator in the laser, the wavelength of the laser can also be made to follow a sawtooth pattern, this is achieved by the laser controller. Sweeps of 5GHz can be achieved in this way, care must be taken when initialising this sweep as mode-hops are frequent and easily disturb the otherwise clean sweep. MOGLabs claim sub-MHz stability, however the more complicated nature of using these devices in a research environment shows that this is not always the case even in temperature and humidity controlled environments.

Despite these changes, a Brillouin response was unable to be detected, once again due to a loss of optical power. Mentioned frequently throughout this report, the setup used had to be designed in a way such that tools could be shared between diamond and rubidium experiments, this includes the second laser and means that light had to be passed through a fibre patch cable before becoming available for use in the experiment, instantly resulting in a 20 – 30% drop in optical power. There was also issue with the sample itself, although diamonds high refractive index has a large influence on Brillouin gain, it also has the undesirable effect of reflecting 17% of the light that is incident on the material, this is a problem that also affected the previous experiment but was unnoticeable with such low

light levels. Including the power reductions mentioned in the previous section that also apply here, this resulted in an overall power reduction of 70% which on a beam of 2mW will mean the power at detection is 0.6mW producing an electrical signal of 1.2mV. Once again this is below the noise floor of the Moku oscilloscope.

These issues combined meant that the predicted Brillouin gain fell beneath the noise floor of the detector. A solution to this issue exists in the form of a more sensitive detector, however the implementation of this was unable to be completed.

Towards the end of this project, a Spectra-Physics Tsunami Ultrafast Titanium-Sapphire laser became available for use in this experiment as a replacement for the pump beam, the laser produces pulses at a repetition rate of 80MHz, with a (somewhat) tunable duration ranging from 10ps to 50ps, and has a tunable wavelength. This laser is capable of producing pulses with a peak power of 375W, this will comfortably generate acoustic phonons in the material and will make detecting them significantly easier in comparison to the previous setup. The pump beam produced by the Ti:Sapph was set to propagate through the diamond sample, detection of a signal beam was done using the same polarisation set up as before that results in orthogonal circular polarisations between pump and signal beams in the diamond, the frequency of the signal beam was swept through the expected Brillouin frequency and the output was measured.

Heavy time restraints meant that this experiment was rushed and once again ended before any results could be seen, the source of issue is varied. One of the benefits of the MOGLabs lasers is that the linewidth of the laser is expected to be small in comparison to the Brillouin gain linewidth allowing for high resolution probing of the Brillouin gain linewidth. The Tsunami, however, produces short pulses with high spectral bandwidths, any Brillouin response seen here is therefore more ambiguous as it is unclear how the low linewidth signal beam interacts with the pump beam. This generates noise in the system and adds the need for post-processing techniques to accurately extract the Brillouin gain linewidth.

In order for Brillouin scattering to occur as efficiently as possible there must be a high spatial mode overlap between pump and probe beams, in previous experiments this problem had been solved with the use of fibre, if both beams enter and exit from fibre on either side of the diamond, it is ensured that they will remain in the same spatial mode as they propagate through the material, however due to these time constraints this technique was omitted in favour of using a series of irises to align the two beams, which may explain why a signal was not able to be detected.

The Ti:Sapph laser allowed light with up to 300mW of average power to be used, optical filters could not be used as they would cut the signal beam out of the experiment that sat only 100GHz away and so relied upon was filtering using a series of waveplates and polarising beam splitters. High extinction ratios can be achieved using this method but even at lower powers some light leaked through into the detection scheme, making analysing the output of the signal beam difficult. Other filtering techniques such as etalons, diffraction gratings, and virtually imaged phase arrays were considered but either did not perform well enough or required space that was unavailable. Upgrading to a more sensitive detector in an attempt to locate a smaller Brillouin response meant this problem was made worse, the leaking pump field saturated the detector with ease.

5.3 Further Work

In the time since these experiments took place, the phonon lifetime in diamond has been established in the literature [149] with a value of 12MHz at a wavelength of 532nm, however it is still useful to find here as it will be different for the diamond used in these experiments and is necessary to characterise the quantum memory ready for when it is in operation. In addition, the value presented was at a fixed wavelength of 532nm [149] and so far there is no experimental analysis of how the Brillouin gain linewidth changes with operation wavelength.

When that experiment has been completed, work will begin in the way outlined in chapter 1. First, a cavity will be built around the diamond that incorporates mirrored lenses fabricated into the sample which results in a low volume cavity and high resonant bandwidths, this allows for both pump and signal fields to be resonant with the cavity and for the propagation of short pulses. A sample featuring mirrored lenses has already been fabricated (figure 5.7), however experiments on this sample are yet to take place.

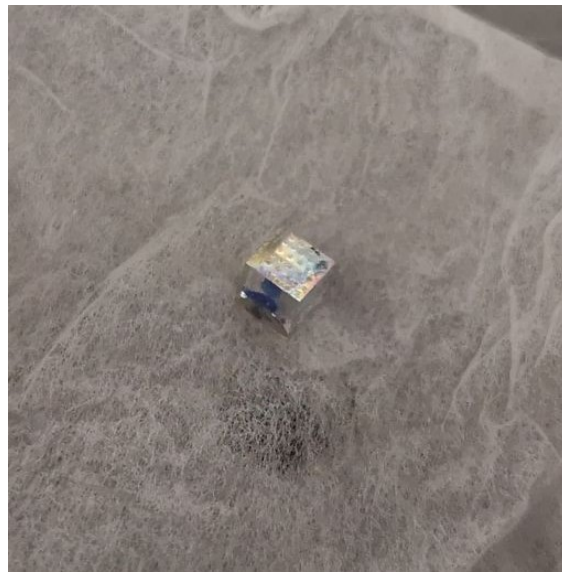


Figure 5.7: The second diamond sample available, this sample features an array of micro-lenses fabricated onto the surface that will act as part of the ring cavity planned for later experiments. This sample was fabricated by Dr. Erdan Gu at Strathclyde University.

Pulses can then be used to simulate the storage and retrieval of quantum information, before the move is made to single photons. Doing so will help further characterise the memory and gain values such as readout efficiency and fidelity.

Chapter 6

A Finite-Element Analysis of Brillouin Scattering: Fibre Tapers

The following set of simulations exhibit forward Brillouin scattering in optical fibre tapers using the same method described in chapter four, both intra and intermodal scattering is analysed to simulate the experiments that have taken place in the lab as well as the planned experiments that work towards a functioning photonic switch.

As was the case in previous simulations, acoustic modes in a taper can be found by calculating eigenmodes for the constitutive equation of motion for an elastic medium with appropriate boundary conditions

$$\nabla \cdot \sigma = \rho \frac{\partial^2 \mathbf{u}}{\partial t^2}, \quad (6.1)$$

where σ is stress, ρ is density, \mathbf{u} is the displacement vector, and t is time. These solutions are assigned azimuthal and radial mode numbers, n and m , and are classified according to the character of their motion as torsional, radial, longitudinal, flexural, or mixtures of these motions. Recall from Chapter 3 that for FSBS, $q = 0$, and so only acoustic modes with zero wavevector are Brillouin active, these are the R_{0m} and TR_{2m} acoustic modes, corresponding to radial and mixed torsional radial motions [188]. The frequency of these modes is gained by applying the free-surface boundary condition to a cylindrical rod and

is represented by the equation

$$f(GHz) = \frac{y_1 v_t}{\pi d(\mu m)} = \frac{p_m}{d}, \quad (6.2)$$

where y_1 is the first root of the transcendental equation representing the free-surface boundary condition, v_t is the acoustic velocity in silica, d is the diameter, and $p_m = y_1 v_t / \pi$ is a constant that is particular to a certain mode. For the R_{01} and TR_{01} modes, p_m is equal to $3.82GHz\mu m^{-1}$ and $2.79GHz\mu m^{-1}$ respectively.

The simulation geometry consists of a circle with the material properties of silica glass from [189–191] surrounded by air, and a diameter of $2.5\mu m$ to match that of the experiment this simulation is attempting to recreate. Applying these conditions to the acoustic mode solver provides accurate results that can be used in simulations. The electromagnetic mode solver requires no alterations and can consistently provide accurate results. Contributions to Brillouin gain from FSBS are purely transverse, and so only boundary electrostriction and radiation pressure is considered for these simulations, these two forces act in opposite directions on the taper and so partly cancel each other out, this is taken into account when calculating overall gain values.

The X, Y, and Z components of each acoustic mode can be viewed individually to confirm the calculated eigenmodes are correct. Figure 6.1 shows the X, Y, and Z components of the R_{01} and TR_{01} modes found by the mode solver, it is easy to recognise radial modes due to the consistent displacement acting away from the centre of the fibre, and torsional radial components show displacements acting at a tangent to the fibre-air interface. Both of these modes have little or sparse displacement in the Z direction, meaning these modes are purely transverse.

Due to limitations in computational power, the mesh density in the following simulations was not able to be increased to an appropriate level which led to fluctuations in results for fibres of near identical diameter. In an attempt to mitigate these errors as much as possible, simulations are ran for a diameter of $\pm 10^{-4}\mu m$ surrounding the target diameter

and an error presented. Although this does not provide full detail of the simulations, it allows for further analysis to take place and represents the most accurate solutions under these conditions.

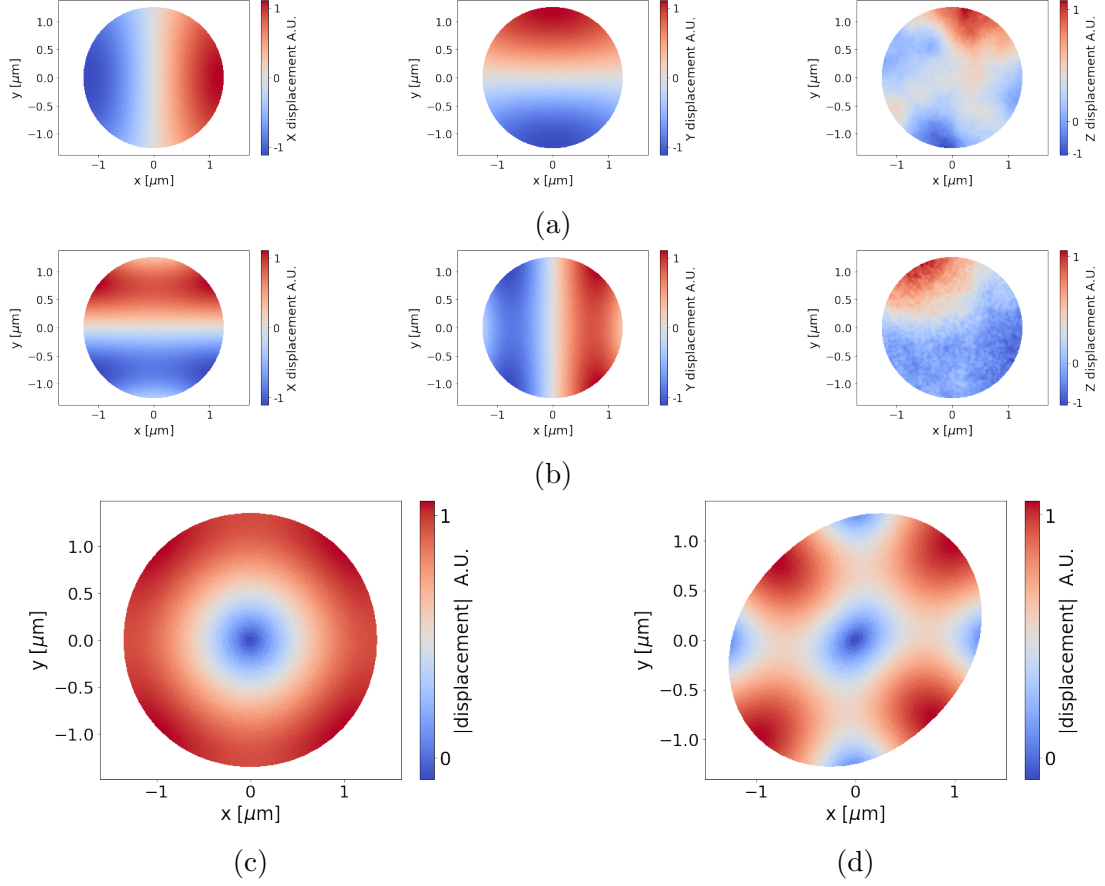


Figure 6.1: Figures (a) and (b) show the X, Y, and Z components of the R_{01} (c) and TR_{21} (d) acoustic modes respectively. From these, an analysis of overall displacement directions can be done to confirm the accuracy of these modes. Physical displacement is exaggerated to aid understanding of the forces a system is under, this is especially true in (d).

6.1 Intramodal FSBS

Beginning with intramodal FSBS, a fixed taper diameter of $2.5\mu\text{m}$ is used and pump wavelength is kept at 780nm . Figure 6.2 shows the domain, the mesh, and the electromagnetic mode, and figure 6.1 shows the R_{01} and TR_{01} acoustic modes which were used in these simulations. The fundamental electromagnetic mode is used for both the pump and signal beams. Brillouin gain for the R_{01} acoustic mode is $4.37 \times 10^{-4} \pm 6.32 \times 10^{-8} \text{W}^{-1}\text{m}^{-1}$ due

to electrostrictive forces, and $5.29 \times 10^{-4} \pm 6.91 \times 10^{-7} \text{W}^{-1}\text{m}^{-1}$ due to radiation pressure forces, resulting in an overall gain of $9.20 \times 10^{-5} \pm 6.93 \times 10^{-7} \text{W}^{-1}\text{m}^{-1}$. Brillouin gain for the TR_{01} acoustic mode is $3.72 \times 10^{-8} \pm 1.01 \times 10^{-8} \text{W}^{-1}\text{m}^{-1}$ due to electrostrictive forces, and $9.51 \times 10^{-5} \pm 2.08 \times 10^{-5} \text{W}^{-1}\text{m}^{-1}$ due to radiation pressure forces, resulting in an overall gain of $9.51 \times 10^{-5} \pm 2.08 \times 10^{-5} \text{W}^{-1}\text{m}^{-1}$. Brillouin gain is significantly higher for the R_{01} acoustic mode compared to the TR_{01} acoustic mode, this is in line with experimental results presented in the literature [192, 193].

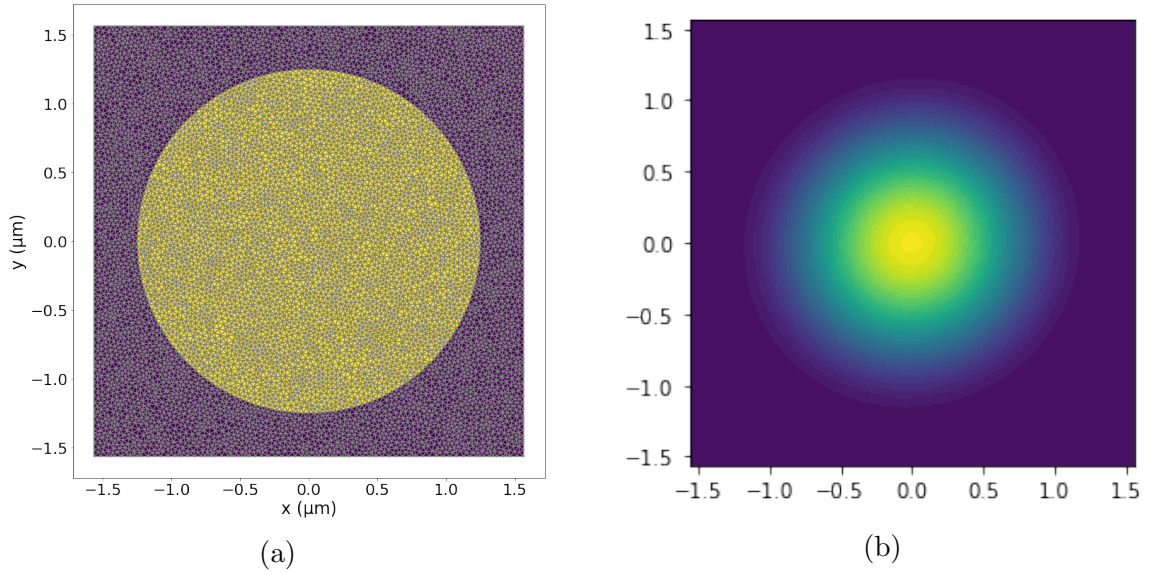
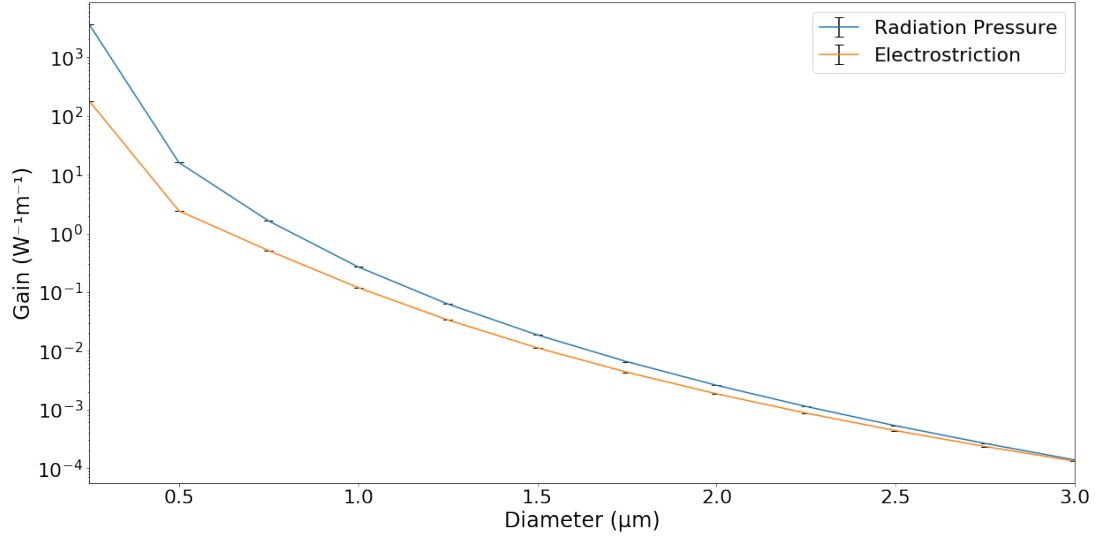


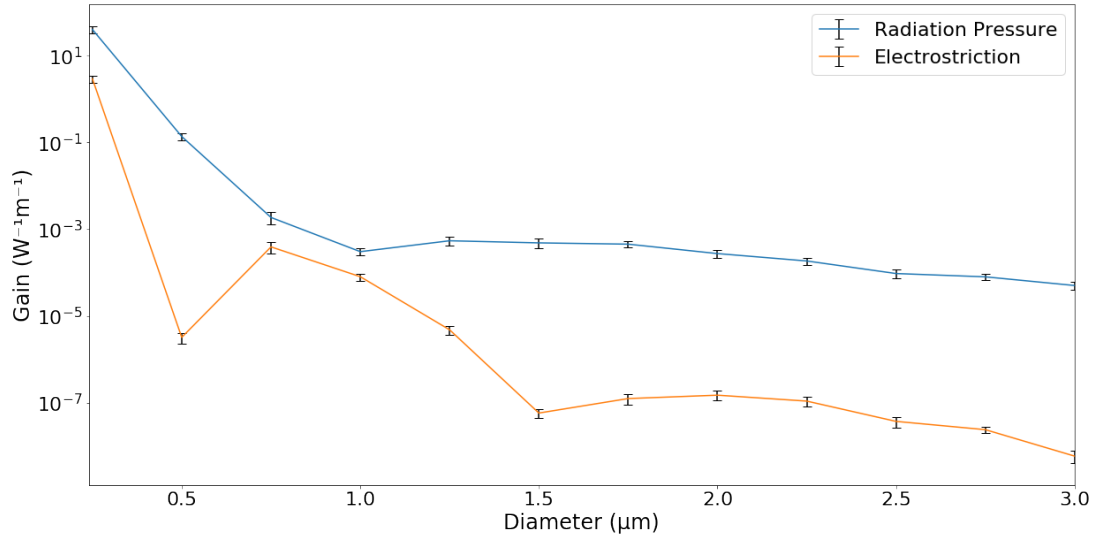
Figure 6.2: The (a) domain, mesh, and (b) electric field mode used in intramodal FSBS simulations.

Diameter can be swept while maintaining mode structures, giving insight into how gain varies as diameter changes. Figure 6.3 shows how gain for both boundary electrostriction and radiation pressure components varies as the diameter increases from $0.125\mu\text{m}$ to $3\mu\text{m}$. The graphs begin at a diameter of $0.125\mu\text{m}$ as this is the cut-off beyond which the fundamental electromagnetic mode does not propagate. Overall gain is maximum at $0.125\mu\text{m}$ with a gain of $3.46 \times 10^3 \pm 22.7 \text{W}^{-1}\text{m}^{-1}$ for the R_{01} acoustic mode, and $0.125\mu\text{m}$ with a gain of $37.2 \pm 7.66 \text{W}^{-1}\text{m}^{-1}$ for the TR_{21} acoustic mode, gain caused by both acoustic modes decreases by 7 orders of magnitude before reaching the end of the simulation. This dramatic decrease in gain is due to the cross sectional area of the taper increasing, the power of a beam is therefore distributed more evenly across a mode which has a large effect on the

non-linear nature of electrostriction and specifically the interactions occurring at the fibre boundaries. It is believed that the dip at $0.5\mu\text{m}$ is an artefact of low computational power.



(a)



(b)

Figure 6.3: Graphs indicating how the boundary electrostriction and radiation pressure components of intramodal FSBS gain vary as diameter is increased from $0.25\mu\text{m}$ to $3\mu\text{m}$ for (a) R_{01} and (b) TR_{21} acoustic modes

6.2 Intermodal FSBS

Next, intermodal FSBS is analysed using the same domain, mesh, and acoustic modes shown in figure 6.2, but changing the electromagnetic modes for the pump and signal beams to those corresponding to the fundamental (LP_{01}) and first order (LP_{11}) modes of the fibre, as shown in figure 6.4. Brillouin gain for the R_{01} acoustic mode is $6.52 \times 10^{-11} \pm 2.05 \times 10^{-11} \text{W}^{-1}\text{m}^{-1}$ due to electrostrictive forces, and $1.96 \times 10^{-9} \pm 4.90 \times 10^{-10} \text{W}^{-1}\text{m}^{-1}$ due to radiation pressure forces, resulting in an overall gain of $1.90 \times 10^{-9} \pm 4.90 \times 10^{-10} \text{W}^{-1}\text{m}^{-1}$. Brillouin gain for the TR_{21} acoustic mode is $2.73 \times 10^{-11} \pm 8.95 \times 10^{-12} \text{W}^{-1}\text{m}^{-1}$ due to electrostrictive forces, and $2.013 \times 10^{-9} \pm 6.76 \times 10^{-10} \text{W}^{-1}\text{m}^{-1}$ due to radiation pressure forces, resulting in an overall gain of $1.96 \times 10^{-9} \pm 6.76 \times 10^{-10} \text{W}^{-1}\text{m}^{-1}$. These values are considerably lower than that of intramodal FSBS and expectedly so, due to the low overlap between LP_{01} and LP_{11} electromagnetic modes.

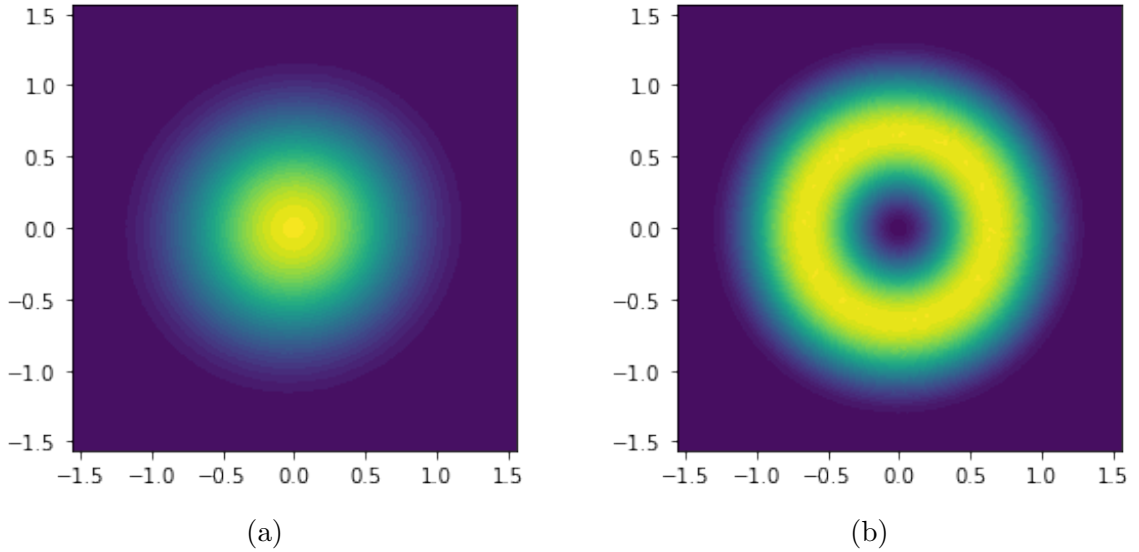


Figure 6.4: (a) Fundamental (LP_{01}) and (b) First order (LP_{11}) electromagnetic modes of a fibre taper with a diameter of $2.5\mu\text{m}$.

This again can undergo a diameter sweep, the results of which are presented in figure 6.5. Once again, the results from this series of simulations are just as expected, intermodal FSBS has consistently lower gain than intramodal FSBS due to the smaller overlap between the two electromagnetic modes. Overall gain peaks at $0.5\mu\text{m}$ with a

value of $1.16 \times 10^{-6} \pm 5.19 \times 10^{-7} \text{W}^{-1}\text{m}^{-1}$ for the R_{01} mode, and $0.5\mu\text{m}$ with a value of $7.50 \times 10^{-7} \pm 2.38 \times 10^{-7} \text{W}^{-1}\text{m}^{-1}$ for the TR_{21} mode. Even though the individual gain components in intermodal FSBS are much lower compared to that of intramodal FSBS, the relative difference between boundary electrostriction and radiation pressure is much higher and therefore don't counteract each other as much as in intramodal FSBS.

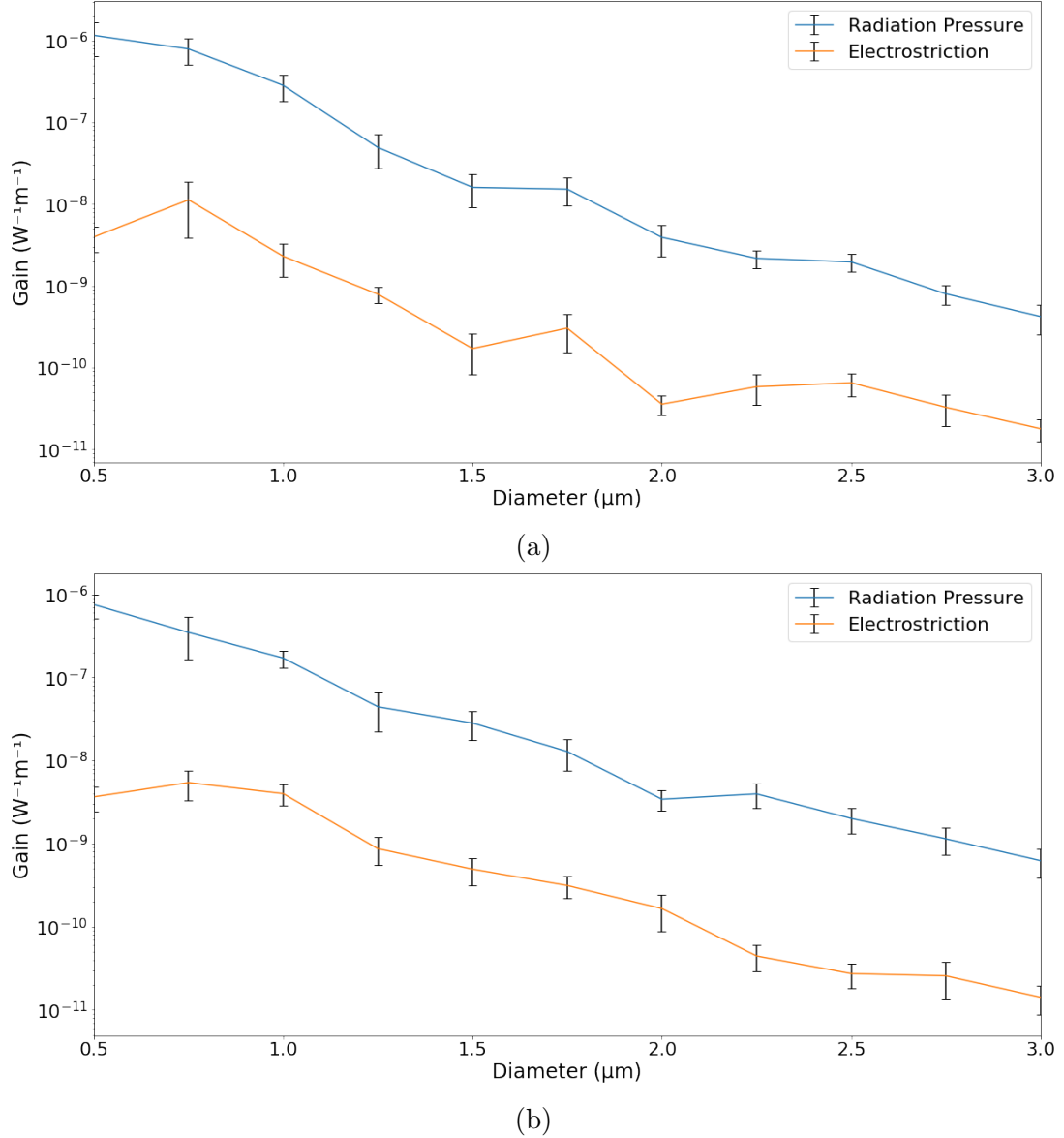


Figure 6.5: The boundary electrostriction and radiation pressure components of intermodal FSBS gain vary as diameter is increased from $0.25\mu\text{m}$ to $2.0\mu\text{m}$ for (a) R_{01} and (b) TR_{21} acoustic modes.

The first order mode begins guiding light at a taper diameter of $0.5\mu\text{m}$, hence the data

for the case of intermodal scattering begins slightly later than previously.

Frequency must be taken into account when analysing these results for use in experiments, equation 6.2 shows that at smaller diameters the frequency of the R_{01} mode exceeds 15GHz, and so there is a stark trade off between high Brillouin gain and low frequencies that are much easier to measure physically. This issue is less important as a direct measurement of Brillouin frequency is not important for the final devices operation.

These results, like all theoretical work, are to be taken lightly. This model assumes that the tapers have a circular cross section which isn't always true especially for a null coupling fibre taper, which depending on fabrication parameters could be oval in shape, this would result in the two degenerate LP_{11} modes to split and nullify the results gained here. Tapers also tend to have a diameter that varies slightly across its length that is again due to the intricacies of the fabrication process and is not considered here. Despite these issues PySBS was able to produce values for gain in keeping with those found in the literature, and so provided a valuable tool to analysing these systems.

This work can be expanded and made more accurate with more powerful computer hardware, this would allow for higher density meshes and finer resolution diameter sweeps.

The next chapter describes the physical implementation of these systems and uses some of the information gained here to analyse why the experiments did not produce desirable results as well as assessing the feasibility of the end device.

Chapter 7

A Proposal for A Photonic Switch Using Brillouin Scattering Induced Acoustic Modes in Null-Coupling Fibre Tapers

Optical fibre is used in both academia and industry as a means to transport light without encountering problems concerning the safety and impracticality associated with a free space laser beam. Most commonly this exists as step-index fibre as shown in figure 7.1 and consists of a high refractive index core with a low refractive index cladding, this allows for total internal reflection at the interface between the core and cladding allowing light to easily propagate through the fibre. Many other types of fibre exist, including but not limited to graded index fibre, where the refractive index of the core decreases as the radius increases allowing for the minimisation of modal dispersion, and polarisation maintaining fibre, which include stress rods in their cladding to induce a directional birefringence resulting in the minimisation of cross talk between degenerate polarisation modes [194].

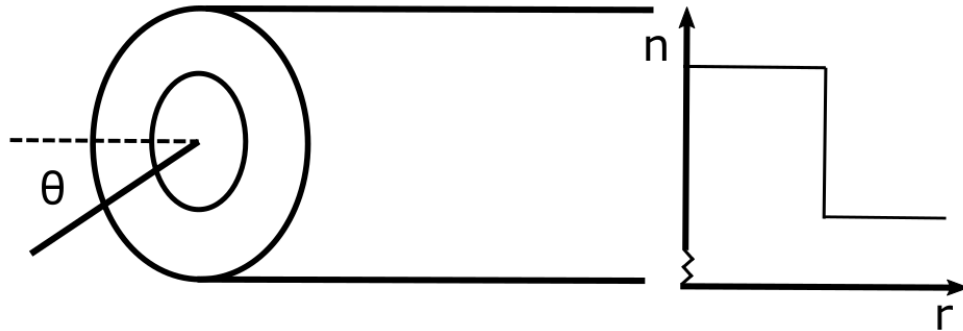


Figure 7.1: Cross section of a step-index fibre with the refractive index as a function of fibre radius, the sharp change at the interface between core and cladding causes light to undergo total internal reflection when it enters the fibre at a maximum angle of θ .

7.1 Fibre Tapers

Optical fibre tapers are fibres that have been stretched to create a section with a smaller diameter. Tapers have unique properties that can be utilised for a range of applications, as shown in figure 7.2, they consist of a normal section with the diameter equal to that of regular fibre (usually $125\mu\text{m}$) followed by a transition, an area where the diameter of the fibre is slowly decreasing along its length, once the transition reaches the desired diameter it is maintained for a certain predetermined length. There are certain instances where this is enough and the fibre is cleaved to form a usable end, or another transition takes place to return the diameter to its original size.

7.1.1 Taper Fabrication

Tapers are fabricated using a flame brush technique (figure 7.2), heat is applied to the fibre by a small oxybutane flame that is hot enough to cross the glass transition temperature of the material, leading to the fibre becoming soft and malleable, the fibre is attached to two linear translation stages at each end that pull and narrow the fibre at the point where heat is being applied. This, in combination with the flame sweeping across the length of the fibre allows for tight control of a variety of taper parameters, such as transition length, waist length, and taper diameter.

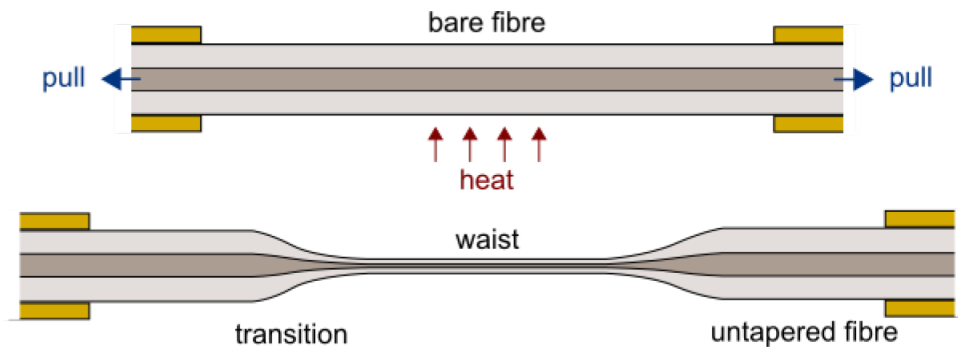
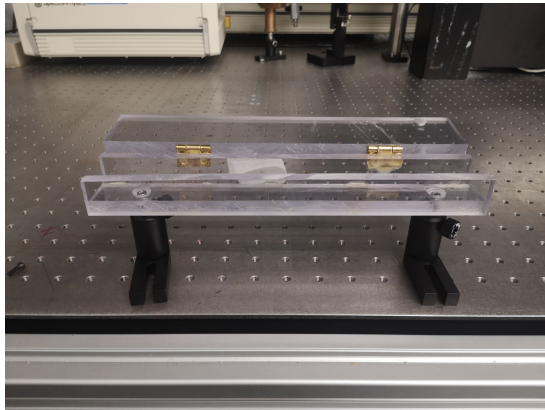
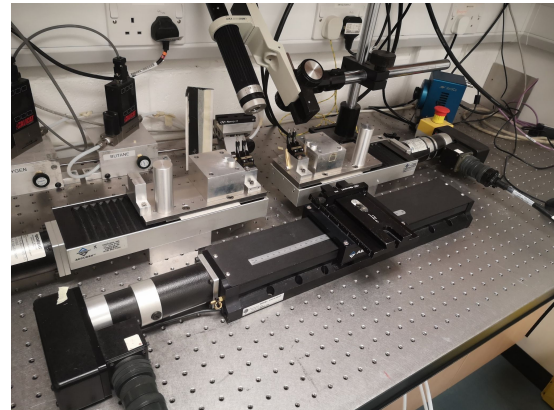


Figure 7.2: Applying heat to a fibre takes it across its glass transition temperature, it is then pulled from both ends to stretch and thin the heated section, the result is a fibre taper. Recreated from [195].

As well as creating basic taper structures, it can also be used to make complex structures, such as photonic lanterns and null coupling fibre tapers, the latter of which will be discussed in more detail in section 7.1.2



(a)



(b)

Figure 7.3: (a) The custom taper mount, designed to encase a taper to reduce dust from settling on the sample and to make transporting tapers easier, and (b) the taper rig, which was used to create tapers.

Commercial taper rigs are available, however the tapers fabricated for experiments presented in this thesis were made by Ross Challinor using a bespoke system developed in the 90s by Tim Birks for early taper experiments. A custom taper holder was built using clear plastic that allowed for the seamless transport of tapers between laboratories and so

that dust would not settle on the device and disturb the acoustic vibrations. This worked well, however, it was found that a simple bracket made out of cardboard worked just as effectively, and in some cases better. Photos of the taper rig and the bespoke sample holder are shown in figure 7.3

7.1.2 Fibre based Couplers and Null Coupling Fibre Tapers

When two tapers of suitable diameter are brought into close confinement, evanescent fields from both fibres interfere and optical power is able to couple between the cores of each taper, this provides the basis for a fibre optic directional coupler and has applications in various fibre based communication systems.

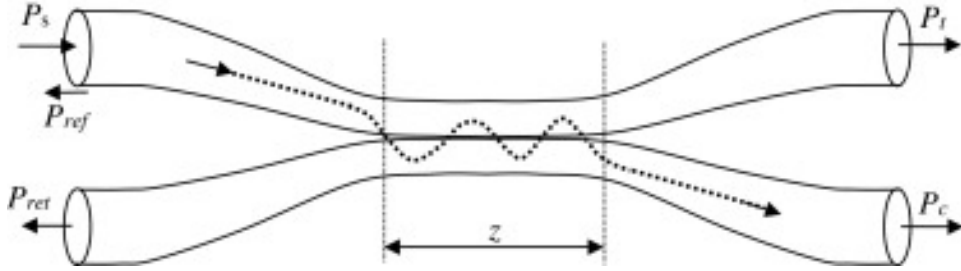


Figure 7.4: When two tapers are brought in close proximity light propagating through one will couple to the core of the second, resulting in an all optical fibre beamsplitter. Reproduced from [196].

From [196], consider two non-identical fibre tapers supporting LP_{01} modes with propagation constants β_1 and β_2 , the power in each fibre can be shown to be

$$\begin{aligned} \frac{P_1(z)}{P_1(0)} &= 1 - \frac{C^2}{\gamma^2} \sin^2(\gamma z) \\ \frac{P_2(z)}{P_1(0)} &= \frac{C^2}{\gamma^2} \sin^2(\gamma z), \end{aligned} \tag{7.1}$$

where P_1 and P_2 are the powers of the two modes, C is the coupling coefficient, z is the lateral distance, $\gamma^2 = C^2 + \frac{1}{4}(\Delta\beta)^2$, and $\Delta\beta = \beta_1 - \beta_2$. The following equation can then be built

$$\frac{C^2}{\gamma^2} = F^2 = \frac{1}{1 + \frac{\Delta\beta^2}{4C^2}}, \quad (7.2)$$

which describes, F , the maximum power fraction and denotes the fractional power that is transferred from one core to another. The sinusoidal dependence results in optical power moving back and forth along the length of the interaction, devices employing this behaviour must therefore carefully consider the length of the device.

Maximal coupling occurs when $\beta_1 = \beta_2$. Before beginning to transfer back, as $\Delta\beta$ increases, the fraction of power that is transferred into the second fibre decreases, until $\Delta\beta$ is large enough to completely stop the transfer of power. The latter case described here is called a null coupling fibre taper.

Fabrication of directional couplers is done using two main techniques, the first is called polished coupling and involves polishing a fibres cladding to expose the core, doing this to two fibres and bringing them close together allows for a highly tunable maximum power fraction but is a labourious process. Instead, fused couplers are often used, which are formed by tapering two twisted single mode fibres together, causing the cores to fuse together. Fused couplers can also be tuned, albeit not actively, by pre-tapering one of the fibres, this causes a change in β and therefore a change in F^2 . Reducing the size of one of the fibres to $80\mu\text{m}$ is enough to create a large enough disparity in propagation constants to form a null coupler.

Fundamental modes within each fibre occupy the lowest two modes of the taper, the LP_{01} and LP_{11} modes, if all transitions are adiabatic, the light entering from one fibre will evolve to only a single mode in the waist and the input and output modes should be identical.

7.2 Null-Coupling Fibre Taper as a Photonic Switch

A paper published in 1996 by Birks *et al* [197] describes a photonic switch based on a null coupling fibre taper. A mechanical vibration induced by a piezoelectric transducer couples the two lowest order modes when certain resonance conditions are met, allowing for a transfer of energy between the first two optical modes in the null coupling fibre. The mechanical vibration causes a periodic refractive index perturbation, resonance occurs when the wavelength of this mechanical vibration is equal to the beat length of the two optical modes. Figure 7.5 shows a schematic for this experiment, and how it could be used as a photonic switch.

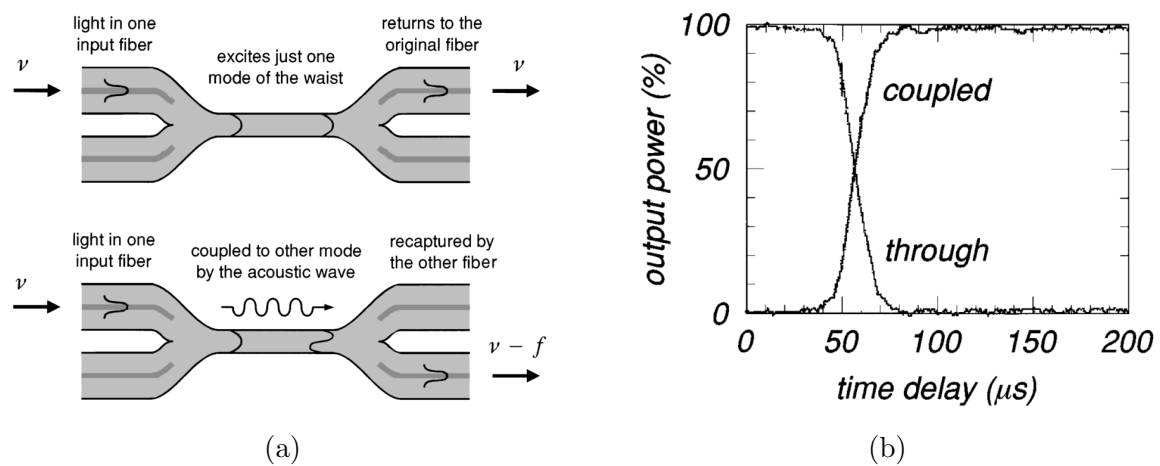


Figure 7.5: (a) The mode of operation for the null-coupling fibre based photonic switch and (b) the results. Reproduced from [197].

This switching mechanism produced strong results, with the piezoelectric transducer capable of coupling electromagnetic modes well enough to facilitate an almost complete power transfer. Since it takes time for the acoustic wave to propagate along the fibre before any switching can occur, the speed of this switch is relatively low (it takes around $50\mu s$), additionally, the need for an external driving force results in a cumbersome device that is not easily marketable. It is possible to describe this switch using forward Brillouin scattering as the dynamics of the two systems are starkly similar.

Birks *et al* produced a device that relies on *spontaneous*¹ intermodal forward Brillouin

¹This is a poor use of the word spontaneous as significant work was done to drive this process, however

scattering, light entering from one arm occupies the fundamental mode in the taper and is scattered into the second order mode as it spontaneously interacts with the induced mechanical wave, allowing it to exit the device through the opposite fibre to which it entered.

Presented in this chapter is the first in a set of experiments that build upon the work done by Birks *et al* [197], where instead of using a piezoelectric transducer, the acoustic modes generated by FSBS are used to couple electromagnetic modes.

7.3 Proof-of-Concept Experiments

To realise this proposal a series of experiments need to be completed, the first of those is to confirm the presence of acoustic modes in a single mode 1×1 taper, this is done with a polarimetry experiment.

Consider the TR_{2m} acoustic mode, the vibration of this mode will naturally have an effect on the strain within the taper, this in turn will induce photoelastic perturbations to the local dielectric tensor, $\Delta\epsilon_{2m}(r, \phi, z, t)$ [198]. As was shown in chapter 3, the effect of the dielectric perturbations on the propagation of optical waves is dependent on their spatial overlap with the optical mode $E_T(r)$, leading to the equation

$$\overline{\Delta\epsilon_{2,m}}(z, t) = \iint \Delta\epsilon_{2,m}(r, \phi, z, t) |E_T(r)|^2 r dr d\phi. \quad (7.3)$$

For a TR_{2m} acoustic mode with principal axes \hat{x} and \hat{y} , the position-averaged dielectric perturbation tensor is then

$$\overline{\Delta\epsilon_{2,m}}(z, t) = \overline{\Delta\epsilon_{2,m}}(\Omega) e^{i(qz - \Omega t)} \begin{pmatrix} 1 & 0 \\ 0 & -1 \end{pmatrix} + c.c. \quad (7.4)$$

Such dielectric perturbations suggest that the TR_{2m} acoustic mode induces a birefringence in the material when it is excited, it is therefore possible to determine the presence of an

the dynamics of the interaction are much more similar to those found in spontaneous interactions than those utilising stimulated Brillouin scattering.

acoustic mode within the taper by analysing the polarisation state of the output light.

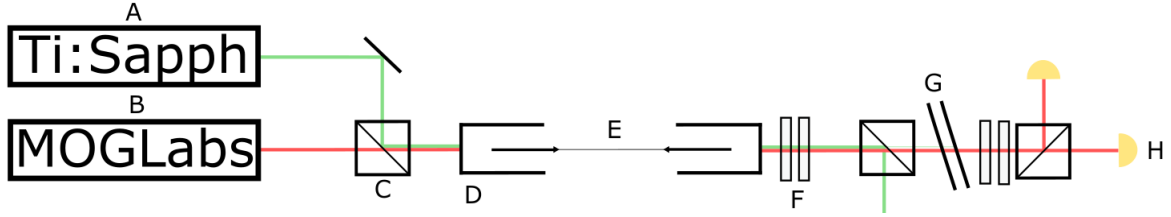


Figure 7.6: Diagram of the polarimetry experiment, the TR_{2m} modes that are excited by the high powered pump beam induce a birefringence that is probed by the signal beam, this has an effect on the output polarisation states. A - Titanium-Sapphire pulsed laser, B - MOGLabs continuous wave laser, C - polarising beam splitter, D - fibre coupling stage, E - fibre taper, F - quarter- and half-waveplates, G - optical filters, and H - detector.

A high powered pump beam of wavelength 805nm and a low powered signal beam of wavelength 780nm are set to co-propagate through a fibre taper of diameter $2.5\mu\text{m}$ and length 6cm made from 780HP single-mode optical fibre produced by Thorlabs, this taper was designed to be long and thin to greatly increase Brillouin gain. The high powered pump beam is from a Spectra-Physics Tsunami Ultrafast Titanium-Sapphire laser, producing pulses at a rate of 80MHz with a (somewhat) tuneable duration ranging from 10ps to 50ps and has a tuneable wavelength.

This experiment operates in a different regime to previous SBS experiments, here, the short pulses result in a large frequency bandwidth that is larger than the Brillouin frequency and can therefore stimulate a light-matter interaction without the need for a signal beam. This is known as impulsive SBS, as opposed to transient SBS that has taken place in previous experiments.

This pump field has an average power of 100mW in the taper and the pulses have a maximum power of 62.5W at the minimum pulse duration, this allows the pump field to excite large numbers of strong acoustic modes in the taper, the signal beam of power 15mW then scatters off these acoustic modes and undergoes the previously described phase shift caused by the induced birefringence of the TR_{2m} modes.

At the output of the taper, the pump beam can be filtered out with polarisation control and a polarising beam splitter due to the orthogonal polarisation of the pump and signal fields at launch. Further filtering comes in the form of an FB790-10 bandpass filter and an FESH0800 shortpass filter, both produced by Thorlabs, that allow for the transmittance of the signal field and the reflectance of the pump field.

A set of waveplates then sets the remaining signal beam to circular polarisation, so that when it is incident on a polarising beam splitter the light is equally distributed between the two output modes. Two PDA8A2 silicon amplified photodetectors, also produced by Thorlabs, were used on each arm of the polarising beam splitter, these amplified detectors have sensitivities of 0.56AW^{-1} and an amplification of 50kVA^{-1} and so are capable of measuring the small changes caused by SBS.

Both detectors are connected to an oscilloscope and the ratio of the signals is taken, when the pump field is on, there will be a strong induction of acoustic modes in the fibre and the signal field will exhibit a polarisation change that is visualised by a change in the ratio of the two output arms of the polarising beam splitter compared to when the pump field is off. A visual description of this setup is shown in figure 7.8, and the results in figure 7.7, here, blue and orange markers correspond to the status of the pump beam and are classified as on and off respectively, the crosses and triangles represent the output from the two different output modes of the beamsplitter.

These results show that the ratio between the two output arms of the polarising beam splitter when the pump is on against when the pump is off have a difference of 0.169. The output arm of a polarising beam splitter has a sinusoidal dependence on input polarisation, from this it is possible to workout applied phase change to the signal beam, which in this case is 0.244rad . In total, 2.33mW was switched from one output arm of the beamsplitter to the other.

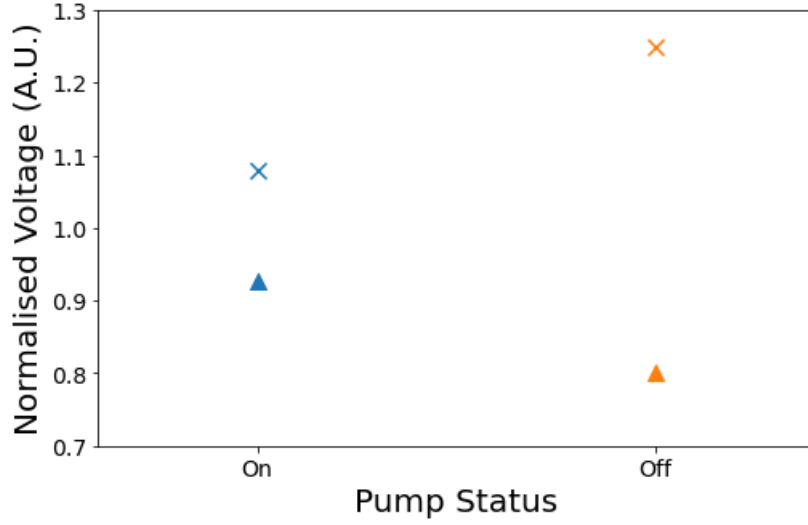


Figure 7.7: The results from this experiment, showing a difference in the ratios of the two arms of a polarising beam splitter equal to 0.169. Crosses and triangles represent the two arms of the polarising beam splitter, blue and orange symbols represent the pump being on and off respectively. Error bars are omitted as they are small (± 0.00760) and were measured using the standard deviation of the time trace.

Although this is a positive and expected result, it is not enough to confirm the presence of Brillouin scattering within the taper as the polarisation change could instead be caused by the Kerr effect, which is another second order non-linear effect that changes the refractive index of a material in response to an applied electric field. This effect could therefore induce a birefringence that would result in a polarisation change, this idea has been studied extensively. The next step is therefore to repeat the experiment but this time attempt to observe the frequency of the scattered light, this observation will guarantee the presence of the desired effect.

Initial experiments functioned in a similar way to those presented in Chapter 5, two MOGLabs lasers detuned by the resonant frequency are set to co-propagate through an optical fibre taper to drive FSBS. This regime unfortunately produced a signal far too small to be measured and so the experiment was adjusted in order to boost the Brillouin response. This system can be analysed in the same way as the analysis of the diamond experiment using the analytical solution to the pump-depletion coupled equations pre-

sented by Boyd [148] in combination with the values of gain produced by the simulations in the previous chapter. For a taper of length 6cm, diameter $2.5\mu\text{m}$ (and therefore of gain $1.87 \times 10^{-4}\text{W}^{-1}\text{m}^{-1}$), and an initial pump-signal power ratio of 2, $1.12 \times 10^{-5}\%$ (or for an initial signal field power of 15mW , $1.68 \times 10^{-7}\text{W}$) of the signal field is scattered, which sits below the noise floor of the electronic spectrum analyser (-100dBm) when detected by an 818-BB-21 photodetector.

A second attempt was made at finding this frequency and changes were implemented in a way to resemble the polarimetry experiment, a strong pulsed pump beam induces acoustic modes which is then filtered off to allow only the detection of a weak signal beam, this time the polarimetry detection system is replaced with a single high-speed detector that is capable of measuring the Brillouin shift.

The taper used here was again made from 780HP fibre produced by Thorlabs, and the detector was 818-BB-21 high-speed (1.2GHz) silicon photodetector produced by Newport optics. Data was visualised with an Agilent 4396B network/spectrum/impedance analyser. A visual description of this setup is shown in figure 7.8.

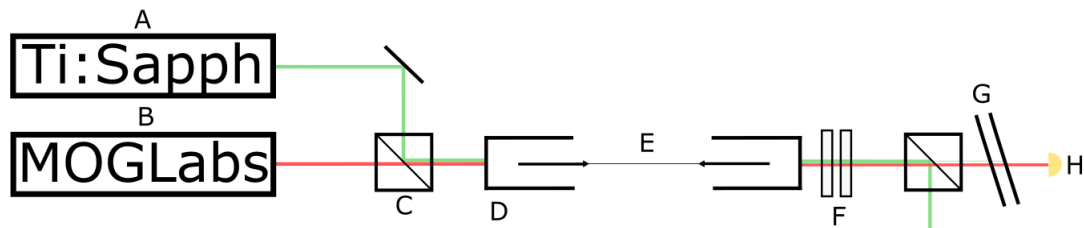


Figure 7.8: Diagram of the experiment used to measure the Brillouin frequency of a fibre taper. A - Titanium-Sapphire pulsed laser, B - MOGLabs continuous wave laser, C - polarising beam splitter, D - fibre coupling stage, E - fibre taper, F - quarter- and half-waveplates, G - dichroic filter, H - detector.

A variety of variables were changed in an attempt to initiate the required interaction, including the power and polarisation of the pump and signal fields and the wavelength of the Ti:Sapph laser which ranged from 800nm to 805nm.

The results of this experiment are inconclusive as a frequency pertaining to Brillouin scattering within the taper could not be observed, there are several reasons for this which are described below.

As soon as fabrication is complete, a fibre taper will begin degrading, gradually reducing the transmittance of light through the fibre until none at all can pass through. There are two primary mechanisms that cause this, water absorption and dust, even with control measures such as enclosing the fibre and monitoring relative humidity tapers will degrade to an unusable level within a matter of days. This made experiments significantly more difficult as the age of the taper increased and could be a contributing factor towards the lack of substantial results.

The process through which tapers are fabricated is controlled with a software that was built in-house, this software takes taper parameters and builds a fabrication process to match, it is unfortunately not always accurate. The various tapers that were fabricated for these experiments could therefore have two potential problems, the first is that the taper parameters were not equal to those that were entered into the software, however this issue is easy to check with the use of a microscope and since tapers have been fabricated for a variety of projects, if this were a serious problem there is a varied group of people that would have noticed something was wrong and corrected it. The second and more likely issue with taper fabrication is that the taper does not have a uniform diameter across its length, this would have the effect of broadening the Brillouin linewidth and decreasing the intensity of the Brillouin peak, perhaps below the noise floor of the detector, as the varying diameter would have a varying Brillouin frequency.

This final point can be modelled using a series of Lorentzian peaks corresponding to Brillouin resonances at different frequencies, each peak is weighted differently based on an error associated with the diameter of the fibre taper so that the summation over all individual peaks produces the expected Brillouin response. This model assumes a

Gaussian distribution of diameters centred around $2.5\mu\text{m}$, the standard deviation is equal to 1%, 5%, 10%, and 50% of the total diameter. Results show that there is a significant decrease in max intensity as the error in diameter increases, shown in figure 7.9.

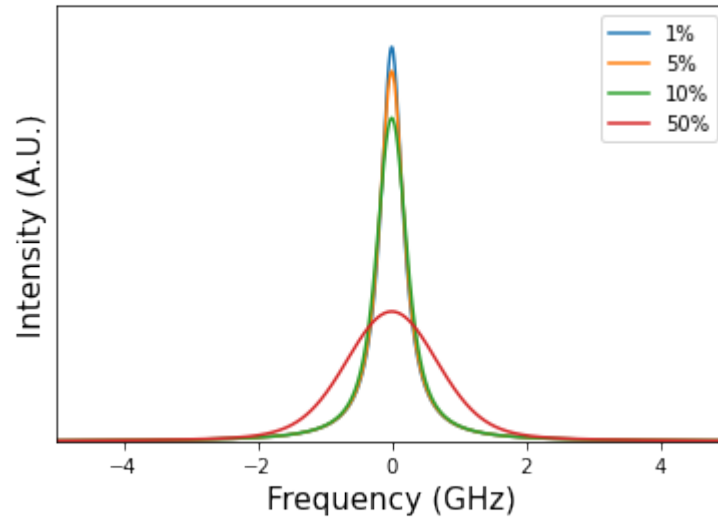


Figure 7.9: Brillouin response as the error in fibre diameter increases from $\sigma = 1\%$ to $\sigma = 50\%$. These results were achieved analytically.

The signal analyser used to observe beat frequencies was old and did not perform well, in particular the electronic noise spectrum that it produced made locating small peaks difficult.

Another issue was the detector that was used, since Brillouin gain increases greatly with lower taper diameter it is desirable to reduce this value as much as possible, however, since the frequency of the mechanical wave increases as taper diameter decreases the bandwidth of the detector severely limits this. It also has a low sensitivity that is not ideal for measuring the subtle frequency changes caused by Brillouin scattering. Brief experiments were completed with an FPD310-FS-VIS silicon PIN amplified photodetector with a bandwidth of 1.5GHz , a sensitivity of 0.5AW^{-1} , and a gain of $2 \times 10^4\text{VW}^{-1}$, this detector would allow for smaller diameter tapers and would be sensitive enough to find low power scattering signals.

Using the values of gain presented in the previous chapter, it is possible to make predic-

tions for the optical power that is scattered by an acoustic field, doing so provides insight into why that experiment didn't produce results and suggestions to changes in experiment design can be made as a result. Beginning with the analysis presented earlier, the total power of scattered light is $10.157\mu\text{W}$.

For the vast majority of experiments, an 818-BB-21 photodetector was used which has a responsivity of 0.47AW^{-1} , a resistance of 50Ω , and produces a voltage of $2.51 \times 10^{-6}\text{V}$ when the scattered signal is detected. Towards the end of this project an amplified photodetector became available for use in experiments, a FPD310-FS-VIS produced by ThorLabs which has a responsivity of 0.5AW^{-1} , a resistance of 50Ω , and a gain of $2 \times 10^4\text{VW}^{-1}$, following the same process, this detector produces a voltage response of $5.35 \times 10^{-2}\text{V}$.

The electronic spectrum analyser used for experiments, an Agilent 4396B, has a noise floor of -145dBm ($1.26 \times 10^{-8}\text{V}$) at its highest resolution which is low enough to produce a SNR enough to yield an accurate peak using either detector. However, in practise the time it takes in order to produce a full spectrum at these resolutions is on the order of hours, in which time lasers drift and stop producing pulses and since the Brillouin frequency has an error associated with it due to fabrication limitations, multiple scans must be taken, making it an unviable option. Increasing the resolution to a manageable level raises the noise floor to -100dBm ($2.24 \times 10^{-6}\text{V}$) meaning that the lower sensitivity detector is not capable of producing a measurable response, but the higher sensitivity detector is.

7.4 Switching Speed

An equation can be built to analyse the switching speed of the device, the first term in this equation accounts for the time it takes for the light to propagate through the taper and the final term accounts for the delay between pump and signal beams.

$$t_{switch} = \frac{n}{2c}L(\bar{\Gamma}) + \tau, \quad (7.5)$$

There is a certain condition for this process, which states that the delay between pump and signal fields must be greater than a quarter of the time period of the acoustic field, $\tau \geq 1/4f$. The need for this arises as a result of the reliance of intermodal scattering on acoustic field amplitude, time scales are short and so if this condition were to be broken ($\tau < 1/4f$) then scattering will not occur at the beginning of the fibre and a full power transfer will not take place.

For a taper length equal to the switching distance, Λ (the extraction of these values will be described in the section 7.5), and $\tau = 1/4f$, the switching speed can be described by figure 7.10. This graph shows that for tapers with diameters less than $2.6\mu\text{m}$, this switching scheme provides an increase in switching speed that increases dramatically at lower diameters over the device this work was based on (Birks *et al* [197], who built a switch that took $50\mu\text{s}$). It also shows, however, that for tapers with diameters larger than $2.6\mu\text{m}$ the switching speed is lower than previous work, something to be considered when building a device.

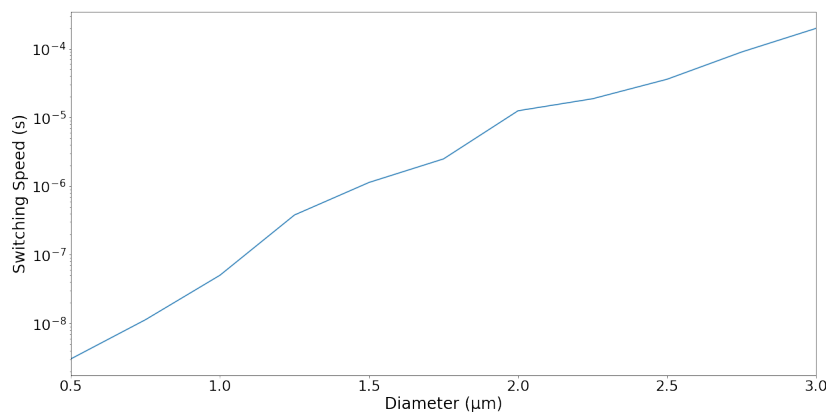


Figure 7.10: Switching speeds calculated from equation 7.5 using switching distances calculated later in the chapter.

7.5 Length Analysis

There are some interesting dynamics that occur as the light propagates down the length of a fibre taper and in order to present an accurate design for a switch these dynamics must be analysed.

The first step is to recap how a switch might operate, as these dynamics will affect how the following simulation is undergone. Two co-propagating pump fields detuned by the Brillouin frequency are directed into the two input ports of a null-coupling fibre taper inducing a high acoustic field amplitude via Brillouin scattering, after a short delay, a signal pulse (or single photon) enters the device through one arm and leaves the device through the opposed fibre. A diagram of this setup is shown in figure 7.11.

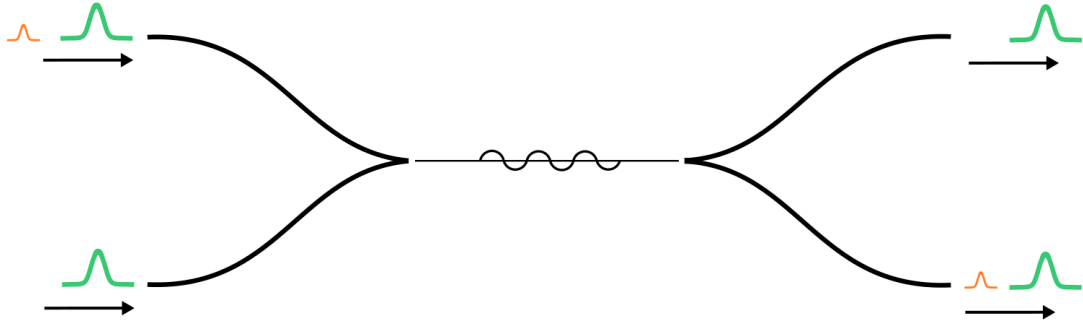


Figure 7.11: Launch conditions and mode of operation for a null-coupling fibre taper switch.

The equations of motion that are derived in chapter 3 are returned to and applied for the case of intermodal forward Brillouin scattering, which are identical to those of intramodal forward Brillouin scattering as they share launch conditions and selection rules

$$\frac{\partial b}{\partial t} + v_0 \frac{\partial b}{\partial z} = i(\Omega - \Omega_0)b - iG^* a_{as}^\dagger a_s \quad (7.6)$$

$$\frac{\partial a_s}{\partial t} + v_p \frac{\partial a_s}{\partial z} = -iGa_{as}b \quad (7.7)$$

$$\frac{\partial a_{as}}{\partial t} + v_s \frac{\partial a_{as}}{\partial z} = -iG^* b^\dagger a_s. \quad (7.8)$$

The phonon dissipation rate, $\bar{\Gamma}/2$, is introduced as the delay between initial pump pulses

and the signal pulse allows for some relaxing of the acoustic field. For the forward Brillouin scattering case, this dissipation rate is high (in the range of MHz) and the group velocity is near zero, the spatial evolution can then be ignored [199]. This in conjunction with the desire to find steady state solutions means that $\partial b/\partial t = \partial b/\partial z = \partial a_{as}/\partial t = \partial a_s/\partial t = 0$. The equations then become

$$0 = i(\Omega - \Omega_s)b + \frac{\bar{\Gamma}}{2}b - iG^*a_{as}^\dagger a_s, \quad (7.9)$$

$$\frac{\partial a_s}{\partial z} = -\frac{1}{v_p}iGa_{as}b, \quad (7.10)$$

$$\frac{\partial a_{as}}{\partial z} = -\frac{1}{v_s}iG^*b^\dagger a_s, \quad (7.11)$$

where G is the coupling strength of the electromagnetic and acoustic fields

$$|G|^2 = \frac{1}{4}v_s v_p \bar{\Gamma} \hbar \omega_p g. \quad (7.12)$$

Now only considering 7.10 and 7.11, the differential of these equations are

$$\frac{\partial}{\partial z} \frac{\partial a_s}{\partial z} = -\frac{1}{v_p}iGb \frac{\partial a_{as}}{\partial z} \quad (7.13)$$

$$\frac{\partial}{\partial z} \frac{\partial a_{as}}{\partial z} = -\frac{1}{v_s}iG^*b^\dagger \frac{\partial a_s}{\partial z}. \quad (7.14)$$

Substituting in equations 7.10 and 7.11 gives

$$\frac{\partial}{\partial z} \frac{\partial a_s}{\partial z} = \left(-\frac{1}{v_p}iGb\right)\left(-\frac{1}{v_s}iG^*b^\dagger a_s\right) = -\frac{1}{v_s v_p}G^2 b^2 a_s \quad (7.15)$$

$$\frac{\partial}{\partial z} \frac{\partial a_{as}}{\partial z} = \left(-\frac{1}{v_s}iG^*b^\dagger\right)\left(-\frac{1}{v_p}iGa_{as}b\right) = -\frac{1}{v_p v_s}G^2 b^2 a_{as}. \quad (7.16)$$

These equations take the form of the simple harmonic oscillator and therefore have solutions

$$a_s(z) = A \cos\left(\sqrt{\frac{G^2 b^2}{v_p v_s}}z\right) \quad (7.17)$$

$$a_{as}(z) = A \cos \left(\sqrt{\frac{G^2 b^2}{v_s v_p}} z \right). \quad (7.18)$$

Returning now to equation 7.9, setting the detuning to zero and rearranging gives an equation for B

$$b = \frac{2}{\Gamma} i G a_s^\dagger a_{as} w. \quad (7.19)$$

Using this equation it is possible to find the amplitude of the acoustic field generated by the two pump fields in the first stage of the switching mechanism, consequently equations 7.17 and 7.18 can then be used to find how the power distribution between LP_{01} and LP_{11} vary as a function of taper length z for the propagation of the signal beam.

Earlier in this chapter it was found that there is a non-linear dependence on gain as taper diameter varies and that for the specific case of intermodal Brillouin scattering of both the TR_{21} and the R_{01} acoustic modes, the gain has a maxima at $1.91 \times 10^{-6} \text{W}^{-1} \text{m}^{-1}$ with a diameter of $0.5 \mu\text{m}$. The standard relation between intensity, power, and electric field strength is

$$I = \frac{P}{A} = \frac{cn\epsilon_0}{2} |E|^2. \quad (7.20)$$

In order to achieve a switching distance (Λ) that is as short as possible, the pump lasers must produce pulses with high peak powers. Commercially available systems at the higher end of what is available can produce pulses with a peak power of 40kW, and so this figure will be used in the following simulation. The pump system operates in the transient regime.

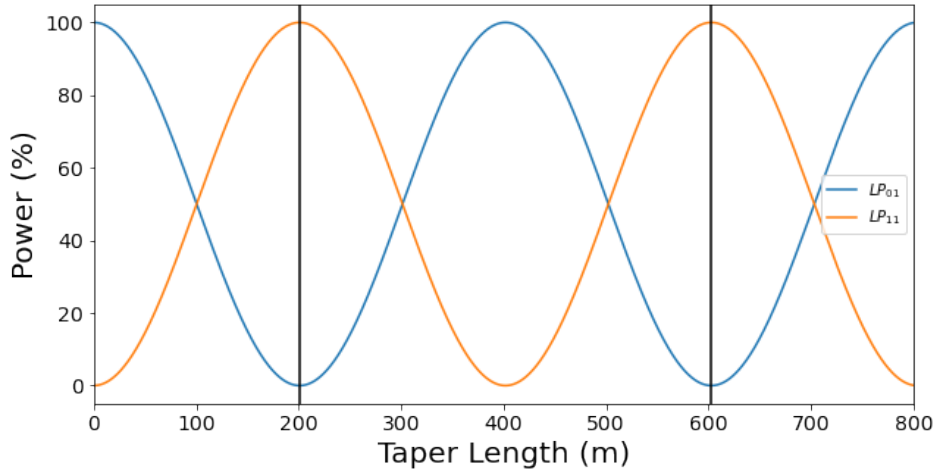


Figure 7.12: Power of a signal beam distribution between LP_{01} and LP_{11} modes as a function of taper length for a taper of diameter $2.5\mu m$. In this simulation the acoustic wave has already been excited by two high powered pump beams.

This result shows that there are periodic lengths where a complete transfer of power between LP_{01} and LP_{11} modes in the fibre taper is possible, null-coupling fibre taper photonic switches of diameter $2.5\mu m$ must therefore have length equal to $n201m$, where $n = 1, 3, 5, \dots$ to achieve complete switching of an input pulse (photon).

Tapers of this length will not be possible to fabricate with the facilities available for this project (or at all, for that matter). However, the gain values for intermodal scattering from both the R_{01} and TR_{01} modes produced in Chapter six can be used in conjunction with the aspect ratio (defined as equal to the ratio of length to diameter) of already fabricated tapers to find taper diameters that could produce viable devices.

The results presented here assume a phonon decay rate, $\bar{\Gamma}$ of zero, as the instantaneous acoustic field amplitude caused by the pump fields is used. With the addition of a decay rate, full power transfer is still possible but occurs at an increasing length that is proportional to the delay between pump and signal beams, τ .

Many tapers were produced during this project with varying aspect ratios, that with the highest was of length 6cm and diameter $2.5\mu m$, producing an aspect ratio of 2.4×10^4 .

This will be used as a figure of merit to judge whether a taper is capable of being produced or not. Figure 7.13 shows the distance required for a full transfer of power (Λ) as a function of taper diameter, with a black line corresponding to the aspect ratio of the best performing taper that was able to be fabricated, diameters sitting beneath this line are those that fit this criteria. This model assumes that there is a linear dependence on maximum aspect ratio as a function of taper diameter, which needs further study to confirm.

This result shows that fibres up to a diameter of $0.905\mu\text{m}$ can be fabricated in order to achieve a device capable of full switching. Tapers of this diameter can be comfortably fabricated using the taper rig available.

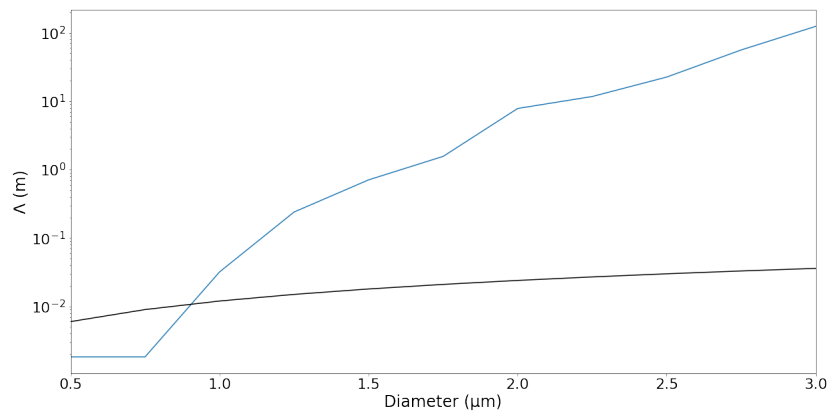


Figure 7.13: Switching distance presented as a function of taper diameter, the black line indicates an aspect ratio equal to that of the best performing taper that was able to be produced during this project. Points sitting below this line are those that can be reliably fabricated as per this figure of merit.

Although the figure of merit used here was for the best performing taper fabricated during this project, it does not represent the physical limit of what is possible. Should work be done to improve the aspect ratio, the potential for higher diameter devices increases which is desirable as they are much more durable.

The strong pump fields used here produce powers in the taper and the high mode confinement at lower diameters means that the intensity of light in a taper is large. The optical

damage threshold for silica is 1.3GWcm^{-1} [200], plotting the absolute power threshold as a function of taper diameter produces the following graph.

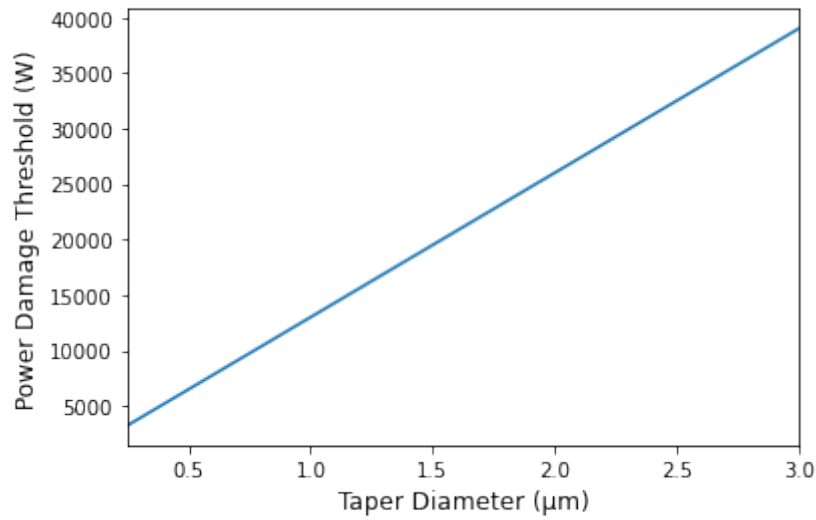


Figure 7.14: Shown here is the maximum possible absolute power that a taper of certain length is able to transmit without being damaged.

From this it is clear to tell that the lasers used in this simulation will critically damage any device considered viable by the previous analysis. This can be overcome with the use of lower powered lasers, but this change comes at the cost of Λ , which will increase as a result and negatively affect the aspect ratio, pushing more taper diameters above the criteria.

Repeating the aspect ratio simulation (figure 7.15) with pump powers capable of being produced in house (62.5W peak power, from the Spectra Physics Ti:Sapph) shows that even at the shortest taper distances, a full transfer of power occurs at a distance several orders of magnitude larger than what is physically capable of being fabricated.

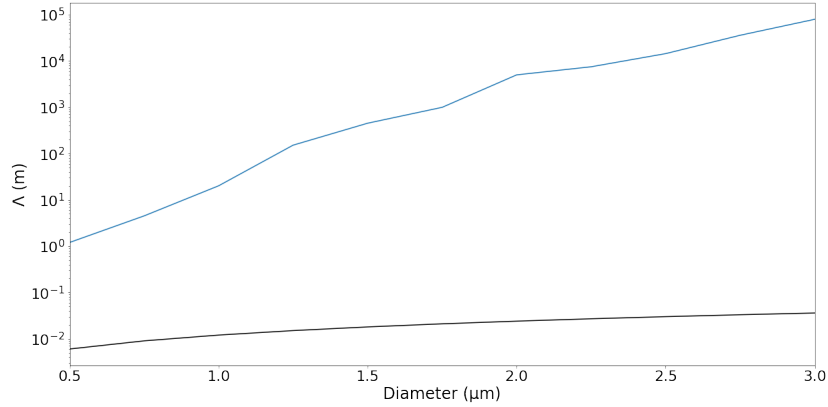


Figure 7.15: Switching distance presented as a function of taper diameter, the black line indicates a aspect ratio equal to that of the best performing taper that was able to be produced during this project and the blue line indicates the distance necessary for a full switching event to occur. Points sitting below this line are those that can be reliably fabricated as per this figure of merit.

From this, it can be deduced that this is not a feasible device. Even with the high powered pump scheme, which is difficult to implement both physically and economically, using light at such high powers is enough to comfortably destroy any device it is used in conjunction with, moving then to a more realistic pump system shows that Λ is consistently greater than the limit of what is physically capable of being fabricated.

7.6 Further Work

There are many ways in which the experiments presented in this chapter can be improved upon. Beginning with the polarimetry experiment, the Kerr effect is instantaneous in nature whereas an acoustic mode will continue to impose birefringence on the taper for a time after the pulse has passed through the taper, this left over birefringence depends on the phonon decay rate, Γ . It is possible to use this in order to deduce the source of the polarisation change with the addition of a high-pass filter into the system, the pulsed laser has a repetition rate of 80MHz and so the Kerr effect and the polarisation rotation will share this frequency, blocking out signals below this frequency will then eliminate contributions from the Kerr effect leaving only those from the presence of acoustic modes, and therefore Brillouin scattering in the frequency spectrum. If it is the acoustic mode

producing this result, the expected outcome of this experiment will look identical to the results already presented in this chapter, as the addition of a filter eliminates the possibility of the effect being the result of the Kerr effect

Even with this addition to the polarimetry experiment, it is still not enough to determine whether or not Brillouin scattering is taking place within the taper, there are a number of changes that could be made to the second experiment presented here in order to aid the detection of the Brillouin frequency.

The first of those is to move from free-space optics to fibre optics, this would allow for the fine control of polarisation before the taper and to achieve higher extinction ratios of the pump beam. Although the stimulation of acoustic modes is achievable with orthogonally polarised pump and signal beams, it is less efficient than the case of identical polarisation states between pump and signal beams. A diagram of this proposed experiment is given in figure 7.16

There should also be greater care taken to ensure the uniformity of the taper diameter, this can be done easily with post-fabrication analysis using a microscope and if taper diameter does indeed vary enough to have a significant effect on FSBS then the taper can be made shorter to ensure a higher degree of uniformity.

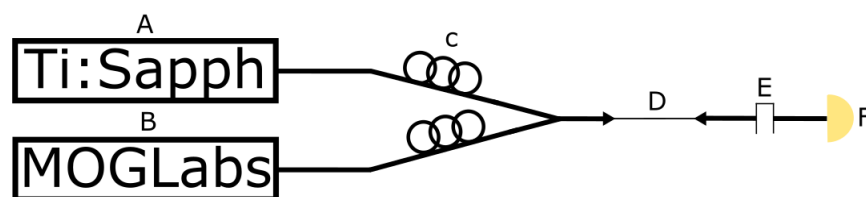


Figure 7.16: Proposed experiment to measure the Brillouin frequency of a fibre taper featuring an all-fibre optics design. A - Titanium-Sapphire pulsed laser, B - MOGLabs continuous wave laser, C - fibre polarisation control, D - fibre taper, E - bandpass filter, F - detector.

Naturally, the next step is to examine Brillouin interactions in a null-coupling fibre taper, this would require a similar setup to the previous experiment but this time light would be

focussed into the two input arms of the device and the ratio of the output arms compared to the ratio of the input arms, a difference in these values when the pump is turned on and off would suggest that light in the taper is undergoing intermodal FSBS.

From here, based on the results of the previous experiment, single photons can be used in the taper to confirm its efficacy at switching quantum information and a device can be manufactured that employs a null-coupling fibre taper in order to switch quantum information. Such a device can be linked with a cavity to form a switchable cavity quantum memory.

These steps will still be useful even with the negative outcome of the feasibility analysis, as confirming parameters such as switching length physically will help confirm this. The maximum aspect ratio of a taper could be increased which may open up the possibility of a feasible device.

Chapter 8

Summary and Conclusions

Throughout this thesis, progress has been made towards using Brillouin scattering as a tool to achieve two different devices that contribute to the field of photonic computing and linear optics quantum computing.

In order to begin these experiments, preliminary data was taken regarding the saturated absorption and two-photon absorption of rubidium vapour, which allows further experiments to be completed that measure the induced susceptibility. With the completion of this measurement, two switchable cavity quantum memories will be built. The first uses the induced susceptibility change caused by two counter-propagating pump fields to create a Bragg grating in the material, light is then trapped between a stationary mirror and this induced Bragg grating. The second changes the susceptibility of rubidium in a ring cavity, which in turn changes the resonances of the cavity.

Two (formal) attempts have been made to measure the Brillouin linewidth of diamond, using a single laser with a sideband created by an electro-optic modulator equal to the Brillouin frequency and by using two separate lasers detuned by the Brillouin frequency. Neither of these attempts were successful, and since these experiments took place this figure has been established in the literature. Further experiments will employ cavities to increase intra-diamond power, increasing Brillouin interactions and finally pulses will be used in an attempt to store and retrieve light.

Further Brillouin scattering experiments have taken place in fibre tapers with the goal of creating a photonic switch made of a null-coupling fibre taper that uses the acoustic field induced by Brillouin scattering to switch light from one electromagnetic mode to another. The first of these experiments measures the polarisation change that a signal field experiences due to the induced birefringence of a TR_{2m} acoustic mode, results showed a significant change in polarisation suggesting the presence of these modes but the polarisation change experienced here is indistinguishable from the birefringence induced by the Kerr effect and so further experiments must be completed to confirm this.

The second of these experiments functions in a similar way to how the Brillouin interaction in diamond was measured, two fields with a detuning equal to the Brillouin frequency are set to co-propagate through a taper and measured to observe the frequency of the acoustic field, also similar to the diamond experiment were the results, which did not give the desired outcome. Finally, a high powered pulsed laser is used to drive high powered acoustic fields which scatters light of dissimilar wavelength, once measured, the result should produce a beat frequency equal to that of the acoustic field, but no such frequency was detected.

Finite-element analysis was used to simulate Brillouin scattering in both diamond and fibre tapers, two Python packages were used called FeNICS and PySBS that took input geometries and material properties and produced electromagnetic modes, acoustic modes, and Brillouin gain. The results of these simulations produced full Brillouin linewidths for three different crystal orientations of diamond, and allowed for the analysis of taper diameters effect on Brillouin gain.

This work culminates in the ability to analyse the feasibility of both of these devices. From the simulation work, values for gain for specific crystal orientations of diamond were found and were used to analyse the distance over which information can be stored, this happened to be 6.36cm which is short in comparison to what is available. This,

along with the acoustic phonon lifetimes presented in Chapter 4, indicated that a quantum memory utilising Brillouin scattering is feasible and that work should be continued towards this goal.

Again from the simulation work, the intermodal Brillouin gain could be found as a function of fibre taper diameter, which in turn could be used to analyse the dynamics of light as it passes along the length of the taper. It was found that for realistic pump powers that could be achieved in the lab, full switching of light could not occur in tapers with aspect ratios capable of being produced in-house. However, this limit could be pushed with an increase in aspect ratio, which could be possible with significant work.

Appendix A

A Mathematical Model of Brillouin Scattering

This appendix describes some of the background material necessary for a full understanding of the ideas presented in the bulk text, it begins with a derivation of both optical and acoustic phonons and goes on to describe classical and quantum characterisations of stimulated Brillouin scattering in a more detailed manner to that presented in chapter 3.

A.1 Lattice Vibrations in Crystals

The Lennard-Jones potential is a mathematical model that describes the soft attractive and repulsive forces between two electronically neutral atoms or molecules [125], as a result of these forces atoms will equilibrate at a set distance from each other where the energy that the system occupies is at a minimum. The attractive force is described by the Van der Waals forces acting on the atoms and follows a $1/r^6$ relation with separation distance, the repulsive force is described by electron orbitals overlapping (i.e. Pauli exclusion principle) and follows a $1/r^{12}$ relation with separation distance. Combining these terms gains the following

$$E_{LJ} = \frac{A}{r^{12}} - \frac{B}{r^6}, \quad (\text{A.1})$$

where E_{LJ} is the potential energy of the system, r is the separation between the two atoms, and A and B are material constants. Figure A.1 shows both terms and how in combination they create a system with a minimum energy at a finite distance away from the atom.

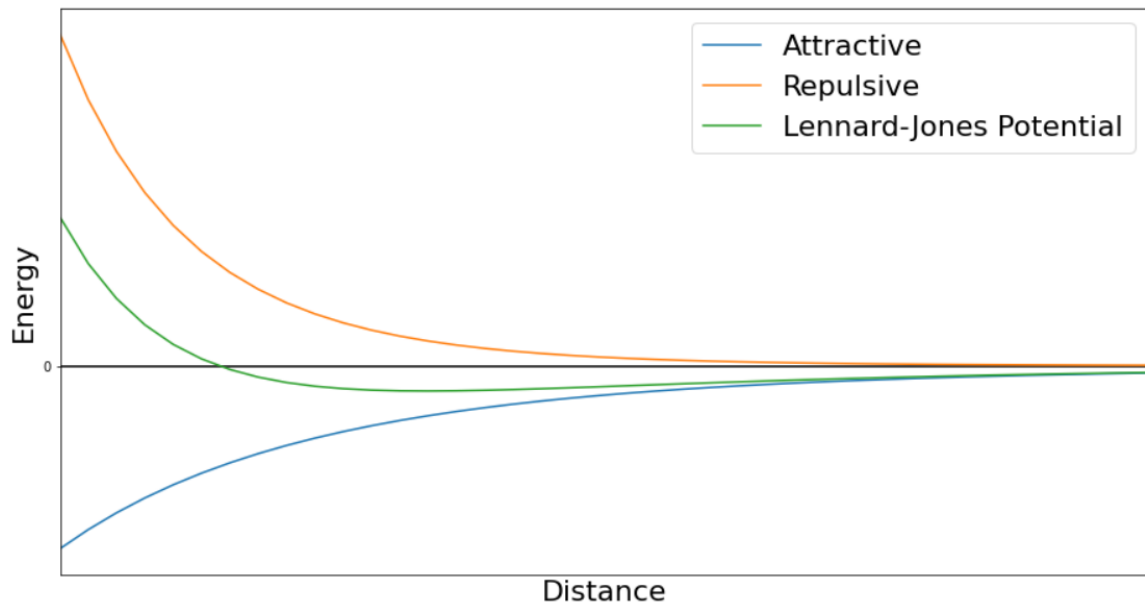


Figure A.1: Graph describing Van der Waals attractive forces, orbital overlap repulsive forces, and the resulting Lennard-Jones potential.

In a crystal, this potential is associated with every atom in the lattice, the potential energies add up and produce an array of wells in which each atom is able to stably sit, however, these wells are shallow and as such the atoms within them are able to oscillate freely. When one atom moves position it will effect the position of the potential field surrounding it, causing atoms nearby to move in a way as to prevent the potential energy increasing, and causes waves to propagate through the material. The energy of these waves is quantised, and so it is often easier to think of them as quasiparticles called phonons. Following is a derivation of the mechanics of these phonons taken from Kittel [125].

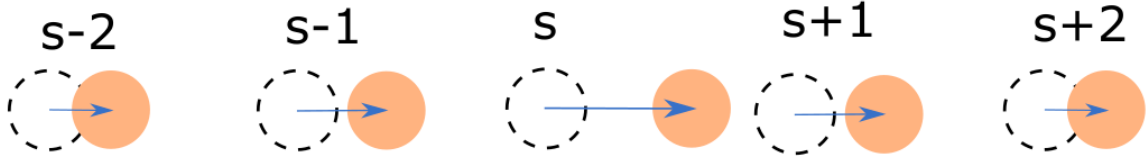


Figure A.2: One-dimensional chain of identical atoms, a small displacement on one will influence the position of nearby atoms, creating regular oscillations known as phonons.

The frequency, ω of a phonon is proportional to its wavenumber, \mathbf{k} , the associated dependency is called the dispersion relation and describes the dispersive effects of a medium on waves that propagate through it [201]. Simplifying a crystal to a linear chain of identical atoms of mass m , connected via spring-like bonds with force constant C , the position of the central atom is denoted as x_s , and its nearest neighbours as x_{s-1} and x_{s+1} as shown in figure A.2. The force, \mathbf{F}_s , acting on an atom is given by

$$\mathbf{F}_s = m \frac{d^2 x_s}{dt^2}. \quad (\text{A.2})$$

Hooke's law, $\mathbf{F}_s = Cx_s$, can be used to express the force applied in terms of the displacement of the atoms and the force constant, taking into account the relative displacements between the central atom and its nearest neighbours gives

$$\mathbf{F}_s = C(x_{s-1} - x_s) + C(x_{s+1} - x_s) = C(x_{s+1} + x_{s-1} - 2x_s). \quad (\text{A.3})$$

These oscillations can be represented as a wave using the equation

$$x_s = Ae^{i\omega t} = Ae^{i\mathbf{k}sa}, \quad (\text{A.4})$$

where ω is the angular frequency, t is time, A is the amplitude, and a is the equilibrium lattice spacing. Differentiating the second term twice with respect to time gives

$$\frac{d^2 x_s}{dt^2} = -\omega^2 Ae^{i\omega t} = -\omega^2 x_s. \quad (\text{A.5})$$

This allows an expression for force independent of time

$$-m\omega^2 x_s = C(x_{s+1} + x_{s-1} - 2x_s). \quad (\text{A.6})$$

Replacing the coordinate values with the final term of eq. A.4

$$-m\omega^2 e^{iksa} = C(e^{ik(s+1)a} + e^{ik(s-1)a} - 2e^{iksa}) = Ce^{iksa}(e^{ika} + e^{-ika} - 2). \quad (\text{A.7})$$

This simplifies to

$$\omega^2 = \frac{2C}{m} (1 - \cos(ka)) = \frac{4C}{m} \sin^2\left(\frac{ka}{2}\right). \quad (\text{A.8})$$

One final step gives the dispersion relation for a monatomic chain

$$\omega(\mathbf{k}) = \sqrt{\frac{4C}{m}} \left| \sin\left(\frac{\mathbf{k}a}{2}\right) \right|. \quad (\text{A.9})$$

This produces the graph shown in figure A.3, wavenumber along the horizontal axis is normalised to a . Only the wavenumbers from $-\frac{\pi}{a}$ to $\frac{\pi}{a}$ (or those within the Brillouin zone) need to be presented as any oscillation outside of this area is indistinguishable from one within it.

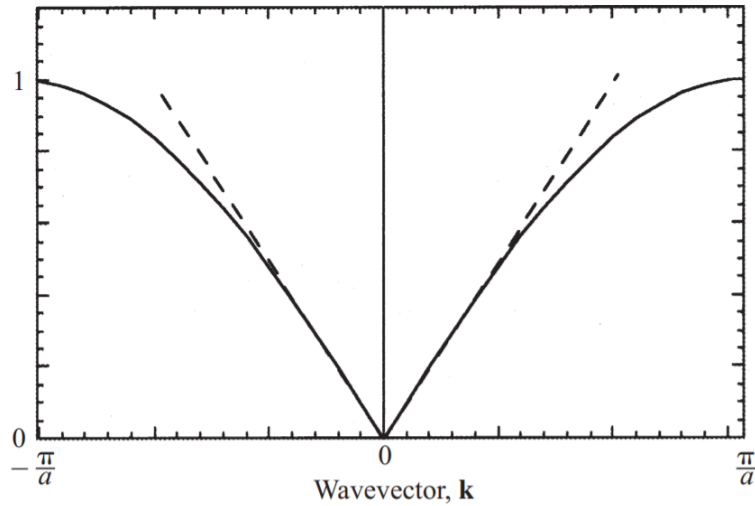


Figure A.3: Dispersion curve caused by a one-dimensional chain of identical atoms as described by equation A.9. The dotted line describes $\mathbf{k} = \omega$ to show the linearity of the dispersion curve at low \mathbf{k} . Reproduced from [126].

The monatomic chain model is only effective for crystal structures with a single atom in

their unit cell, for a full description of phonon propagation in crystals the case where there are two atoms per unit cell must also be examined. Consider the case of a diatomic chain, where atoms of high and low mass (M and m) alternate along a linear, one-dimensional plane. In this case, the position of the atoms are u and v for each mass respectively, s encapsulates one atom of each mass, all bonds have the same force constant, C , and the lattice parameter, a , is the distance between two identical atoms.

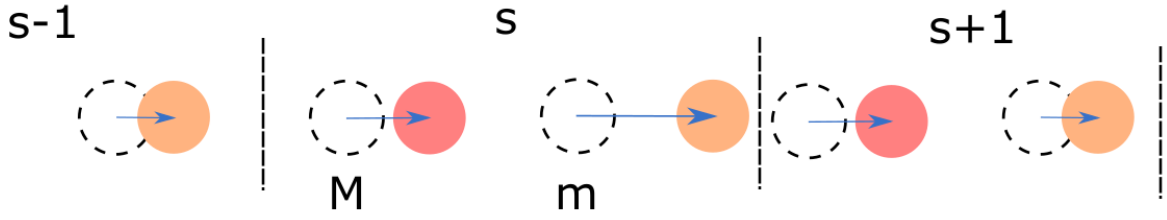


Figure A.4: One-dimensional chain of atoms with alternating high and low masses, a small displacement on one will influence the position of nearby atoms, creating regular oscillations known as phonons.

Similar to the case of a monatomic chain, the first step is to take the relative difference in displacement between the central atom and its two nearest neighbours, this must be done for both atoms in the unit cell.

$$\begin{aligned}\mathbf{F}_u &= M \frac{d^2 u_s}{dt^2} = C(v_s + v_{s-1} - 2u_s), \\ \mathbf{F}_v &= m \frac{d^2 v_s}{dt^2} = C(u_{s+1} + u_s - 2v_s).\end{aligned}\tag{A.10}$$

Once again, the oscillating atoms can be described as waves in space and time, but this time the two atoms will have different amplitudes, u and v

$$\begin{aligned}u_s &= u e^{i s k a} e^{-i \omega t}, \\ v_s &= v e^{i s k a} e^{-i \omega t}.\end{aligned}\tag{A.11}$$

Differentiating twice with respect to time gives

$$\begin{aligned}\frac{d^2 u_s}{dt^2} &= -\omega^2 u e^{i s \mathbf{k} a} e^{-i \omega t}, \\ \frac{d^2 v_s}{dt^2} &= -\omega^2 v e^{i s \mathbf{k} a} e^{-i \omega t},\end{aligned}\tag{A.12}$$

which can be substituted into equations A.10 and simplified to produce a pair of coupled equations

$$\begin{cases} -\omega^2 M u &= C v (1 + e^{-i \mathbf{k} a}) - 2 C u \\ -\omega^2 m v &= C u (1 + e^{i \mathbf{k} a}) - 2 C v \end{cases}.\tag{A.13}$$

These equations can be rearranged, written as a determinant, and solved to get the solution

$$M m \omega^4 - 2 C (M + m) \omega^2 + 2 C^2 [1 - \cos(\mathbf{k} a)] = 0.\tag{A.14}$$

Finally, solving for ω and simplifying gives the equation used to describe the phonon dispersion relation

$$\omega^2(\mathbf{k}) = \frac{C(M + m)}{M m} \pm C \sqrt{\frac{(M + m)^2}{M^2 m^2} - \frac{4}{M m} \sin^2\left(\frac{\mathbf{k} a}{2}\right)}.\tag{A.15}$$

This equation gives rise to two branches, representing to two different types of phonon in a material, the higher frequency band corresponds to optical phonons and the lower frequency band corresponds to acoustic phonons (figure A.5). Optical phonons are named as such because of their movement patterns, for an ionic crystal with atoms of alternating charge the atoms of an optical phonon will move against each other and will have a fixed center of mass, this type of motion is able to be excited with the electric field of a light wave. The atoms in an acoustic phonon move with each other and have an oscillating center of mass much like in long wavelength acoustic vibrations, hence their name.

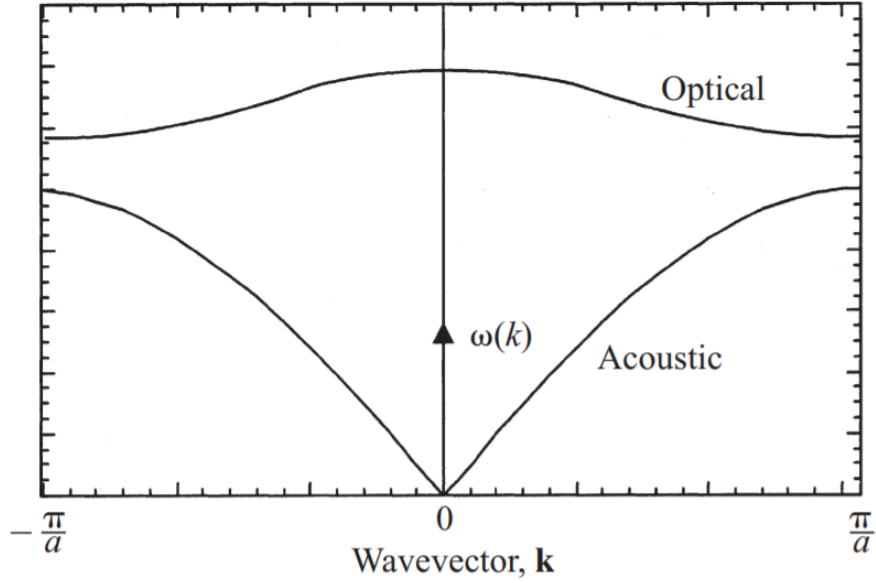


Figure A.5: Dispersion curve caused by a one-dimensional chain of atoms with alternating high and low masses as described by equation A.9. The higher frequency band is caused by optical phonons and the lower is caused by acoustic phonons. Reproduced from [126].

Waves in a crystal can move in both transverse and longitudinal patterns, and so more lines in a dispersion relation will arise as a result of the number of degrees of freedom a particular crystal has. If there are p atoms in the primitive cell, there will be $3p$ branches to the phonon dispersion relation: 3 acoustic branches and $3p - 3$ optical branches [125].

The primary mechanism by which phonons arise in a material is due to the random motion of atoms induced by their temperature, as a result phonons play a pivotal role in the transfer of heat across a material, effecting material properties such as heat capacity. There will therefore be phonons present in any material above 0K, noise caused by phonons can be reduced by cooling the sample to near this level.

A.2 The Three Contributions to Brillouin Scattering

Consider two beams of different wavelength passing through a bulk material and occupying the same spacial mode, a high powered pump beam with amplitude, frequency, and wavevector $(E_p, \omega_p, \mathbf{k}_p)$, and a low powered signal beam with amplitude, frequency, and

wavevector $(E_s, \omega_s, \mathbf{k}_s)$. As these two beams propagate they will beat together to form a standing wave, which will induce a periodic density variation caused by electrostriction. When the frequency difference between the pump and signal beam is equal to the frequency of a phonon mode (u, Ω, \mathbf{q}) in the material, a resonant energy transfer takes place to dramatically boost the power of the signal beam. There are a number of selection rules associated with this process accounting for the conservation of energy and momentum

$$\Omega = \omega_p - \omega_s, \quad (\text{A.16})$$

$$\mathbf{q} = \mathbf{k}_p + \mathbf{k}_s. \quad (\text{A.17})$$

Electrostriction is the tendency of a dielectric material to compress under a high local electric field leading to areas of higher density. It is a non-linear effect, meaning that the strength of the interaction has a non-linear relation with electric field strength. More precisely, it is a non-linear interaction between polarisation (in this context referring to the induced electric dipole moment per unit volume) and electric field strength, described by expressing polarisation, $\mathbf{P}(t)$, as a power series in the field strength $\mathbf{E}(t)$

$$\mathbf{P}(t) = \epsilon_0(\chi^{(1)}\mathbf{E}(t) + \chi^{(2)}\mathbf{E}^2(t) + \chi^{(3)}\mathbf{E}^3(t) + \dots), \quad (\text{A.18})$$

where ϵ_0 is the permittivity of free space, $\chi^{(1)}$ is the linear susceptibility, and $\chi^{(2)}$ and $\chi^{(3)}$ are the second- and third-order non-linear optical susceptibilities. The physical origin of the various linear and non-linear susceptibilities comes from a materials symmetry and how an atom is able to oscillate in a potential well, for condensed matter, $\chi^{(1)}$ is unity, and higher order susceptibilities $\chi^{(2)}$ and $\chi^{(3)}$ are on the order of 10^{-12} and 10^{-24} respectively. An assortment of effects arises as a result of non-linear optics, including second harmonic generation [128], optical parametric oscillation [129], and sum- and difference-frequency generation [130].

Following the derivation presented in [202], electrostriction is a third order non-linear effect and the potential energy in a material caused by the phenomena is given by

$$u = \frac{1}{2}\epsilon\epsilon_0 E^2, \quad (\text{A.19})$$

where ϵ is the relative dielectric constant and E is the electric field strength. The magnitude of electrostrictive forces can be found using the electrostriction tensor

$$\sigma_{ij} = -\frac{1}{2}\epsilon_0 n^4 p_{ijkl} E_k E_l, \quad (\text{A.20})$$

where n is the refractive index, p_{ijkl} is the photoelastic tensor, the total electric field for two waves in the same spatial mode is given by $(\mathbf{E}_p e^{i(\mathbf{k}_p x - \omega_p t)} + \mathbf{E}_s e^{i(\mathbf{k}_s x - \omega_s t)})/2 + c.c.$. Inserting this into equation A.20 and filtering out the components with frequency Ω , the time-harmonic electrostrictive tensor of the form $\sigma_{ij} e^{i(\mathbf{q}x - \Omega t)}$ is given, with components

$$\begin{bmatrix} \sigma_{xx} \\ \sigma_{yy} \\ \sigma_{zz} \\ \sigma_{yz} \\ \sigma_{xz} \\ \sigma_{xy} \end{bmatrix} = -\frac{1}{2}\epsilon_0 n^4 \begin{bmatrix} p_{11} & p_{12} & p_{13} & & & \\ p_{12} & p_{22} & p_{23} & & & \\ p_{13} & p_{23} & p_{33} & & & \\ & & & p_{44} & & \\ & & & & p_{55} & \\ & & & & & p_{66} \end{bmatrix} \begin{bmatrix} E_{px} E_{sx}^* \\ E_{py} E_{sy}^* \\ E_{pz} E_{sz}^* \\ E_{py} E_{sz}^* + E_{pz} E_{sy}^* \\ E_{px} E_{sz}^* + E_{pz} E_{sx}^* \\ E_{px} E_{sy}^* + E_{py} E_{sx}^* \end{bmatrix}. \quad (\text{A.21})$$

The divergence of the electrostrictive tensor gives the bulk electrostrictive force, and so equation A.41 becomes $\mathbf{f}^{ES} e^{i(\mathbf{q}x - \Omega t)}$ with components

$$f_x^{ES} = -i\mathbf{q}\sigma_{xx} - \partial_y \sigma_{xy} - \partial_z \sigma_{xz}, \quad (\text{A.22})$$

$$f_y^{ES} = -i\mathbf{q}\sigma_{xy} - \partial_y \sigma_{yy} - \partial_z \sigma_{yz}, \quad (\text{A.23})$$

$$f_z^{ES} = -i\mathbf{q}\sigma_{xz} - \partial_y \sigma_{zy} - \partial_z \sigma_{zz}. \quad (\text{A.24})$$

For larger materials, the bulk electrostriction component of SBS far exceeds the boundary electrostriction and radiation pressure components, however when devices begin to reach nanometer scales the two boundary effects vastly outweigh the bulk electrostriction component due to an excess of material boundaries. The discontinuity of optical powers and photoelastic constants generates stress (and therefore electrostrictive forces) that contribute to the overall effect, taking the divergence of equation A.20 in a similar way to before the boundary electrostrictive forces between material 1 and 2 becomes $\mathbf{F}^{ES} e^{i(\mathbf{q}x - \Omega t)}$

with components

$$F_i^{ES} = (\sigma_{1ij} - \sigma_{2ij})n_j, \quad (\text{A.25})$$

where n_j is a normal vector that points from material 1 to material 2. When an electromagnetic field is incident on a material interface, there is an exchange of momentum between the field and the material resulting in a mechanical pressure being exerted on the material, this is known as radiation pressure and makes up the final component of SBS. The forces associated with radiation pressure can be derived from the Maxwell Stress Tensor (MST), a second-order symmetric tensor that represents the interaction between electromagnetic forces and mechanical momentum. The electric part of MST is

$$T_{ij} = \epsilon_0 \epsilon (E_i E_j - \frac{1}{2} \delta_{ij} E^2), \quad (\text{A.26})$$

where δ_{ij} is the Kronecker delta. The pressure between material 1 and 2 is

$$F_i^{RP} = (T_{2ij} - T_{1ij})n_j. \quad (\text{A.27})$$

When the normal and tangential components of the electric field are resolved with respect to the dielectric interface $\mathbf{E} = E_n \mathbf{n} + E_t \mathbf{t}$, and using the boundary conditions $\epsilon_1 E_{1n} = \epsilon_2 E_{2n} = D_n$ and $E_{1t} = E_{2t} = E_t$, it can be shown that

$$\mathbf{F}^{RP} = -\frac{1}{2} \epsilon_0 E_t^2 (\epsilon_2 - \epsilon_1) \mathbf{n} + \frac{1}{2} \epsilon_0^{-1} D_n^2 (\epsilon_2^{-1} - \epsilon_1^{-1}) \mathbf{n}. \quad (\text{A.28})$$

Like with both electrostriction components, if the total electric field, $(\mathbf{E}_p e^{i(\mathbf{k}_p x - \omega_p t)} + \mathbf{E}_s e^{i(\mathbf{k}_s x - \omega_s t)})/2 + c.c.$, is inserted into equation A.28 and the components with frequency Ω are filtered out, the result is a time-harmonic radiation pressure of the form $F^{RP} e^{i(qx - \Omega t)}$, with components

$$\mathbf{F}^{RP} = -\frac{1}{2} \epsilon_0 E_{pt} E_{st}^* (\epsilon_2 - \epsilon_1) \mathbf{n} + \frac{1}{2} \epsilon_0^{-1} D_{pn} D_{sn}^* (\epsilon_2^{-1} - \epsilon_1^{-1}) \mathbf{n}. \quad (\text{A.29})$$

This equation shows that the forces caused by radiation pressure are always normal to the dielectric interface, pointing from the high to the low index medium.

The Brillouin gain is an important figure when discussing the efficiency of SBS processes, it is defined as the ratio of input to output power of the signal field. Brillouin gain can be found using the overlap integral between the optical forces and the elastic displacement, the first step in deriving this is to describe how power is transferred between pump and signal fields along the axis of propagation direction (x) [148]

$$\frac{dP_s}{dx} = gP_pP_s - \alpha_sP_s, \quad (\text{A.30})$$

where P_p and P_s is the power of the pump and signal fields respectively, g is the SBS gain, and α_s is the sound absorption coefficient. By utilising particle flux conservation, SBS can be expressed as

$$g(\Omega) = \frac{\omega_s}{2\Omega P_p P_s} \text{Re} \left\langle \mathbf{f}, \frac{d\mathbf{u}}{dt} \right\rangle, \quad (\text{A.31})$$

where \mathbf{f} is the total optical forces generated by the interaction of the pump and signal waves, and \mathbf{u} is the elastic deformation caused by \mathbf{f} . The inner product between two vector fields is defined as the overlap integral over the material cross-section

$$\langle \mathbf{A}, \mathbf{B} \rangle \triangleq \int \mathbf{A}^* \cdot \mathbf{B} ds. \quad (\text{A.32})$$

The optical power, $P = \nu_g \langle \mathbf{E}, \epsilon \mathbf{E} \rangle / 2$, where ν_g is the optical group velocity can be substituted into equation A.31 to give

$$g(\Omega) = \frac{2\omega_s}{\nu_{gp}\nu_{gs}} \frac{\text{Im} \langle \mathbf{f}, \mathbf{u} \rangle}{\langle \mathbf{E}_p, \epsilon \mathbf{E}_p \rangle \langle \mathbf{E}_s, \epsilon \mathbf{E}_s \rangle}. \quad (\text{A.33})$$

This can be further simplified by considering the ideal case, neglecting the elastic loss, with a elastic response $\mathbf{u}e^{-i\Omega t}$ caused by a force $\mathbf{f}e^{-i\Omega t}$. From Royer [203],

$$-\rho\Omega^2 u_i = \frac{\partial}{\partial x_j} c_{ijkl} \frac{\partial u_i}{\partial x_k} + f_i, \quad (\text{A.34})$$

where ρ is the mass density, and c_{ijkl} is the elastic tensor. There two important properties of the elastic tensor that are worth noting, first, it is symmetric with respect to the first

two and last two indices ($c_{ijkl} = c_{jikl}, c_{ijkl} = c_{ijlk}$), and the interchange of the first two and last two indices does not affect the value ($c_{ijkl} = c_{klij}$) [203]. Using these properties it is possible to show that the operator on the left hand side of equation A.34 is Hermitian, since without a driving force, \mathbf{f} , equation A.34 becomes the eigen-equation for elastic waves. Therefore, the eigen-mode $\mathbf{u}_m e^{-i\Omega_m t}$ satisfies the orthogonality condition

$$\langle \mathbf{u}_m, \rho \mathbf{u}_n \rangle = \delta_{mn} \langle \mathbf{u}_m, \rho \mathbf{u}_m \rangle. \quad (\text{A.35})$$

When including \mathbf{f} , \mathbf{u} can be decomposed in terms of it's eigenmodes $\mathbf{u} = \sum_m b_m \mathbf{u}_m$. Using equation A.35,

$$b_m = \frac{\langle \mathbf{u}_m, \mathbf{f} \rangle}{\langle \mathbf{u}_m, \rho \mathbf{u}_m \rangle} \frac{1}{\Omega_m^2 - \Omega^2}, \quad (\text{A.36})$$

where Ω_m is frequency of the mechanical wave. Consider now the case with elastic loss. The first-order effect of loss can be found by changing Ω_m to a complex value, $\Omega_m - i\Gamma_m/2$. Assuming a quality factor $Q_m = \Omega_m/\Gamma_m$ much larger than one,

$$b_m = \frac{\langle \mathbf{u}_m, \mathbf{f} \rangle}{\langle \mathbf{u}_m, \rho \mathbf{u}_m \rangle} \frac{1}{\Omega_m^2 - \Gamma_m} \frac{\Gamma_m/2}{\Omega_m - \Omega - i\Gamma_m/2}. \quad (\text{A.37})$$

Γ_m is the Brillouin linewidth, relating to the damping parameter by $\Gamma_m = \mathbf{q}^2 \bar{\Gamma}$. Inserting equation A.37 into equation A.33 shows that the total SBS gain is the sum of SBS gains of individual elastic modes, expressed as

$$g(\Omega) = \sum_m G_m \frac{(\Gamma_m/2)^2}{(\Omega - \Omega_m)^2 + (\Gamma_m/2)^2}, \quad (\text{A.38})$$

where G_m is the peak value, defined by

$$G_m = \frac{2\omega Q_m}{\Omega_m^2 \nu_{gp} \nu_{gs}} \frac{|\langle f, u_m \rangle|^2}{\langle E_p, \epsilon E_p \rangle \langle E_s, \epsilon E_s \rangle \langle u_m, \rho u_m \rangle}. \quad (\text{A.39})$$

SBS falls in to two categories depending on launch conditions. When the pump and signal beams are counter-propagating through a material, the process reverses the direction of travel of the scattered light, and when the pump and signal beams are co-propagating through a material the process does not reverse the direction of travel of the scattered

light. This is known as Backwards Stimulated Brillouin Scattering (BSBS) and Forward Brillouin Scattering (FSBS) respectively. Both BSBS and FSBS are explored thoroughly in this thesis, and so it is useful to examine the varying mechanics of these processes.

In BSBS, electromagnetic fields are travelling in opposite directions, and so $E_p = E$, $E_s = E^*$, and $q = 2k$ since $k_p = k_s$ to good approximation. Equation A.41 then becomes

$$\begin{bmatrix} \sigma_{xx} \\ \sigma_{yy} \\ \sigma_{zz} \\ \sigma_{yz} \\ \sigma_{xz} \\ \sigma_{xy} \end{bmatrix} = -\frac{1}{2}\epsilon_0 n^4 \begin{bmatrix} p_{11} & p_{12} & p_{13} & & & \\ p_{12} & p_{22} & p_{23} & & & \\ p_{13} & p_{23} & p_{33} & & & \\ & & & p_{44} & & \\ & & & & p_{55} & \\ & & & & & p_{66} \end{bmatrix} \begin{bmatrix} E_x^2 \\ E_y^2 \\ E_z^2 \\ 2E_y E_z \\ 2E_x E_z \\ 2E_x E_y \end{bmatrix}. \quad (\text{A.40})$$

All components of the electrostriction tensor are non-zero and so the electrostriction force generates both longitudinal and transverse components.

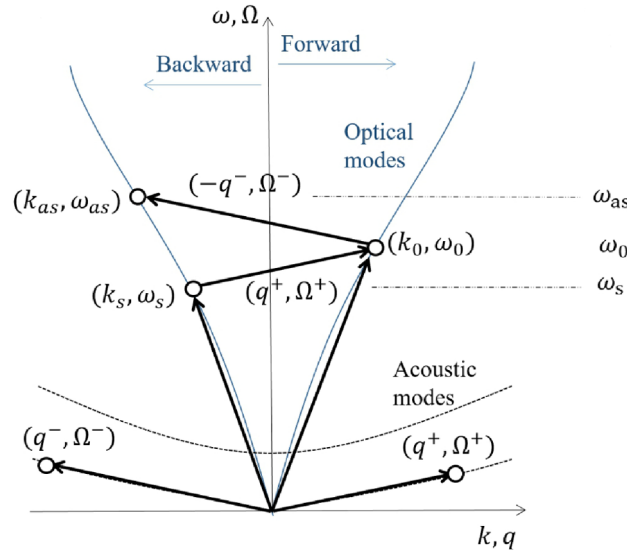


Figure A.6: Dispersion diagram for backwards Brillouin scattering. Reproduced from Wolff *et al* [204].

In FSBS, electromagnetic fields are travelling in the same direction, and so $E_p = E_s = E$, and equation 3.3 becomes $q = 0$. Equation A.41 becomes

$$\begin{bmatrix} \sigma_{xx} \\ \sigma_{yy} \\ \sigma_{zz} \\ \sigma_{yz} \\ \sigma_{xz} \\ \sigma_{xy} \end{bmatrix} = -\frac{1}{2}\epsilon_0 n^4 \begin{bmatrix} p_{11} & p_{12} & p_{13} & & & \\ p_{12} & p_{22} & p_{23} & & & \\ p_{13} & p_{23} & p_{33} & & & \\ & & & p_{44} & & \\ & & & & p_{55} & \\ & & & & & p_{66} \end{bmatrix} \begin{bmatrix} |E_x|^2 \\ |E_y|^2 \\ |E_z|^2 \\ 2\text{Re}(E_y E_z^*) \\ 0 \\ 0 \end{bmatrix}. \quad (\text{A.41})$$

It is shown here that σ_{xz} and σ_{xy} are both zero, using this in equations A.23, and A.25, gives $f_x^{ES} = F_x^{ES} = 0$. This shows that any electrostrictive forces are purely transverse. While forward Brillouin scattering can occur in bulk media, the increase in the surface area to volume ratios for nanoscale systems such as waveguides lends itself to forward Brillouin scattering and so devices employing this effect are often very small.

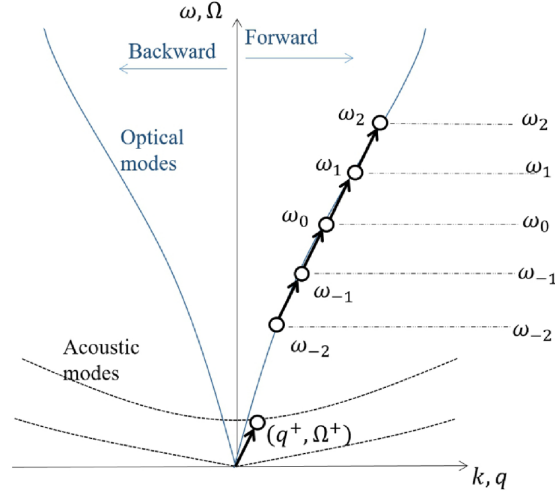


Figure A.7: Dispersion diagram for forwards Brillouin scattering. Reproduced from Wolff *et al* [204].

A.3 Quantising SBS

There are various interpretations of quantum mechanics that attempt to explain how the mathematical descriptions of quantum systems correspond to reality, one such interpretation is the Heisenberg interpretation, which takes state vectors as time-independent and therefore constant and operators to have a time dependence. This is in contrast to the Schrodinger interpretation, where state vectors have a time dependence but observables do not, this difference can be thought of as a change of reference frame in Hilbert space.

The Heisenberg interpretation is gained from the Schrodinger interpretation by applying a unitary operator \hat{U} on state vector $|\psi(t)\rangle_H$, the result is the Heisenberg equation of motion which describes how a system changes in time

$$\frac{d\hat{A}_H}{dt} = \frac{1}{i\hbar} [\hat{A}_H, \hat{H}], \quad (\text{A.42})$$

where \hat{A}_H is an operator in the state $|\psi(t)\rangle_H$ and \hat{H} is the Hamiltonian, an expression that amounts to the total energy contained within a system. The square brackets in this case denote a canonical commutation relation, which describe the fundamental relation between canonical conjugate quantities (quantities where the Fourier transform of one is equal to the other) and can be expanded as $[\hat{A}_H, \hat{H}] = \hat{A}_H \hat{H} - \hat{H} \hat{A}_H$. From this, the full equations of motion for both forward and backward SBS can be derived, the first step of which is find the systems Hamiltonian, this takes the form

$$H = H^{ph} + H^{\text{opt}} + H^{\text{int}}, \quad (\text{A.43})$$

where H^{ph} , H^{opt} , and H^{int} are the Hamiltonian's used to describe the acoustic field, optical field, and the acousto-optic interaction respectively. The following section provides a brief derivation of all three of these Hamiltonian's and applies them to find the equations of motion for backward and forward Brillouin scattering in terms of envelope operators. This derivation is for the generalised case of Brillouin scattering in a waveguide, however can be applied to bulk optical systems. The acoustic Hamiltonian can be represented by the sum of the kinetic and potential energy

$$H^A = \int \frac{\pi^i(\mathbf{r})\pi^i(\mathbf{r})}{2\rho(\mathbf{r})} d\mathbf{r} + \frac{1}{2} \int S^{ij}(\mathbf{r})c^{ijkl}(\mathbf{r})S^{kl}(\mathbf{r})d\mathbf{r}, \quad (\text{A.44})$$

and can be quantised as

$$H^{ph} = \int dq \hbar \Omega(q) b_q^\dagger b_q, \quad (\text{A.45})$$

where b_q^\dagger and b_q are the creation and annihilation operators for the q th phonon mode that encapsulates the time evolution of each mode amplitude, $\pi(\mathbf{r})$ is the conjugate momenta,

$\rho(\mathbf{r})$ is density, $S^{ij}(\mathbf{r})$ is the linearised strain tensor operator, and $c^{ijkl}(\mathbf{r})$ is the stiffness tensor. The full Hamiltonian includes the sum over all branches of acoustic dispersion, but focussed on here is a single acoustic field with dispersion $\Omega(q)$. Since the acoustic field given here is driven, it has a well defined carrier wavevector q_0 , and so the phonon-mode envelope operator is introduced $b(z) = 1/\sqrt{2\pi} \int dq b_q e^{i(q-q_0)z}$ which peaks around the carrier wavevector allowing the the acoustic field to evolve in space. $b_e(z)b_e(z)^\dagger$ then represents the phonon number per unit length. Substituting the inverse Fourier transform $b_q = 1/\sqrt{2\pi} \int dz b(z) e^{-i(q-q_0)z}$ into equation 3.45, the Hamiltonian becomes

$$H^{ph} = \int dz \hbar b^\dagger(z) \hat{\Omega}_z b(z), \quad (\text{A.46})$$

where the Taylor expansion of $\Omega(q)$ around q_0 results in the operator

$$\hat{\Omega}_z = \sum_{n=0}^{\infty} \frac{1}{n!} \left. \frac{\partial^n \Omega}{\partial q^n} \right|_{qD} \left(-i \frac{\partial}{\partial z} \right)^n. \quad (\text{A.47})$$

A caveat of this definition is that this linewidth must be small, which is indeed the case for Brillouin interaction.

The electromagnetic Hamiltonian can be derived in a similar way. Standard arguments in electromagnetic theory lead to an expression for the energy density

$$H^{\text{ed}} = \int \mathbf{H} \cdot d\mathbf{B} + \int \mathbf{E} \cdot d\mathbf{D}, \quad (\text{A.48})$$

where \mathbf{H} is the magnetising field, \mathbf{B} is the magnetic flux density, \mathbf{E} is the electric field, and \mathbf{D} is the electric displacement field. This can be expanded and split into linear and non-linear terms. The quantised solution is then

$$H = \sum_{\alpha} \hbar \omega_{\alpha} a_{\alpha}^{\dagger} a_{\alpha}, \quad (\text{A.49})$$

where a_{α}^{\dagger} and a_{α} are the photon creation and annihilation operators, and ω_{α} is frequency of a mode α . The photon-mode envelop, $a_s(z) = 1/\sqrt{2\pi} \int dk a_{\gamma k} e^{i(k-k_{\gamma})z}$, is introduced in a similar fashion as with the acoustic Hamiltonian, the inverse Fourier transform $a_{\gamma k}(z) =$

$1/\sqrt{2\pi} \int dk a_s(z) e^{-i(k-k_\gamma)z}$ is substituted into equation 3.49

$$H^{\text{EM}} = \sum_{\gamma} \int dk \hbar \hat{\omega}_z a_s^\dagger a_s. \quad (\text{A.50})$$

Over all modes γ and with the corresponding spatial operator

$$\hat{\omega}_z = \sum_{n=0}^{\infty} \frac{1}{n!} \frac{\partial^n \omega}{\partial k^n} \bigg|_k \left(-i \frac{\partial}{\partial z} \right)^n. \quad (\text{A.51})$$

The light matter interaction is introduced with the new quantity $\beta^{ij}(\mathbf{r})$, which is the total inverse relative dielectric tensor

$$\beta^{ij}(\mathbf{r}) = \delta^{ij} \beta_{\text{ref}}(\mathbf{r}) + \bar{\beta}^{ij}(\mathbf{r}; [\mathbf{u}(\mathbf{r})]). \quad (\text{A.52})$$

The coupling between optical and acoustic fields arises as a result of the dependence of $\beta^{ij}(\mathbf{r})$ on displacement field $\mathbf{u}(\mathbf{r})$ through its reliance on the strain in the material and the motion of the interfaces. The opto-acoustic coupling can then be written as

$$H^{\text{int}} = \frac{1}{2\epsilon_0} \int D^i(\mathbf{r}) \tilde{\beta}^{ij}(\mathbf{r}; [\mathbf{u}(\mathbf{r})]) D^j(\mathbf{r}) d\mathbf{r}, \quad (\text{A.53})$$

where ϵ_0 is the permittivity of free space. Neglecting two-photon interactions and only taking the significant terms of the above equation (those that contain creation and annihilation operators of photons, which have a much greater energy than those of phonons), the interaction Hamiltonian reduces to

$$\begin{aligned} H^{\text{int}} = & \sum_{\gamma, \gamma', \alpha} \int \frac{dk}{(2\pi)^{3/2}} \frac{dk' dq}{(2\pi)^{3/2}} a_s^\dagger a_{as} b \int G(\gamma k; \gamma' k'; \alpha q) e^{i(k' - k + q)z} dz \\ & + \sum_{\gamma, \gamma', \alpha} \int \frac{dk}{(2\pi)^{3/2}} \frac{dk' dq}{(2\pi)^{3/2}} b^\dagger a_{as}^\dagger a_s \int G^*(\gamma k; \gamma' k'; \alpha q) e^{-i(k' - k + q)z} dz \end{aligned} \quad (\text{A.54})$$

Where primed operators indicate their belonging to the signal field, and for a acoustic mode α . The coupling parameter introduced here includes contributions from bulk electrostriction and surface effects such as boundary electrostriction and radiation pressure, it can be reduced for convenience

$$\bar{G}(\gamma k; \gamma' k'; \alpha q) = \frac{1}{\sqrt{(\hbar\omega_{\gamma k})(\hbar\omega_{\gamma' k'}) (\hbar\Omega_{\alpha q}) |v_{\gamma k} v_{\gamma' k'} v_{\alpha q}|}} G(\gamma k; \gamma' k'; \alpha q) \quad (\text{A.55})$$

Where $v_{\gamma k}$, $v_{\gamma' k'}$, and $v_{\alpha q}$ are the velocities of the pump, signal, and acoustic fields respectively. And expanded to include separate expressions for bulk and surface effects

$$\bar{G}(\gamma k; \gamma' k'; \alpha q) = \bar{G}_{\text{bulk}}(\gamma k; \gamma' k'; \alpha q) + \bar{G}_{\text{surf}}(\gamma k; \gamma' k'; \alpha q) \quad (\text{A.56})$$

Which, in turn, can be described by the following

$$\begin{aligned} \bar{G}_{\text{bulk}}(\gamma k; \gamma' k'; \alpha q) &= \frac{1}{\epsilon_0} \frac{1}{2\sqrt{2} |\nu_{\gamma k} v_{\gamma' k'} v_{\alpha q}|} \\ &\quad \times \int dx dy (d_{\gamma k}^i(x, y))^* d_{\gamma' k'}^j(x, y) p^{ijm}(x, y) s_{\alpha q}^{\text{ln}}(x, y) \\ \bar{G}_{\text{surf}}(\gamma k; \gamma' k'; \alpha q) &= -\frac{1}{\epsilon_0} \frac{1}{2\sqrt{2} |v_{\gamma k} v_{\gamma' k'} v_{\alpha q}|} \\ &\quad \times \int dx dy (d_{\gamma k}^i(x, y))^* d_{\gamma' k'}^j(x, y) \left(\frac{\partial \beta_{\text{ref}}(x, y)}{\partial r^j} \right) u_{\alpha q}^j(x, y) \end{aligned} \quad (\text{A.57})$$

The full Hamiltonian can then be built, featuring acoustic, electromagnetic, and acoustooptic interaction contributions

$$\begin{aligned} H &= \int dz \hbar b^\dagger(z) \hat{\Omega}_z b(z) \\ &\quad + \sum_{\gamma} \int dk \hbar \omega_z a_s^\dagger a_s \\ &\quad + \sum_{\gamma, \gamma', \alpha} \int \frac{dk dk' dq}{(2\pi)^{3/2}} a_s^\dagger a_{\alpha s} b \int G(\gamma k; \gamma' k'; \alpha q) e^{i(k' - k + q)z} dz \\ &\quad + \sum_{\gamma, \gamma', \alpha} \int \frac{dk dk' dq}{(2\pi)^{3/2}} b^\dagger a_s^\dagger a_s \int G^*(\gamma k; \gamma' k'; \alpha q) e^{-i(k' - k + q)z} dz, \end{aligned} \quad (\text{A.58})$$

With the full Hamiltonian of this system fully derived, it is possible to apply it to equation 3.42 in order to retrieve the full Heisenberg equations of motion for pump, signal, and acoustic fields. These equations follow the same basic form for both forward and backward Brillouin scattering, differing only on the launch conditions of the optical fields. For

acoustic, pump, and signal fields of the form

$$\begin{aligned}
 \mathbf{U} &= b(z, t) \mathbf{y}(x, y) e^{i(qz - \Omega t)} + \text{c.c.} \\
 E_p &= a_s(z, t) e_1(x, y) e^{i(k_p z - \omega_p t)} + \text{c.c.} \\
 E_a &= a_{as}(z, t) e_2(x, y) e^{i(k_x z - \omega_x t)} + \text{c.c.}
 \end{aligned}
 \tag{A.59}$$

For backwards Brillouin scattering, ignoring the anti-Stokes scattered field and obeying the selection rules (equations A.16 and A.17), the equations of motion are then

$$\begin{aligned}
 \frac{\partial B}{\partial t} - v_0 \frac{\partial b}{\partial z} &= i(\Omega - \Omega_0) b + iG^* a_{as}^\dagger a_s \\
 \frac{\partial a_s}{\partial t} + v_p \frac{\partial a_s}{\partial z} &= iG a_{as} b \\
 \frac{\partial a_{as}}{\partial t} - v_s \frac{\partial a_{as}}{\partial z} &= iG^* b^\dagger a_s.
 \end{aligned}
 \tag{A.60}$$

Using the same criteria for forward Brillouin scattering, the equations of motion are

$$\begin{aligned}
 \frac{\partial b}{\partial t} + v_0 \frac{\partial b}{\partial z} &= i(\Omega - \Omega_0) B - iG^* a_{as}^\dagger a_s \\
 \frac{\partial a_s}{\partial t} + v_p \frac{\partial a_s}{\partial z} &= -iG a_{as} b \\
 \frac{\partial a_{as}}{\partial t} + v_s \frac{\partial a_{as}}{\partial z} &= -iG^* b^\dagger a_s,
 \end{aligned}
 \tag{A.61}$$

Where G is related to Brillouin gain g by the equation

$$g = \frac{4|G|^2}{v_s v_p \Gamma_m \hbar \omega_p} \frac{\left(\frac{\Gamma_m}{2}\right)^2}{(\Omega - \Omega_0)^2 + \left(\frac{\Gamma_m}{2}\right)^2}
 \tag{A.62}$$

Appendix B

Finite Element Analysis

The Finite Element Method (FEM) is a numerical method that is designed to solve differential equations for large geometries. Finite Element Analysis (FEA) is the process by which this mathematical model is applied to a system. FEM was developed 60 years after Lord Rayleigh presented basic solutions for finding the first natural frequency of simple structures which formed the basis for modern solutions, and quickly developed into a hugely useful tool for both engineers and physicists [205].

Typical applications of FEA include structural analysis, heat transfer, fluid flow, mass transport, and electromagnetic potential, but can be applied to a huge range of problems that are described by differential equations.

A geometry comprising of different materials and unique shapes is divided up into a number of discrete sections known as elements¹ that are joined only via nodes that exist at the vertices of the elements, the complete set of elements is known as the mesh and the process by which a geometry is split up is known as a discretisation. Once a geometry has undergone an appropriate discretisation algorithm, the chosen equations are applied to each individual element and assembled to give system equations, and a macroscopic picture of the system is built. Post-processing checks can then be applied manually to

¹This forms the latter part of the name Finite Element, the former refers to the number of degrees of freedom used to model each element.

ensure results are correct, as there are a large number of variables that can derail what could be accurate results, these include poor meshing, inaccurate approximations, incorrect material parameters, etc. This describes the three primary stages, discretisation, solution analysis, and post processing of a finite element simulation.

Presented here is a detailed example of how stress and strain of a simple 1-dimensional structure can be obtained using FEA. Beginning with Hooke's law,

$$F = -kx, \quad (\text{B.1})$$

where F is the force, k is the stiffness constant, and x is the displacement. This can easily be adjusted in order to apply it to a element, F becomes f , the nodal forces, k becomes $[k]$, the stiffness matrix, and x becomes $[u]$, the nodal displacements.



Figure B.1: A single 1-dimensional element with two nodes, each with linear translational elements x and y , and a torsional translational element θ .

For a single 1-dimensional element with two nodes, 1 and 2, each with linear translational elements x and y , and a torsional translational element θ , as shown in figure B.1, equation B.1 becomes

$$\begin{bmatrix} f_{x1} \\ f_{y1} \\ m_1 \\ f_{x2} \\ f_{y2} \\ m_2 \end{bmatrix} = \begin{bmatrix} k_{11} & k_{12} & k_{13} & k_{14} & k_{15} & k_{16} \\ k_{21} & k_{22} & k_{23} & k_{24} & k_{25} & k_{26} \\ k_{31} & k_{32} & k_{33} & k_{34} & k_{35} & k_{36} \\ k_{41} & k_{42} & k_{43} & k_{44} & k_{45} & k_{46} \\ k_{51} & k_{52} & k_{53} & k_{54} & k_{55} & k_{56} \\ k_{61} & k_{62} & k_{63} & k_{64} & k_{65} & k_{66} \end{bmatrix} \begin{bmatrix} u_1 \\ v_1 \\ \theta_1 \\ u_2 \\ v_2 \\ \theta_2 \end{bmatrix}. \quad (\text{B.2})$$

The equilibrium equation governing the lateral deflection of a beam is given by [206]

$$EI \frac{d^4 w(x)}{dx^2} = q(x), \quad (\text{B.3})$$

where E is the Young's modulus, I is the area moment of inertia, $w(x)$ is the deflection of the beam, and $q(x)$ is the distributed load applied to the beam. By solving this equation the stiffness matrix can be found

$$[k] = \begin{bmatrix} \frac{AE}{L} & 0 & 0 & -\frac{AE}{L} & 0 & 0 \\ 0 & \frac{12EI}{L^3} & \frac{6EI}{L^2} & 0 & -\frac{12EI}{L^3} & \frac{6EI}{L^2} \\ 0 & \frac{6EI}{L^2} & \frac{4EI}{L} & 0 & -\frac{6EI}{L^2} & \frac{2EI}{L} \\ -\frac{AE}{L} & 0 & 0 & \frac{AE}{L} & 0 & 0 \\ 0 & -\frac{12EI}{L^3} & -\frac{6EI}{L^2} & 0 & \frac{12EI}{L^3} & \frac{6EI}{L^2} \\ 0 & \frac{6EI}{L^2} & \frac{2EI}{L} & 0 & -\frac{6EI}{L^2} & \frac{4EI}{L} \end{bmatrix}, \quad (\text{B.4})$$

where A is the cross sectional area and L is the length of the beam. This can be substituted into equation B.2 and simplified into a series of linear equations

$$\begin{aligned} f_{x1} &= \frac{AE}{L}u_1 - \frac{AE}{L}u_2, \\ f_{y1} &= \frac{12EI}{L^3}v_1 + \frac{6EI}{L^2}\theta_1 - \frac{12EI}{L^3}v_2 + \frac{6EI}{L^2}\theta_2, \\ m_1 &= \frac{6EI}{L^2}v_1 + \frac{4EI}{L}\theta_1 - \frac{6EI}{L^2}v_2 + \frac{2EI}{L}\theta_2, \\ f_{x2} &= -\frac{AE}{L}u_1 + \frac{AE}{L}u_2, \\ f_{y2} &= -\frac{12EI}{L^3}v_1 - \frac{6EI}{L^2}\theta_1 + \frac{12EI}{L^3}v_2 - \frac{6EI}{L^2}\theta_2, \\ m_2 &= \frac{6EI}{L^2}v_1 + \frac{2EI}{L}\theta_1 - \frac{6EI}{L^2}v_2 + \frac{4EI}{L}\theta_2. \end{aligned} \quad (\text{B.5})$$

It is possible to apply a linear force to node two in the x direction while all other degrees of freedom remain fixed, and are therefore equal to zero, this results in

$$\begin{aligned} f_{x1} &= 0, \\ f_{y1} &= -\frac{12EI}{L^3}v_2, \\ m_1 &= -\frac{6EI}{L^2}v_2, \\ f_{x2} &= 0, \\ f_{y2} &= \frac{12EI}{L^3}v_2, \\ m_2 &= -\frac{6EI}{L^2}v_2. \end{aligned} \quad (\text{B.6})$$

And so the forces acting on other nodes that are caused by the initial displacement can easily be calculated. From this, a simple set of equations can be applied to find stress,

strain, and displacement, first by using equation B.1 to find $[u]$, and then using equations $\epsilon = \Delta L/L_0$ and $\sigma = E\epsilon$ to find strain and stress respectively, where L_0 is the original size of the beam.



Figure B.2: Three 1-dimensional elements with a total of 4 nodes, each with linear translational elements x and y , and a torsional translational element θ .

Expanding this example into a chain of 1-dimensional elements each with 2 nodes, as in figure B.2, it is possible to form a stiffness matrix that represents the entire system, since adjacent elements share nodes there is significant overlap between the corresponding elements in the stiffness matrix, Hooke's law therefore becomes equation B.7.

With the addition of only two extra elements this equation has become unmanageable to do by hand, and so systems with huge numbers of elements need complex software to accurately analyse. Many such packages exist, one of which is FeNICS.

$$\begin{bmatrix} f_{x1} \\ f_{y1} \\ m_1 \\ f_{x2} \\ f_{y2} \\ m_2 \\ f_{x3} \\ f_{y3} \\ m_3 \\ f_{x4} \\ f_{y4} \\ m_4 \end{bmatrix} = \begin{bmatrix} \frac{A_1 E_1}{L_1} & 0 & 0 & -\frac{A_1 E_1}{L_1} & 0 & 0 \\ 0 & \frac{12 E_1 I_1}{L_1^3} & \frac{6 E_1 I_1}{L_1^2} & 0 & -\frac{12 E_1 I_1}{L_1^3} & \frac{6 E_1 I_1}{L_1^2} \\ 0 & \frac{6 E_1 I_1}{L_1^2} & \frac{4 E_1 I_1}{L_1} & 0 & -\frac{6 E_1 I_1}{L_1^2} & \frac{2 E_1 I_1}{L_1} \\ -\frac{A_1 E_1}{L_1} & 0 & 0 & \frac{A_1 E_1}{L_1} + \frac{A_2 E_2}{L_2} & 0 & 0 \\ 0 & -\frac{12 E_1 I_1}{L_1^3} & -\frac{6 E_1 I_1}{L_1^2} & 0 & \frac{12 E_1 I_1}{L_1^3} + \frac{12 E_2 I_2}{L_2^3} & -\frac{6 E_1 I_1}{L_1^2} + \frac{6 E_2 I_2}{L_2^2} \\ 0 & \frac{6 E_1 I_1}{L_1^2} & \frac{2 E_1 I_1}{L_1} & 0 & -\frac{6 E_1 I_1}{L_1^2} + \frac{6 E_2 I_2}{L_2^2} & \frac{4 E_1 I_1}{L_1} + \frac{4 E_2 I_2}{L_2} \\ 0 & 0 & 0 & -\frac{A_2 E_2}{L_2} & 0 & 0 \\ 0 & 0 & 0 & 0 & -\frac{12 E_2 I_2}{L_2^3} & -\frac{6 E_2 I_2}{L_2^2} \\ 0 & 0 & 0 & 0 & \frac{6 E_2 I_2}{L_2^2} & \frac{2 E_2 I_2}{L_2} \\ 0 & 0 & 0 & 0 & 0 & 0 \\ 0 & 0 & 0 & 0 & 0 & 0 \\ 0 & 0 & 0 & 0 & 0 & 0 \end{bmatrix} \begin{bmatrix} 0 & 0 & 0 & 0 & 0 & 0 \\ 0 & 0 & 0 & 0 & 0 & 0 \\ 0 & 0 & 0 & 0 & 0 & 0 \\ -\frac{A_2 E_2}{L_2} & 0 & 0 & 0 & 0 & 0 \\ 0 & -\frac{12 E_2 I_2}{L_2^3} & \frac{6 E_2 I_2}{L_2^2} & 0 & 0 & 0 \\ 0 & -\frac{6 E_2 I_2}{L_2^2} & \frac{2 E_2 I_2}{L_2} & 0 & 0 & 0 \\ \frac{A_2 E_2}{L_2} + \frac{A_3 E_3}{L_3} & 0 & 0 & -\frac{A_3 E_3}{L_3} & 0 & 0 \\ 0 & \frac{12 E_2 I_2}{L_2^3} + \frac{12 E_3 I_3}{L_3^3} & -\frac{6 E_2 I_2}{L_2^2} + \frac{6 E_3 I_3}{L_2^2} & 0 & -\frac{12 E_3 I_3}{L_3^3} & \frac{6 E_3 I_3}{L_2^2} \\ 0 & -\frac{6 E_2 I_2}{L_2^2} + \frac{6 E_3 I_3}{L_2^2} & \frac{4 E_2 I_2}{L_2} + \frac{4 E_3 I_3}{L_3} & 0 & -\frac{6 E_3 I_3}{L_3^2} & \frac{2 E_3 I_3}{L_3} \\ -\frac{A_3 E_3}{L_3} & 0 & 0 & \frac{A_3 E_3}{L_3} & 0 & 0 \\ 0 & -\frac{12 E_3 I_3}{L_3^3} & -\frac{6 E_3 I_3}{L_3^2} & 0 & \frac{12 E_3 I_3}{L_3^3} & -\frac{6 E_3 I_3}{L_3^2} \\ 0 & \frac{6 E_3 I_3}{L_3^2} & \frac{2 E_3 I_3}{L_3} & 0 & -\frac{6 E_3 I_3}{L_3^2} & \frac{4 E_3 I_3}{L_3} \end{bmatrix} \begin{bmatrix} u_1 \\ v_1 \\ \theta_1 \\ u_2 \\ v_2 \\ \theta_2 \\ u_3 \\ v_3 \\ \theta_3 \\ u_4 \\ v_4 \\ \theta_4 \end{bmatrix} \quad (\text{B.7})$$

Appendix C

Electromagnetic Modes in an Optical Fibre

Electromagnetic waves propagating through a spatially confined waveguide such as an optical fibre exist in modes, unvarying intensity distributions that are found by solving Maxwell's equations with appropriate boundary conditions, each solution has a field distribution, $\psi(x, y)$, and a propagation constant, β , a value characterising the change of amplitude and phase as an electromagnetic wave propagates. For an arbitrary non-magnetic dielectric medium of refractive index $n(x, y)$ with no point sources, Maxwell's equations become

$$\begin{aligned}\nabla \cdot (n^2 E) &= 0, \\ \nabla \cdot B &= 0, \\ \nabla \times E &= -\frac{\partial B}{\partial t}, \\ \nabla \times B &= \epsilon_0 n^2 \frac{\partial E}{\partial t}.\end{aligned}\tag{C.1}$$

Beginning with Gauss' equation and using the product rule $\nabla \cdot (fv) = f(\nabla \cdot v) + v \cdot (\nabla f)$

$$\nabla \cdot E = -\frac{E \cdot \nabla n^2}{n^2} = -E \cdot \nabla \ln n^2.\tag{C.2}$$

At the same time, using Faraday's Law of Induction and the vector identity $\nabla^2 f = \Delta f$ obtains

$$\nabla \times (\nabla \times E) = -\mu_0 \frac{\partial \nabla \times H}{\partial t}. \quad (\text{C.3})$$

Substituting in Ampere's Circuital Law on the right hand side to remove the magnetic field and using $\mu_0 \epsilon_0 = 1/c^2$ gives

$$\nabla(\nabla \cdot E) - \nabla^2 E = \frac{n^2}{c^2} \frac{\partial^2 E}{\partial t^2}. \quad (\text{C.4})$$

As a result of this substitution, the solution will be only in terms of electric field. Substituting equation C.2 into C.4 gives

$$\nabla^2 E - \frac{n^2}{c^2} \frac{\partial^2 E}{\partial t^2} = -\nabla(E \cdot \nabla \ln n^2). \quad (\text{C.5})$$

n does not depend on z or t , so modes are sought of the form

$$\left. \begin{matrix} E(x, y, z, t) \\ H(x, y, z, t) \end{matrix} \right\} = \left. \begin{matrix} E(x, y) \\ H(x, y) \end{matrix} \right\} e^{i(\beta z - \omega t)}, \quad (\text{C.6})$$

such that $\partial/\partial z \rightarrow i\beta$, and $\partial/\partial t \rightarrow -i\omega$, equation C.5 along with $k = \omega/c$ becomes the vector wave equation

$$\nabla_T^2 E + (K^2 n^2 - \beta^2) E = -(\nabla_T + i\beta \hat{z})(E \cdot \nabla_T \ln n^2), \quad (\text{C.7})$$

where $\nabla_T = (\partial/\partial x, \partial/\partial y, 0)$ is the transverse component of the grad operator and \hat{z} is the unit vector along z . The solutions for this equation are satisfied by eigenfunctions $E(x, y)$ with eigenvalues β , however, the right hand side makes finding these solutions difficult as the x and y components of the electric field are coupled together by the right hand side, this can be conveniently eliminated with the weak guidance approximation, $\Delta n(x, y) \ll n$, because $\nabla_T \ln n^2$ is proportional to the variation in n . The weak guidance approximation applied to the majority of optical fibres and despite its name fibres with this characteristic can guide light well. The resulting equation is the scalar wave equation

$$\nabla_T^2 \psi(x, y) \hat{e} + (K^2 n^2 - \beta^2) \psi(x, y) \hat{e} = 0, \quad (\text{C.8})$$

where $\psi(x, y)$ is the scalar field distribution, \hat{e} is a unit vector, and the propagation constant, β , varies and obeys the condition, $kn_2 \geq \beta \geq kn_1$, resulting in the constant being positive in the core and negative in the cladding. This is possible since the remaining part of the vector wave equation becomes independent of vector direction, E_x and E_y are no longer coupled. Moving into polar coordinates, separation of variables can be used to convert the scalar wave equation into radial and angular dependent ordinary differential equations

$$\psi(r, \phi) = R(r)F(\phi). \quad (\text{C.9})$$

The angular equation for $F(\phi)$, from simple harmonic motion, is

$$\frac{d^2 F}{d\phi^2} + l^2 F = 0. \quad (\text{C.10})$$

This produces two answers with sine and cosine dependencies

$$F(\phi) = \cos(l\phi), F(\phi) = \sin(l\phi), \quad (\text{C.11})$$

where $l = 0, 1, 2, \dots$ is a separation constant. The radial equation for $R(r)$ is

$$r^2 \frac{d^2 R}{dr^2} + r \frac{dR}{dr} + r^2 (k^2 n^2 - \beta^2) R - l^2 R = 0. \quad (\text{C.12})$$

This is simply the Bessel functions of order l in the core, and the solution that is finite as $r \rightarrow 0$ is

$$R(r) = A J_l \left(\frac{Ur}{a} \right), \quad (\text{C.13})$$

where $J_l(x)$ is the Bessel function of the first kind of order l . For the cladding, the radial equation is Bessel's modified equation of order l , the solution that is finite as $r \rightarrow \infty$ is

$$R(r) = BK_l \left(\frac{Wr}{a} \right), \quad (\text{C.14})$$

where $K_l(x)$ is the modified Bessel function of the second kind of order l . Bessel functions of the first kind and modified Bessel functions of the second kind are presented graphically in figure C.1.

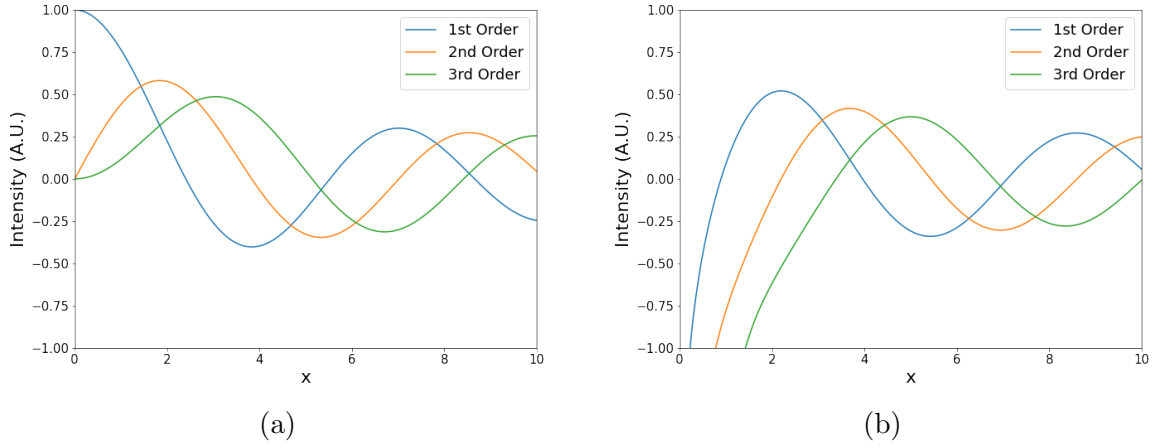


Figure C.1: First, Second, and third order (a) Bessel functions of the first kind ($J_l(x)$) and (b) Bessel functions of the second kind ($K_l(x)$). These are the solutions to the radial equation C.12 for the core and cladding respectively.

Introduced in equations C.13 and C.14 are the normalised parameters U and W , they are dimensionless values that aid in the simplification of the solutions corresponding to the core and cladding respectively. They are defined as

$$\begin{aligned} U &= a\sqrt{k^2 n_1^2 - \beta^2}, \\ W &= a\sqrt{\beta^2 - k^2 n_2^2}. \end{aligned} \quad (\text{C.15})$$

The quadratic summation of parameters U and W , $U^2 + W^2 = V^2$, leads to a third parameter, V , which is considered a normalised frequency and is colloquially known as the V-number, expressed as

$$V = ak\sqrt{n_1^2 - n_2^2}, \quad (\text{C.16})$$

where a is the radius of the fibre core, and n_1 and n_2 are the refractive indices for the core and cladding respectively. Only a single mode (eigenfunction) will be present in a fibre when $V < 2.405$, corresponding to the first zero of the Bessel function used to describe the mode, this is known as a single mode fibre and has its own unique applications when compared with multimode fibre, characterised as a fibre with $V > 2.405$. For large values of V , the number of modes in a fibre can be approximated with the equation [207]

$$N \approx \frac{V^2}{4} \quad (\text{C.17})$$

The first three modes in a multimode, step index fibre for light that is linearly polarised ($LP_{l,m}$ modes) are presented in figure C.2, each mode has two parameters, l and m that influence the shape of the mode, these correspond to how the field distribution varies with angle and radius as per equations C.11 and C.12. For modes where $l \neq 0$, two degenerate orthogonal solutions are present corresponding to the two sinusoidal solutions for equation C.11, for modes where $l = 0$, only one solution is present since $F(\phi) = \sin(0\phi) = 0$.

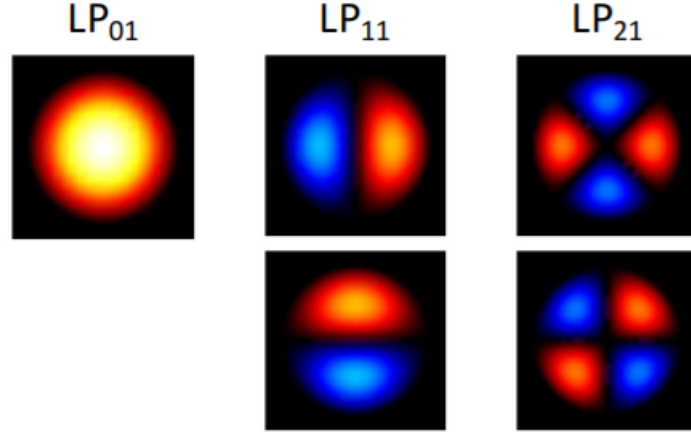


Figure C.2: The first three linear polarisation (LP) modes for a step-index fibre are presented here, including both of the two degenerate forms of modes LP_{11} and LP_{21} . Reproduced from [195].

$LP_{l,m}$ modes are not the only ones to exist in this kind of fibre, Transverse Electric and Transverse Magnetic (TE and TM) modes designate modes where there is no electric or magnetic field component in the z -direction respectively, Transverse ElectroMagnetic (TEM) designate modes without any electric nor magnetic field components in the z -

direction, and hybrid modes, where there is non-zero electric and magnetic field in the z -direction. Due to the weak guidance approximation, combinations of solutions for these various modes correspond directly to the scalar solutions for linear polarisation modes and are often presented as LP modes. A full correspondence between the first ten LP modes and the contingent TM , TE , EH , and HE modes is shown in the following table.

LP-mode designation	Mode designation and quantity	Number of degenerate modes
LP_{01}	$HE_{11} \times 2$	2
LP_{11}	$TE_{01}, TM_{01}, HE_{21} \times 2$	4
LP_{21}	$EH_{11} \times 2, HE_{31} \times 2$	4
LP_{02}	$HE_{12} \times 2$	2
LP_{31}	$EH_{21} \times 2, HE_{41} \times 2$	4
LP_{12}	$TE_{02}, TM_{02}, HE_{22} \times 2$	4
LP_{41}	$EH_{31} \times 2, HE_{51} \times 2$	4
LP_{22}	$EH_{12} \times 2, HE_{32} \times 2$	4
LP_{03}	$HE_{13} \times 2$	2
LP_{51}	$EH_{41} \times 2, HE_{61} \times 2$	4

For modes with propagation constants that fall outside of the condition $kn_2 \geq \beta \geq kn_1$, the light is no longer strictly confined to the core of the fibre. When $\beta < kN_2$, the associated mode is a ‘cladding mode’, which occurs due to refraction from the core and propagates in the cladding [208].

C.1 Loss

Optical fibres are far from perfect and exhibit various types of loss as light moves through them, some such loss mechanisms are bend loss, insertion loss, and attenuation.

As light moves through a curved fibre with radii of curvature on the order of 1cm, light will pass through the cladding and leak out of the core due to the change in angle of

incidence at the core-cladding interface.

Insertion loss comes when light in free space is focussed into a fibre, if there is not a complete overlap between the field distribution in free space and the superposition of modes within a fibre then some of the light will not enter the fibre and instead, this also applies to when light leaves one fibre to enter another (i.e. splicing).

Finally, attenuation occurs due to absorption and scattering processes as light propagates through the fibre and is highly dependent on wavelength. At wavelengths below 1350nm the main contributor to attenuation is Rayleigh scattering, which effects lower wavelengths far more readily than higher ones and the rate of which is inversely proportional to wavelength to the fourth power, a large spike then occurs around 1400nm corresponding to absorption due to O-H (water) bonds in the fibre, there is then a brief dip at 1550nm before a large increase in attenuation due to absorption by Si-O bonds in the material. This is summarised in figure C.3. As a result, long distance telecommunications that use fibre in their operation use wavelengths around 1550nm, since light is able to travel significantly further without attenuating.

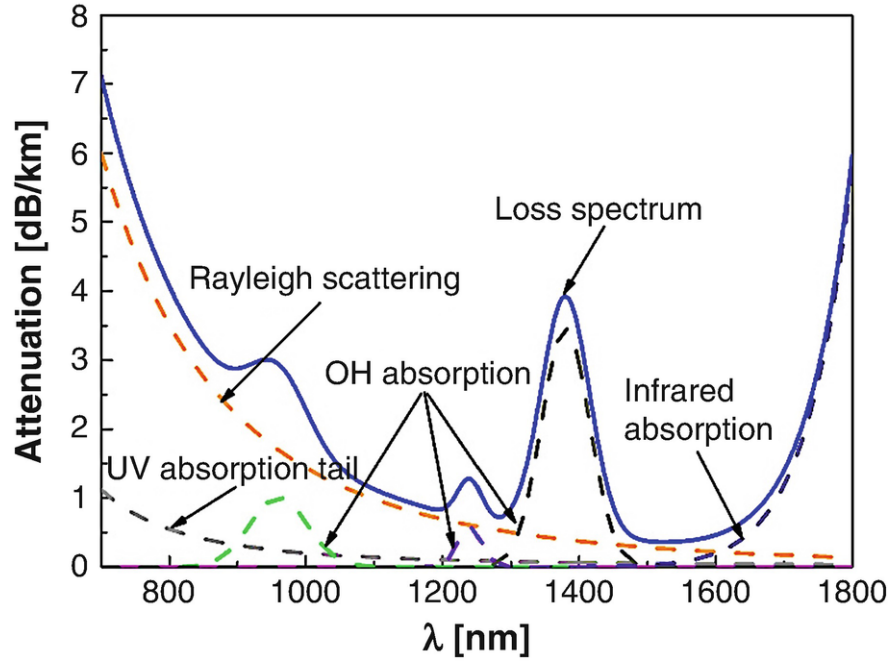


Figure C.3: Graph showing the attenuation in a fibre as a function of wavelength, there are various intrinsic properties of silica that result in the attenuation of light. There is a natural dip at 1550nm and so long distance fibre communications operate at this wavelength. Reproduced from [209].

C.2 Mode Development in Transition Regions

As a result of the large change in diameter, various properties of the fibre undergo dramatic changes. As light passes through the transition region of the taper, loss occurs due to the field distribution being unable to change rapidly enough to keep up with the changing field distribution which has a dependency on the fibre diameter, light will enter higher order and cladding modes as a result. Loss is a function of taper angle and a transition with a suitably low loss is considered adiabatic.

There are two criteria for determining whether or not a transition is adiabatic or not, the length scale criterion and the weak power transfer criterion, both derived by Love *et al* [210]. Modelling the transition as a right circular cone with height (transition length) z_t and an apex angle (taper angle) $\Omega(z) = \arctan |d\rho/da|$ where z is the distance along the taper and $a = a(z)$. Since $\Omega(z) \gg 1$, then

$$z_t \approx \frac{a}{\Omega}. \quad (\text{C.18})$$

The local coupling length between the fundamental and second order modes is taken to be

$$z_b = \frac{2\pi}{\beta_1 - \beta_2}, \quad (\text{C.19})$$

where β_1 and β_2 both have a dependency on z . It is therefore intuitive that negligible coupling between the two modes occurs when $z_t \gg z_b$ and the fundamental mode will propagate adiabatically through the transition, and complete coupling between the two modes will occur when $z_t \ll z_b$. The condition $z_t = z_b$ will then give an approximate boundary between adiabatic and lossy transitions, this is equivalent to the following equation and concludes the derivation of the length scale criterion.

$$\Omega = \frac{a(\beta_1 - \beta_2)}{2\pi}. \quad (\text{C.20})$$

Next is the weak power transfer criterion, which is derived by expressing the field along the taper as a superposition of the fundamental and cladding local modes and then formally solving a set of coupled local mode equations which relate the amplitude of each mode, thereby quantifying the loss from the fundamental mode due to tapering. Assuming small loss and a transfer of power from the fundamental to the mode with the most similar propagation constant, then the coupled equations have analytical solutions and the amplitudes of these two modes have approximate solutions

$$a_1(z) = a_1(0) \exp\left\{i \int_0^z \beta_1(z') dz'\right\}, \quad (\text{C.21})$$

$$a_2(z) = a_1(0) \exp\left\{i \int_0^z \beta_2(z') dz'\right\} \times \int_0^z C(z') \exp\left\{i \int_0^{z'} (\beta_1(z'') - \beta_2(z'')) dz''\right\} dz', \quad (\text{C.22})$$

where a_1 and a_2 are the amplitudes of the two modes, and C is the coupling coefficient between two modes, given by

$$C = \frac{1}{2} \frac{k}{\beta_1 - \beta_2} \frac{d\rho}{dz} \frac{1}{n_{co}} \frac{\int_{A_\infty} \psi_1 \psi_2 \frac{\partial n^2}{\partial \rho} dA}{\left(\int_{A_\infty} \psi_1^2 dA \int_{A_\infty} \psi_2^2 dA \right)^{1/2}}, \quad (\text{C.23})$$

where n_{co} is the maximum core index, A_∞ is the infinite cross section, and ϕ_1, ϕ_2 are the scalar field distributions for the two modes. It can be reasoned that the power transfer between modes is small when the final term of equation C.22 is significantly less than one when $z = L$, the end of the transition region. The exponential in this equation causes the integral to oscillate in phase, and so if the taper is slowly varying the maximum power transfer occurs after half a beat length ($\pi/\beta_1 - \beta_2$). The integrand and the coupling coefficient are approximately constant over these small length scales, and so the inequality reduces to $C_{zb}/\pi \ll 1$ where the fraction of power lost from the fundamental is given by the square of the left hand side. Assuming that $C_{zb} = 1$, the loss becomes $1/\pi^2$, or approximately 10% per half beat length.

This criterion is more accurate as it includes the field distributions of both modes, a detail that is omitted in the length scale criterion, but is unfortunately harder to implement for the same reason.

Bibliography

- [1] ITL Education Solutions Limited. Introduction to Computer Science, 2011.
- [2] Vimal Mehta. *Logic Gates for Beginners*. 2015.
- [3] Hassan Mujtaba. AMD EPYC Rome CPUs Feature 39.54 Billion Transistors, IOD Detailed, 2019.
- [4] David P. Anderson. Biographies: Tom Kilburn: A Pioneer of Computer Design. *IEEE Annals of the History of Computing*, 31(2):82–86, jun 2009.
- [5] Karl Rupp. The Economic Limit to Moore’s Law, 2011.
- [6] John Shalf. The future of computing beyond Moore’s Law, mar 2020.
- [7] R. Mark Stevenson, Andrew J. Hudson, Anthony J. Bennett, Robert J. Young, Christine A. Nicoll, David A. Ritchie, and Andrew J. Shields. Evolution of entanglement between distinguishable light states. *Physical Review Letters*, 101(17):170501, oct 2008.
- [8] Massimo Blasone, Fabio Dell’anno, Silvio De Siena, and Fabrizio Illuminati. Entanglement in neutrino oscillations. 2009.
- [9] Yiheng Lin, David R. Leibbrandt, Dietrich Leibfried, and Chin wen Chou. Quantum entanglement between an atom and a molecule. *Nature* 2020 581:7808, 581(7808):273–277, may 2020.
- [10] Tanjung Krisnanda, Chiara Marletto, Vlatko Vedral, Mauro Paternostro, and Tomasz Paterek. Probing quantum features of photosynthetic organisms. *npj Quantum Information*, 4(1), nov 2017.

- [11] Shlomi Kotler, Gabriel A. Peterson, Ezad Shojaei, Florent Lecocq, Katarina Cicak, Alex Kwiatkowski, Shawn Geller, Scott Glancy, Emanuel Knill, Raymond W. Simmonds, José Aumentado, and John D. Teufel. Direct observation of deterministic macroscopic entanglement. *Science*, 372(6542):622–625, may 2021.
- [12] Michael A. Nielsen. Cluster-state quantum computation. *Reports on Mathematical Physics*, 57(1):147–161, apr 2005.
- [13] E Bagan, M A Ballester, R D Gill, A Monras, and R Muñoz-Tapia. Optimal full estimation of qubit mixed states.
- [14] Colin P. Williams. Explorations in quantum computing. 2011.
- [15] Adriano Barenco, Charles H. Bennett, Richard Cleve, David P. Divincenzo, Norman Margolus, Peter Shor, Tycho Sleator, John A. Smolin, and Harald Weinfurter. Elementary gates for quantum computation. *Physical Review A*, 52(5):3457, nov 1995.
- [16] M.A. Nielsen and I.L. Chuang. *Quantum Computation and Quantum Information*, volume 52. 2011.
- [17] Richard P Feynman. Quantum Mechanical Computers 1. *Foundations of Physics*, 16(6), 1986.
- [18] Dorit Aharonov. A Simple Proof that Toffoli and Hadamard are Quantum Universal. 2003.
- [19] John Preskill. Quantum Computing and the Entanglement Frontier. 2012.
- [20] Peter W Shor. Algorithms for Quantum Computation: Discrete Logarithms and Factoring. Technical report, 1994.
- [21] H D Zeh. On the Interpretation of Measurement in Quantum Theory. *Foundations of Physics*, 1(1), 1970.
- [22] Maximilian Schlosshauer. Quantum decoherence. *Physics Reports*, 831:1–57, oct 2019.

- [23] T Pellizzari, S A Gardiner, J I Cirac, and P Zoller. Decoherence, Continuous Observation, and Quantum Computing: A Cavity QED Model. 75, 1995.
- [24] Alon Orlitsky. Information Theory. *Encyclopedia of Physical Science and Technology*, pages 751–769, jan 2003.
- [25] J A Schreier, A A Houck, Jens Koch, D I Schuster, B R Johnson, J M Chow, J M Gambetta, J Majer, L Frunzio, M H Devoret, S M Girvin, and R J Schoelkopf. Suppressing Charge Noise Decoherence in Superconducting Charge Qubits. 2007.
- [26] I Chiorescu, Y Nakamura, C J P M Harmans, and J E Mooij. Coherent Quantum Dynamics of a Superconducting Flux Qubit. 2003.
- [27] John M Martinis. Superconducting phase qubits. 8:81–103, 2009.
- [28] Leon N. Cooper. Bound Electron Pairs in a Degenerate Fermi Gas. *Physical Review*, 104(4):1189, nov 1956.
- [29] B. D. Josephson. Possible new effects in superconductive tunnelling. *Physics Letters*, 1(7):251–253, jul 1962.
- [30] Frank Arute, Kunal Arya, Ryan Babbush, Dave Bacon, Joseph C Bardin, Rami Barends, Rupak Biswas, Sergio Boixo, Fernando G S L Brandao, David A Buell, Brian Burkett, Yu Chen, Zijun Chen, Ben Chiaro, Roberto Collins, William Courtney, Andrew Dunsworth, Edward Farhi, Brooks Foxen, Austin Fowler, Craig Gidney, Marissa Giustina, Rob Graff, Keith Guerin, Steve Habegger, Matthew P Harrigan, Michael J Hartmann, Alan Ho, Markus Hoffmann, Trent Huang, Travis S Humble, Sergei V Isakov, Evan Jeffrey, Zhang Jiang, Dvir Kafri, Kostyantyn Kechedzhi, Julian Kelly, Paul V Klimov, Sergey Knysh, Alexander Korotkov, Fedor Kostritsa, David Landhuis, Mike Lindmark, Erik Lucero, Dmitry Lyakh, Salvatore Mandrà, Jarrod R McClean, Matthew McEwen, Anthony Megrant, Xiao Mi, Kristel Michielsen, Masoud Mohseni, Josh Mutus, Ofer Naaman, Matthew Neeley, Charles Neill, Murphy Yuezhen Niu, Eric Ostby, Andre Petukhov, John C Platt, Chris Quintana, Eleanor G Rieffel, Pedram Roushan, Nicholas C Rubin, Daniel Sank,

- Kevin J Satzinger, Vadim Smelyanskiy, Kevin J Sung, Matthew D Trevithick, Amit Vainsencher, Benjamin Villalonga, Theodore White, Z Jamie Yao, Ping Yeh, Adam Zalcman, Hartmut Neven, and John M Martinis. Quantum supremacy using a programmable superconducting processor. *Nature* —, 574:505, 2019.
- [31] Kentaro Tamura and Yutaka Shikano. Quantum Random Number Generation with the Superconducting Quantum Computer IBM 20Q Tokyo. 2020.
- [32] Intel. Reinventing Data Processing with Quantum Computing. Technical Report 1, jan 2019.
- [33] H Häffner, C F Roos, and R Blatt. Quantum computing with trapped ions. *Physics Reports*, 469:155–203, 2008.
- [34] Hiroki Takahashi, Ezra Kassa, Costas Christoforou, and Matthias Keller. Strong Coupling of a Single Ion to an Optical Cavity. *Physical Review Letters*, 124, 2020.
- [35] I Pogorelov, T Feldker, Ch D Marciniak, L Postler, G Jacob, O Krieglsteiner, V Podlesnic, M Meth, V Negnevitsky, M Stadler, B Höfer, C Wächter, K Lakhmanskiy, R Blatt, P Schindler, and T Monz. Compact Ion-Trap Quantum Computing Demonstrator. *Physical Review Applied*, 10:20343, 2021.
- [36] Lieven M K Vandersypen, Matthias Steffen, Gregory Breyta, Costantino S Yannoni, Mark H Sherwood, and Isaac L Chuang. Experimental realization of Shor’s quantum factoring algorithm using nuclear magnetic resonance. 2001.
- [37] Nico W. Hendrickx and Menno Veldhorst. An array of four germanium qubits. *Nature*, may 2021.
- [38] Davide Castelvechi. Welcome anyons! Physicists find best evidence yet for long-sought 2D structures. *Nature*, 583(7815):176–177, jul 2020.
- [39] Yao Shen, Chuan Wang, and Gui Lu Long. Decoherence-free subspaces of anyon states. *Physica A: Statistical Mechanics and its Applications*, 390(23-24):4713–4718, nov 2011.

- [40] James Nakamura, Shuang Liang, Geoffrey C. Gardner, and Michael J. Manfra. Direct observation of anyonic braiding statistics at the $\nu=1/3$ fractional quantum Hall state. (1), 2020.
- [41] Pieter Kok, W J Munro, Kae Nemoto, T C Ralph, Jonathan P Dowling, and G J Milburn. Linear optical quantum computing. 2006.
- [42] Michihisa Yamamoto, Shintaro Takada, Christopher Bäuerle, Kenta Watanabe, Andreas D. Wieck, and Seigo Tarucha. Electrical control of a solid-state flying qubit. *Nature Nanotechnology*, 7(4):247–251, 2012.
- [43] E. Knill, R. Laflamme, and G. J. Milburn. A scheme for efficient quantum computation with linear optics. *Nature 2001 409:6816*, 409(6816):46–52, jan 2001.
- [44] Fulvio Flamini, Nicolo Spagnolo, and Fabio Sciarrino. Photonic quantum information processing: A review. *Reports on Progress in Physics*, 82(1), 2019.
- [45] Frédéric Bouchard, Alicia Sit, Yingwen Zhang, Robert Fickler, Filippo M. Miatto, Yuan Yao, Fabio Sciarrino, and Ebrahim Karimi. Two-photon interference: the Hong–Ou–Mandel effect. *Reports on Progress in Physics*, 84(1):012402, dec 2020.
- [46] Agata M Branczyk. Hong-Ou-Mandel Interference. 2017.
- [47] Michał Jachura and Radosław Chrapkiewicz. Shot-by-shot imaging of Hong-Ou-Mandel interference with an intensified sCMOS camera. *Optics Letters*, 40(7):1540, feb 2015.
- [48] C. K. Hong, Z. Y. Ou, and L. Mandel. Measurement of subpicosecond time intervals between two photons by interference. *Physical Review Letters*, 59(18):2044, nov 1987.
- [49] Daniel Gottesman and Isaac L. Chuang. Demonstrating the viability of universal quantum computation using teleportation and single-qubit operations. *Nature 1999 402:6760*, 402(6760):390–393, nov 1999.

- [50] T B Pittman, B C Jacobs, and J D Franson. Probabilistic quantum logic operations using polarizing beam splitters. *Physical Review A*, 64(6):062311, nov 2001.
- [51] Charles H. Bennett, Gilles Brassard, Claude Crépeau, Richard Jozsa, Asher Peres, and William K. Wootters. Teleporting an unknown quantum state via dual classical and Einstein-Podolsky-Rosen channels. *Physical Review Letters*, 70(13):1895, mar 1993.
- [52] Dik Bouwmeester, Jian Wei Pan, Klaus Mattle, Manfred Eibl, Harald Weinfurter, and Anton Zeilinger. Experimental quantum teleportation. *Nature*, 390(6660):575–579, 1997.
- [53] M. J. Collins, C. Xiong, I. H. Rey, T. D. Vo, J. He, S. Shahnian, C. Reardon, T. F. Krauss, M. J. Steel, A. S. Clark, and B. J. Eggleton. Integrated spatial multiplexing of heralded single-photon sources. *Nature Communications* 2013 4:1, 4(1):1–7, oct 2013.
- [54] C. Xiong, X. Zhang, Z. Liu, M. J. Collins, A. Mahendra, L. G. Helt, M. J. Steel, D. Y. Choi, C. J. Chae, P. H.W. Leong, and B. J. Eggleton. Active temporal multiplexing of indistinguishable heralded single photons. *Nature Communications* 2016 7:1, 7(1):1–6, mar 2016.
- [55] Moran Chen, Nicolas C. Menicucci, and Olivier Pfister. Experimental realization of multipartite entanglement of 60 modes of a quantum optical frequency comb. *Physical Review Letters*, 112(12):120505, dec 2013.
- [56] Michael A Nielsen. CLUSTER-STATE QUANTUM COMPUTATION. 2005.
- [57] Shaowei Li, Anthony D. Castellano, Shiyu Wang, Yulin Wu, Ming Gong, Zhiguang Yan, Hao Rong, Hui Deng, Chen Zha, Cheng Guo, Lihua Sun, Chengzhi Peng, Xiaobo Zhu, and Jian Wei Pan. Realisation of high-fidelity nonadiabatic CZ gates with superconducting qubits. *npj Quantum Information* 2019 5:1, 5(1):1–7, oct 2019.

- [58] C Simon, M Afzelius, J Appel, A Boyer De La Giroday, S J Dewhurst, N Gisin, C Y Hu, F Jelezko, S Kröll, J H Müller, J Nunn, E S Polzik, J G Rarity, H De Riedmatten, W Rosenfeld, A J Shields, N Sköld, R M Stevenson, R Thew, I A Walmsley, M C Weber, H Weinfurter, J Wrachtrup, and R J Young. Quantum memories A review based on the European integrated project "Qubit Applications (QAP)". *Eur. Phys. J. D*, 58:1–22, 2010.
- [59] Axel Kuhn, Markus Hennrich, and Gerhard Rempe. A Deterministic Single-Photon Source for Distributed Quantum Networking. 2002.
- [60] Valerio Scarani, Helle Bechmann-Pasquinucci, Nicolas J Cerf, Miloslav Dušek, Norbert Lütkenhaus, and Momtchil Peev. The Security of Practical Quantum Key Distribution. 2009.
- [61] Koji Azuma, Kiyoshi Tamaki, and Hoi-Kwong Lo. ARTICLE All-photonic quantum repeaters. *Nature Communications*, 2015.
- [62] Jian-Wei Pan, Dik Bouwmeester, Harald Weinfurter, and Anton Zeilinger. Experimental Entanglement Swapping: Entangling Photons That Never Interacted. *PHYSICAL REVIEW LETTERS*, 80, 1998.
- [63] Rui-Bo Jin, Masahiro Takeoka, Utako Takagi, Ryosuke Shimizu, and Masahide Sasaki. Highly efficient entanglement swapping and teleportation at telecom wavelength. 2015.
- [64] C Simon, M Afzelius, J Appel, A Boyer De La Giroday, S J Dewhurst, N Gisin, C Y Hu, F Jelezko, S Kröll, J H Müller, J Nunn, E S Polzik, J G Rarity, H De Riedmatten, W Rosenfeld, A J Shields, N Sköld, R M Stevenson, R Thew, I A Walmsley, M C Weber, H Weinfurter, J Wrachtrup, and R J Young. Quantum memories A review based on the European integrated project "Qubit Applications (QAP)". *Eur. Phys. J. D*, 58:1–22, 2010.

- [65] Nicolas Sangouard, Christoph Simon, Hugues De Riedmatten, and Nicolas Gisin. Quantum repeaters based on atomic ensembles and linear optics. *Reviews of Modern Physics*, 83(1):33–80, 2011.
- [66] Khabat Heshami, Duncan G England, Peter C Humphreys, Philip J Bustard, Victor M Acosta, Joshua Nunn, and Benjamin J Sussman. Quantum memories: emerging applications and recent advances. *Journal of Modern Optics*, 63(20):2005–2028, 2016.
- [67] Duncan G England, Kent A G Fisher, Jean-Philippe W Maclean, Philip J Bustard, Rune Lausten, Kevin J Resch, and Benjamin J Sussman. Storage and Retrieval of THz-Bandwidth Single Photons Using a Room-Temperature Diamond Quantum Memory. 2015.
- [68] M R Sprague, P S Michelberger, T F M Champion, D G England, J Nunn, X-m Jin, W S Kolthammer, A Abdolvand, P J St Russell, and I A Walmsley. Broad-band single-photon-level memory in a hollow-core photonic crystal fibre. *NATURE PHOTONICS* —, 8, 2014.
- [69] K. C. Lee, B. J. Sussman, M. R. Sprague, P. Michelberger, K. F. Reim, J. Nunn, N. K. Langford, P. J. Bustard, D. Jaksch, and I. A. Walmsley. Macroscopic non-classical states and terahertz quantum processing in room-temperature diamond. *Nature Photonics* 2011 6:1, 6(1):41–44, dec 2011.
- [70] K. C. Lee, M. R. Sprague, B. J. Sussman, J. Nunn, N. K. Langford, X. M. Jin, T. Champion, P. Michelberger, K. F. Reim, D. England, D. Jaksch, and I. A. Walmsley. Entangling macroscopic diamonds at room temperature. *Science (New York, N.Y.)*, 334(6060):1253–1256, dec 2011.
- [71] Kent A G Fisher, Duncan G England, Jean-Philippe W Maclean, Philip J Bustard, Kevin J Resch, and Benjamin J Sussman. Quantum optical signal processing in diamond. 2018.

- [72] Jun ichi Yoshikawa, Kenzo Makino, Shintaro Kurata, Peter van Loock, and Akira Furusawa. Creation, storage, and on-demand release of optical quantum states with a negative wigner function. *Physical Review X*, 3(4):041028, dec 2014.
- [73] Feihu Xu, Fumihiro Kaneda, Joseph Chapman, and Paul G. Kwiat. Quantum-memory-assisted multi-photon generation for efficient quantum information processing. *Optica, Vol. 4, Issue 9, pp. 1034-1037*, 4(9):1034–1037, sep 2017.
- [74] M. Hosseini, B. M. Sparkes, G. Campbell, P. K. Lam, and B. C. Buchler. High efficiency coherent optical memory with warm rubidium vapour. *Nature Communications 2011 2:1*, 2(1):1–5, feb 2011.
- [75] Y.-W. Cho, G. T. Campbell, J. L. Everett, J. Bernu, D. B. Higginbottom, M. T. Cao, J. Geng, N. P. Robins, P. K. Lam, and B. C. Buchler. Highly efficient optical quantum memory with long coherence time in cold atoms. *Optica*, 3(1):100, jan 2016.
- [76] J P Marangos. Topical review Electromagnetically induced transparency. 1997.
- [77] Lijun Ma, Oliver Slattery, and Xiao Tang. Optical quantum memory based on electromagnetically induced transparency. *Journal of Optics (United Kingdom)*, 19(4), 2017.
- [78] Georg Heinze, Christian Hubrich, and Thomas Halfmann. Stopped Light and Image Storage by Electromagnetically Induced Transparency up to the Regime of One Minute. 2013.
- [79] A I Lvovsky, B C Sanders, and W Tittel. Optical quantum memory. 2010.
- [80] Manjin Zhong, Morgan P. Hedges, Rose L. Ahlefeldt, John G. Bartholomew, Sarah E. Beavan, Sven M. Wittig, Jevon J. Longdell, and Matthew J. Sellars. Optically addressable nuclear spins in a solid with a six-hour coherence time. *Nature 2015 517:7533*, 517(7533):177–180, jan 2015.

- [81] Ziteng Wang, David L Kaplan, and Tara Murphy. Optical quantum memory based on electromagnetically induced transparency as a Highly Polarized Transient Point Source with the Australian SKA Pathfinder. 2017.
- [82] L. Chen, E. Hall, L. Theogarajan, and J. Bowers. Photonic switching for data center applications. *IEEE Photonics Journal*, 3(5):834–844, 2011.
- [83] Guillermo Muñoz-Matutano, Mattias Johnsson, Juan Martínez-Pastor, David Rivas Góngora, Luca Seravalli, Giovanna Trevisi, Paola Frigeri, Thomas Volz, and Massimo Gurioli. All optical switching of a single photon stream by excitonic depletion. *Communications Physics 2020 3:1*, 3(1):1–9, jan 2020.
- [84] Yishen Huang. *Silicon photonic switching: from building block design to intelligent control*. PhD thesis, 2020.
- [85] David A.B. Miller. Device requirements for optical interconnects to silicon chips. *Proceedings of the IEEE*, 97(7):1166–1185, 2009.
- [86] Cisco. Cisco Annual Internet Report (2018–2023). 2018.
- [87] Benjamin G. Lee and Nicolas Dupuis. Silicon Photonic Switch Fabrics: Technology and Architecture. *Journal of Lightwave Technology*, Vol. 37, Issue 1, pp. 6-20, 37(1):6–20, jan 2019.
- [88] K Jain and G W Pratt. Optical transistor. 2008.
- [89] Anton V. Zasedatelev, Anton V. Baranikov, Denis Sannikov, Darius Urbonas, Fabio Scafrimuto, Vladislav Yu Shishkov, Evgeny S. Andrianov, Yurii E. Lozovik, Ullrich Scherf, Thilo Stöferle, Rainer F. Mahrt, and Pavlos G. Lagoudakis. Single-photon nonlinearity at room temperature. *Nature 2021 597:7877*, 597(7877):493–497, sep 2021.
- [90] Yong Zhang, Ruihuan Zhang, Qingming Zhu, Yuan Yuan, Yikai Su, and Senior Member. Architecture and Devices for Silicon Photonic Switching in Wavelength, Polarization and Mode. *JOURNAL OF LIGHTWAVE TECHNOLOGY*, 38(2), 2020.

- [91] Li Fan, S. Gloeckner, P.D. Dobbela, S. Patra, D. Reiley, C. King, T. Yeh, J. Gritters, S. Gutierrez, Y. Loke, M. Harburn, R. Chen, E. Kruglick, M. Wu, and A. Husain. Digital MEMS switch for planar photonic crossconnects, 2002.
- [92] J. Kim, C. J. Nuzman, B. Kumar, D. F. Lieuwen, J. S. Kraus, A. Weiss, C. P. Lichtenwalner, A. R. Papazian, R. E. Frahm, N. R. Basavanahally, D. A. Ramsey, V. A. Aksyuk, F. Pardo, M. E. Simon, V. Lifton, H. B. Chan, M. Haueis, A. Gasparyan, H. R. Shea, S. Arney, C. A. Bolle, P. R. Kolodner, R. Ryf, D. T. Neilson, and J. V. Gates. 1100×1100 port MEMS-based optical crossconnect with 4-dB maximum loss. *IEEE Photonics Technology Letters*, 15(11):1537–1539, nov 2003.
- [93] D. Heiss, E. A. J. M. Bente, J. J. G. M. van der Tol, K. Ławniczuk, K. A. Williams, M. K. Smit, X. J. M. Leijtens, and Y. Jiao. InP photonic circuits using generic integration. *Photonics Research*, Vol. 3, Issue 5, pp. B60-B68, 3(5):B60–B68, oct 2015.
- [94] Shinsuke Tanaka, Seok Hwan Jeong, Susumu Yamazaki, Ayahito Uetake, Shuichi Tomabechi, Mitsuru Ekawa, and Ken Morito. Monolithically integrated 8:1 SOA gate switch with large extinction ratio and wide input power dynamic range. *IEEE Journal of Quantum Electronics*, 45(9):1155–1162, 2009.
- [95] Qixiang Cheng, Sébastien Rumley, Meisam Bahadori, and Keren Bergman. Photonic switching in high performance datacenters. *Optics Express*, 26(12):16022, 2018.
- [96] Vlatko Vedral. Introduction to quantum information science. page 183, 2006.
- [97] K. Hamamoto, T. Anan, K. Komatsu, M. Sugimoto, and I. Mito. First 8×8 semiconductor optical matrix switches using GaAs/AlGaAs electro-optic guided-wave directional couplers. *Electronics Letters*, 28(5):441–443, 1992.
- [98] K. Shimizu, S. Asakawa, D. Suehiro, Y. Matsushima, H. Ishikawa, and K. Utaka. Device Design of Silicon 2×2 Mach-Zehnder-Type Optical Switch For Polarization-

- Independent Operation. *Advanced Photonics 2017 (IPR, NOMA, Sensors, Networks, SPCom, PS) (2017), paper PTh1D.5*, Part F57-P:PTh1D.5, jul 2017.
- [99] Adrian Wonfor, Ian H. White, Qixiang Cheng, and Richard V. Penty. Scalable, Low-Energy Hybrid Photonic Space Switch. *Journal of Lightwave Technology*, Vol. 31, Issue 18, pp. 3077-3084, 31(18):3077–3084, sep 2013.
- [100] A. Wonfor, I. H. White, J. L. Wei, Q. Cheng, and R. V. Penty. Monolithic MZI-SOA hybrid switch for low-power and low-penalty operation. *Optics Letters*, Vol. 39, Issue 6, pp. 1449-1452, 39(6):1449–1452, mar 2014.
- [101] Ken Tanizawa, Keiji Suzuki, Munehiro Toyama, Minoru Ohtsuka, Nobuyuki Yokoyama, Kazuyuki Matsumaro, Miyoshi Seki, Keiji Koshino, Toshio Sugaya, Satoshi Suda, Guangwei Cong, Toshio Kimura, Kazuhiro Ikeda, Shu Namiki, Hitoshi Kawashima, J Kurumida, K Ishii, A Takefusa, Y Tanimura, S Yanagimachi, H Takeshita, A Tajima, K Fukuchi, H Honma, W Odashima, H Onaka, K Tanizawa, K Suzuki, S Suda, K Ikeda, H Kawashima, H Uetsuka, H Matsuura, H Kuwatsuka, K Sato, T Kudoh, S Namiki, H Kim, M Ohno, T Chiba, H Tadokoro, M Yanagihara, Y Igarashi, M Masahara, A Himeno, M Okuno, H Takahashi, K Hattori, h Jeong, D Shimura, T Simoyama, M Seki, N Yokoyama, M Ohtsuka, K Koshino, T Horikawa, Y Tanaka, and K Morito. Monolithic InP strictly non-blocking 8×8 switch for high-speed WDM optical interconnection. *OSA Technical Digest*, 20(17):30163–30174, 2012.
- [102] Wei Jia, Rajesh Menon, and Berardi Sensale-Rodriguez. Unique prospects of phase change material Sb₂Se₃ for ultra-compact reconfigurable nanophotonic devices. *Optical Materials Express*, 11(9), 2021.
- [103] Gaurav Kumar Bharti and Jayanta Kumar Rakshit. Design of all-optical logical mode-switching using micro-ring resonator. *Optical Engineering*, 60(03):1–15, 2021.
- [104] J.K. Rakshit, T. Chattopadhyay, and J.N. Roy. Design of ring resonator based all optical switch for logic and arithmetic operations – A theoretical study — Elsevier Enhanced Reader. *Optik*, 2013.

- [105] Nicolás Sherwood-Droz, Howard Wang, Long Chen, Benjamin G. Lee, Aleksandr Biberman, Keren Bergman, and Michal Lipson. Optical 4x4 hitless silicon router for optical networks-on-chip (NoC). *Optics Express*, 16(20):15915, sep 2008.
- [106] Ming C. Wu, Niels Quack, Richard S. Muller, Sangyoon Han, and Tae Joon Seok. Highly Scalable Digital Silicon Photonic MEMS Switches. *Journal of Lightwave Technology*, Vol. 34, Issue 2, pp. 365-371, 34(2):365–371, jan 2016.
- [107] Yi Sun and Daoxin Dai. New concept of silicon photonic MEMS switch based on total internal reflection. *Asia Communications and Photonics Conference/International Conference on Information Photonics and Optical Communications 2020 (ACP/IPOC) (2020)*, paper T1D.4, page T1D.4, oct 2020.
- [108] F. Kaneda and P. G. Kwiat. High-efficiency single-photon generation via large-scale active time multiplexing. *Science Advances*, 5(10):1–7, 2019.
- [109] Connor Kupchak, Jennifer Erskine, Duncan England, and Benjamin Sussman. Terahertz-bandwidth switching of heralded single photons. *Optics Letters*, 44(6):1427, 2019.
- [110] Carlo Alexander Scott Page. Atomic Switchable Cavity Quantum Memory Through Induced Two Photon Dispersion. 2021.
- [111] MOGLabs. External Cavity Diode Laser Manual. *Construction Specifier*, 57(12):22, 2018.
- [112] MOGLabs. External Cavity Diode Laser Controller Manual. 31(2), 2017.
- [113] MOGLabs. *MWM wavemeter Manual*. 2021.
- [114] F.J. Duarte. Tunable Lasers Handbook. *Tunable Lasers Handbook*, 1995.
- [115] Gerhard Kloos. Applications of lock-in amplifiers in optics. page 118, 2018.
- [116] E A Donley, T P Heavner, F Levi, M O Tataw, and S R Jefferts. Double-pass acousto-optic modulator system. 2005.

- [117] Liquid Intruments. *Moku:Lab Specifications*. 2021.
- [118] John S Townsend. *A Modern Approach To Quantum Mechanics*. 2000.
- [119] Daniel A Steck. Rubidium 87 D Line Data. 2001.
- [120] Daniel Steck. Rubidium 85 D Line Data. 2008.
- [121] Shigeru Nakayama. Theoretical Analysis of Rb and Cs D2 Lines in Saturation Spectroscopy with Optical Pumping. *Japanese Journal of Applied Physics*, 23(Part 1, No. 7):879–883, jul 1984.
- [122] Eric J Heller, Robert L Sundberg, and David Tanner¹. Simple Aspects of Raman Scattering. *J. Phys. Chem*, 86:1822–1833, 1982.
- [123] Thomas H. Kauffmann, Ninel Kokanyan, and Marc D. Fontana. Use of Stokes and anti-Stokes Raman scattering for new applications. *Journal of Raman Spectroscopy*, 50(3):418–424, mar 2019.
- [124] Marcel Fajkus, Jan Nedoma, Pavel Mec, Eva Hrubesova, Radek Martinek, and Vladimir Vasinek. Analysis of the highway tunnels monitoring using an optical fiber implemented into primary lining. *Journal of Electrical Engineering*, 68(5):364–370, sep 2017.
- [125] Charles. Kittel. *Introduction to solid state physics*. Wiley, 2005.
- [126] Adrian Bejan and Allan D. Kraus. *Heat Transfer Handbook*. 2003.
- [127] Jaffar Emad Kadum, Cheng Feng, and Thomas Schneider. Characterization of the Noise Induced by Stimulated Brillouin Scattering in Distributed Sensing. *Sensors (Basel, Switzerland)*, 20(15):1–15, aug 2020.
- [128] D. A. Kleinman. Theory of Second Harmonic Generation of Light. *Physical Review*, 128(4):1761, nov 1962.
- [129] Stephen J. Brosnan and Robert L. Byer. Optical Parametric Oscillator Threshold and Linewidth Studies. *IEEE Journal of Quantum Electronics*, 15(6):415–431, 1979.

- [130] Rüdiger Paschotta. Field Guide to Lasers. *Field Guide to Lasers*, sep 2009.
- [131] Elsa Garmire. Stimulated Brillouin Review: Invented 50 Years Ago and Applied Today. *Hindawi International Journal of Optics*, page 17, 2018.
- [132] B.Ya. Zel’dovich, V. I. Popovichev, V. V. Ragul’skii, and F. S. Faizullov. Connection Between the Wave Fronts of the Reflected and Exciting Light in Stimulated Mandel’Shtam-Brillouin Scattering. (109):303–306, 1972.
- [133] Zhenxu Bai, Hang Yuan, Zhaohong Liu, Pengbai Xu, Qilin Gao, Robert J. Williams, Ondrej Kitzler, Richard P. Mildren, Yulei Wang, and Zhiwei Lu. Stimulated Brillouin scattering materials, experimental design and applications: A review. *Optical Materials*, 75:626–645, jan 2018.
- [134] Zhenxu Bai, Yulei Wang, Zhiwei Lu, Hang Yuan, Zhenxing Zheng, Sensen Li, Yi Chen, Zhaohong Liu, Can Cui, Hongli Wang, and Rui Liu. High Compact, High Quality Single Longitudinal Mode Hundred Picoseconds Laser Based on Stimulated Brillouin Scattering Pulse Compression. *Applied Sciences 2016, Vol. 6, Page 29*, 6(1):29, jan 2016.
- [135] Liang Wang and Chester Shu. Dynamic control of phase matching in four-wave mixing wavelength conversion of amplitude-and phase-modulated signals. *Journal of Lightwave Technology*, 31(9):1468–1474, 2013.
- [136] Gaurav Bahl, John Zehnpfennig, Matthew Tomes, and Tal Carmon. Stimulated optomechanical excitation of surface acoustic waves in a microdevice. *Nature Communications 2011 2:1*, 2(1):1–6, jul 2011.
- [137] Peter T. Rakich, Charles Reinke, Ryan Camacho, Paul Davids, and Zheng Wang. Giant Enhancement of Stimulated Brillouin Scattering in the Subwavelength Limit. *Physical Review X*, 2(1):011008, jan 2012.
- [138] Chris N. Richardson, Nathan Sime, and Garth N. Wells. Scalable computation of thermomechanical turbomachinery problems. *Finite Elements in Analysis and Design*, 155:32–42, mar 2019.

- [139] Smit. ASiMoV Prosperity Partnership, 2018.
- [140] Johan Hoffman, Johan Jansson, and Niclas Jansson. FEniCS-HPC: Automated predictive high-performance finite element computing with applications in aerodynamics. 2016.
- [141] V Vinje, J Brucker, ME Rognes, KA Mardal, and V Haughton. Fluid dynamics in syringomyelia cavities: Effects of heart rate, CSF velocity, CSF velocity waveform and craniovertebral decompression. *The Neuroradiology Journal*, 31(5):482, oct 2018.
- [142] Marcin Malinowski and Sasan Fathpour. Fully-Tensorial Modeling of Stimulated Brillouin Scattering in Photonic Waveguides. *IEEE JOURNAL OF QUANTUM ELECTRONICS*, 2019.
- [143] O.C. Zienkiewicz. *The Finite Element Method Fifth edition Volume 2: Solid Mechanics*. 2000.
- [144] James Clerk Maxwell. *A Dynamical Theory of the Electromagnetic Field*. 1864.
- [145] Albert Migliori, Hassel Ledbetter, Robert G. Leisure, C. Pantea, and J. B. Betts. Diamond’s elastic stiffnesses from 322 K to 10 K. *Journal of Applied Physics*, 104(5):053512, sep 2008.
- [146] M. H. Grimsditch and A. K. Ramdas. Brillouin scattering in diamond. *Physical Review B*, 11(8):3139, apr 1975.
- [147] Haiyin Sun. Laser Diode Beam Basics, Manipulations and Characterizations. *Media*, page 83, 2012.
- [148] Robert W. Boyd. Stimulated Brillouin and Stimulated Rayleigh Scattering. In *Nonlinear Optics*, pages 409–450. 2003.
- [149] Zhenxu Bai, Robert J Williams, and Ondrej Kitzler. Diamond Brillouin laser in the visible . *APL Photonics*, 5:31301, 2020.

- [150] Z Zhu, M D Dawes, D J Gauthier, L Zhang, and A E Willner. Wavelength dependence of the Brillouin spectral width of boron doped germanosilicate optical fibers . *J. Lightwave Technol*, 4(5):11, 1968.
- [151] Virgil Taillandier. High speed imaging detectors with diamond dynode materials. (October), 2013.
- [152] Qiang Liu, Luigi Bibbó, Sacharia Albin, Qiong Wang, Mi Lin, Huihui Lu, and Zhengbiao Ouyang. Plasmonic waveguide design for the enhanced forward stimulated brillouin scattering in diamond. *Scientific Reports*, 8(1), dec 2018.
- [153] G. Aiello, S. Schreck, K. A. Avramidis, T. Franke, G. Gantenbein, J. Jelonnek, A. Meier, T. Scherer, D. Strauss, M. Thumm, M. Q. Tran, C. Wild, and E. Wörner. Towards large area CVD diamond disks for Brewster-angle windows. *Fusion Engineering and Design*, 157:111818, aug 2020.
- [154] Jack Ogden. Diamonds: An early history of the king of gems. page 388, 2018.
- [155] De Beers. History of Diamonds — Diamond Education — De Beers UK.
- [156] K. P.S.S. Hembram, Sohyung Lee, Hyunsik Im, Hyunsu Ju, Sang Hun Jeong, and Jae Kap Lee. The surface hybridization of diamond with vertical graphene: A new route to diamond electronics. *Materials Horizons*, 7(2):470–476, 2020.
- [157] Neil W. Ashcroft and N. David. Mermin. Solid state physics. page 826, 1976.
- [158] A MARIKANI. MATERIALS SCIENCE. 2018.
- [159] Karl E. Spear, John P. Dismukes, and Electrochemical Society. Synthetic diamond : emerging CVD science and technology. page 663, 1994.
- [160] M. A. Pinault, J. Barjon, T. Kociniowski, F. Jomard, and J. Chevallier. The n-type doping of diamond: Present status and pending questions. *Physica B: Condensed Matter*, 401-402:51–56, 2007.

- [161] Georgia F. Wood, Carmen E. Zvoriste-Walters, Mark G. Munday, Mark E. Newton, Viacheslav Shkirskiy, Patrick R. Unwin, and Julie V. Macpherson. High pressure high temperature synthesis of highly boron doped diamond microparticles and porous electrodes for electrochemical applications. *Carbon*, 171:845–856, jan 2021.
- [162] Morana Druskovic, Drazen Vouk, Hana Posavcic, Ivan Halkijevic, and Karlo Nad. The application of electrochemical processes in oily wastewater treatment: a review Morana Druskovic, Drazen Vouk, Hana Posavcic, Ivan Halkijevic & Karlo Nad The application of electrochemical processes in oily wastewater treatment: a review. *Journal of Environmental Science and Health*, 2021.
- [163] José Manuel Díaz-Cruz, Núria Serrano, Clara Pérez-Ràfols, Cristina Ariño, and Miquel Esteban. Electroanalysis from the past to the twenty-first century: challenges and perspectives. *Journal of Solid State Electrochemistry* 2020 24:11, 24(11):2653–2661, jun 2020.
- [164] Donald T. Sawyer. Electrochemistry. *Encyclopedia of Physical Science and Technology*, pages 161–197, jan 2003.
- [165] P. L. Cabot, F. Alcaide, and E. Brillas. Cogeneration of Energy and Chemicals: Fuel Cells. *Encyclopedia of Electrochemical Power Sources*, pages 146–156, jan 2009.
- [166] Omowunmi A. Sadik, Austin O. Aluoch, and Ailing Zhou. Status of biomolecular recognition using electrochemical techniques. *Biosensors and Bioelectronics*, 24(9):2749–2765, may 2009.
- [167] T. Yokoya, T. Nakamura, T. Matsushita, T. Muro, Y. Takano, M. Nagao, T. Takenouchi, H. Kawarada, and T. Oguchi. Origin of the metallic properties of heavily boron-doped superconducting diamond. *Nature* 2005 438:7068, 438(7068):647–650, dec 2005.
- [168] Sigal A. Wolf, Itamar Rosenberg, Ronen Rapaport, and Nir Bar-Gill. Initialization and measurement of nitrogen-vacancy centers in diamond with plasmonic Purcell enhancement. *Quantum Optics*, 9900(April 2016):99000S, 2016.

- [169] Alexios Beveratos, Sergei Kühn, Rosa Brouri, Thierry Gacoin, Jean-Philippe Poizat, and Philippe Grangier. Room temperature stable single-photon source. 2001.
- [170] G D Fuchs, G Burkard, P V Klimov, and D D Awschalom. A quantum memory intrinsic to single nitrogen–vacancy centres in diamond. *Nature Physics*, 7, 2011.
- [171] B Hensen, H Bernien, A E Dréau, A Reiserer, N Kalb, M S Blok, J Ruitenber, R F L Vermeulen, R N Schouten, C Abellán, W Amaya, V Pruneri, M W Mitchell, M Markham, D J Twitchen, D Elkouss, S Wehner, T H Taminiau, and R Hanson. Experimental loophole-free violation of a Bell inequality using entangled electron spins separated by 1.3 km. 2015.
- [172] Benjamin Griffiths, Ben L. Green, Colin J. Stephen, Gavin W. Morley, Jason M. Smith, Laiyi Weng, Mark E. Newton, Martin J. Booth, Patrick S. Salter, Sam Johnson, Shannon S. Nicley, Shazeaa N. Ishmael, Yashna Lekhai, and Yu-Chen Chen. Laser writing of individual nitrogen-vacancy defects in diamond with near-unity yield. *Optica*, Vol. 6, Issue 5, pp. 662–667, 6(5):662–667, may 2019.
- [173] Peter G. Read. *Gemmology*. page 324, 2005.
- [174] Element 6. FASTER DRILLING, LONGER LIFE, LOWER COSTS. Technical report, 2017.
- [175] Howard L. Hartman and Jan M. Mutmanský. *Introductory mining engineering*. page 570, 2002.
- [176] Richard C. Bullock. *Underground Mining Methods*. 2001.
- [177] Joshua A Hammons, Michael H Nielsen, Michael Bagge-Hansen, Sorin Bastea, Chadd May, William L Shaw, Aiden Martin, Yuelin Li, Nicholas Sinclair, Lisa M Lauderbach, Ralph L Hodgkin, Daniel A Orlikowski, Laurence E Fried, and Trevor M Willey. Submicrosecond Aggregation during Detonation Synthesis of Nanodiamond. *J. Phys. Chem. Lett.* 2021, 12:5293, 2021.
- [178] Edward K. Chow, Xue Qing Zhang, Mark Chen, Robert Lam, Erik Robinson, Hou-jin Huang, Daniel Schaffer, Eiji Osawa, Andrei Goga, and Dean Ho. Nanodiamond

- therapeutic delivery agents mediate enhanced chemoresistant tumor treatment. *Science Translational Medicine*, 3(73), mar 2011.
- [179] Shawqi H. Alawdi, Housam Eidi, Marwa M. Safar, and Mosaad A. Abdel-Wahhab. Loading amlodipine on diamond nanoparticles: A novel drug delivery system. *Nanotechnology, Science and Applications*, 12:47–53, 2019.
- [180] J M Z Im. The thermal conductivity of diamond at low temperatures. *Proceedings of the Royal Society of London. Series A. Mathematical and Physical Sciences*, 220(1141):171–183, nov 1953.
- [181] Ksenia Nosaeva, Thualfiqar Al-Sawaf, Wilfred John, Dimitri Stoppel, Matthias Rudolph, Franz Josef Schmuckle, Bernd Janke, Olaf Kruger, Viktor Krozer, Wolfgang Heinrich, and Nils G. Weimann. Multifinger indium phosphide double-heterostructure transistor circuit technology with integrated diamond heat sink layer. *IEEE Transactions on Electron Devices*, 63(5):1846–1852, 2016.
- [182] Mark P. Hiscocks, Christopher J. Kaalund, Francois Ladouceur, Shane T. Huntington, Brant C. Gibson, Steven Trpkovski, David Simpson, Eric Ampem-Lassen, and Steven Prawer. Diamond waveguides: toward an all-diamond platform. *Photonics: Design, Technology, and Packaging III*, 6801(December):68010J, 2007.
- [183] A.M. Zaitsev. *Optical Properties of Diamond*. Springer, 2001.
- [184] C. E. Bradley, J. Randall, M. H. Abobeih, R. C. Berrevoets, M. J. Degen, M. A. Bakker, M. Markham, D. J. Twitchen, and T. H. Taminiau. A Ten-Qubit Solid-State Spin Register with Quantum Memory up to One Minute. *Physical Review X*, 9(3):31045, 2019.
- [185] D. D. Sukachev, A. Sipahigil, C. T. Nguyen, M. K. Bhaskar, R. E. Evans, F. Jelezko, and M. D. Lukin. Silicon-Vacancy Spin Qubit in Diamond: A Quantum Memory Exceeding 10 ms with Single-Shot State Readout. *Physical Review Letters*, 119(22):1–5, 2017.

- [186] G. D. Fuchs, G. Burkard, P. V. Klimov, and D. D. Awschalom. A quantum memory intrinsic to single nitrogen-vacancy centres in diamond. *Nature Physics*, 7(10):789–793, 2011.
- [187] ROGERS H STOLEN. Polarization Effects in Fiber Raman and Brillouin Lasers. (10), 1979.
- [188] R M Shelby, M D Levenson, and P W Bayer. Resolved Forward Brillouin Scattering in Optical Fibers. 54(9), 1985.
- [189] Lin Zhang, Raymond Barrett, Peter Cloetens, Carsten Detlefs, Manuel Sanchez, and Del Rio. Synchrotron Radiation Anisotropic elasticity of silicon and its application to the modelling of X-ray optics. *J. Synchrotron Rad*, 21:507–517, 2014.
- [190] D Donadio, M Bernasconi, and F Tassone Pirelli Cavi Sistemi Sp. Photoelasticity of crystalline and amorphous silica from first principles. 2003.
- [191] Willi Pabst and Eva Gregorová. Elastic Properties of Silica Polymorphs - A Review. *Original papers Ceramics-Silikáty*, 57(3):167–184, 2013.
- [192] Myeong Soo Kang, André Brenn, Gustavo S. Wiederhecker, and Philip St J. Russell. Optical excitation and characterization of gigahertz acoustic resonances in optical fiber tapers. *Applied Physics Letters*, 93(13):3–6, 2008.
- [193] Fan Yang, Flavien Gyger, Adrien Godet, Jacques Chrétien, Li Zhang, Meng Pang, Jean-Charles Beugnot, and Luc Thévenaz. Large evanescently-induced Brillouin scattering at the surrounding of a nanofibre. 2021.
- [194] Casimer. DeCusatis and Carolyn J. Sher. DeCusatis. Fiber optic essentials. page 271, 2006.
- [195] Stephanos Yerolatsitis. Adiabatically Tapered All-Fibre Devices for Mode Manipulation. 2016.
- [196] Rongqing Hui. Introduction to fiber-optic communications. *Introduction to Fiber-Optic Communications*, pages 1–635, jan 2019.

- [197] Tim A. Birks, Philip St J. Russell, and D. O. Culverhouse. The acousto-optic effect in single-mode fiber tapers and couplers. *Journal of Lightwave Technology*, 14(11):2519–2529, 1996.
- [198] Hilel Hagai Diamandi, Gil Bashan, Yosef London, Kavita Sharma, Keren Shemer, and Avi Zadok. Interpolarization Forward Stimulated Brillouin Scattering in Standard Single-Mode Fibers. *Laser and Photonics Reviews*, 16(1), jan 2022.
- [199] P. Kharel, R. O. Behunin, W. H. Renninger, and P. T. Rakich. Noise and dynamics in forward Brillouin interactions. *Physical Review A*, 93(6):1–12, 2016.
- [200] Raman Kashyap. Fiber Bragg Gratings. *Fiber Bragg Gratings*, 2010.
- [201] J. Bros. Dispersion Relations. *Encyclopedia of Mathematical Physics: Five-Volume Set*, pages 87–101, jan 2006.
- [202] Wenjun Qiu, Peter T Rakich, Heedeuk Shin, Hui Dong, Marin Soljačić, Soljačić, Zheng Wang, Y Choi, H Mcfarlane, S Hile, E Li, L Thevenaz, B Luther-Davies, S J Madden, and B J Eggleton. Stimulated Brillouin scattering in nanoscale silicon step-index waveguides: a general framework of selection rules and calculating SBS gain. *Phys*, 5(25):276–280, 2009.
- [203] Daniel Royer and Eugene Dieulesaint. *Elastic Waves in Solids I: Free and Guided Propagation*. 1996.
- [204] Theoretical Physics and Physical Sciences. Brillouin scattering — theory and experiment : tutorial. 38(4), 2021.
- [205] Steve M Rohde. Finite Element Optimization of Finite Stepped Slider Bearing Profiles. *ASLE TRANSACTIONS*, 17(2):105–110, 1974.
- [206] Roger T. Fenner. Mechanics of solids. page 625, 1989.
- [207] A.S. Vasudeva. *Principle of Engineering Physics*.

-
- [208] O. V. Ivanov, S. A. Nikitov, and Yu V. Gulyaev. Cladding modes of optical fibers: Properties and applications. *Cladding modes of optical fibers: Properties and applications*, 49(2):167–191, feb 2006.
- [209] Mingjie Ding, Desheng Fan, Wenyu Wang, Yanhua Luo, and Gang-Ding Peng. Basics of Optical Fiber Measurements. *Handbook of Optical Fibers*, pages 1–39, 2018.
- [210] R. J. Black, S. Lacroix, F. Gonthier, and J. D. Love. Tapered single-mode fibres and devices Part 2. Experimental and theoretical quantification. *IEE proceedings. Part J, Optoelectronics*, 138(5):355–364, 1991.